AN ABSTRACT OF THE DISSERTATION OF

Melanie Ann Jenkins for the degree of Doctor of Philosophy in Electrical and Computer Engineering presented on October 18, 2019.

Title: Investigation of Energy Barrier Heights within Metal-insulator-metal Devices via Internal Photoemission Spectroscopy

Abstract approved:

John F. Conley Jr.

Metal-insulator-metal (MIM) and dual-insulator MIM (MIIM) devices are used in rectennas, hot-electron transistors, single electron transistors, resistive random access memory (RRAM), and capacitors. The performance of these devices relies heavily on the energy barrier height at each metal-insulator interface. Thus, determination of the *in-situ* electron energy barrier at each interface is critical to accurately predicting charge transport and confidently integrating new materials into microelectronic devices. Internal photoemission (IPE) spectroscopy is a well-established electro-optical technique that allows for direct measurement of interfacial energy barriers within a device structure. Although IPE has widely been used to characterize the interfaces between various

polycrystalline elemental metals and oxides within MOS structures, there have been relatively few reports of IPE within MIM structures.

First, MIM structures with amorphous metal bottom electrodes are investigated via IPE. Amorphous metals are attractive for use in the aforementioned devices owing to their ultra-low roughness which gives rise to a highly uniform electric field in the ultrathin sandwiched insulator(s). IPE is used to measure the energy barrier heights in MIM device structures between either amorphous metal ZrCuAlNi, Ta-based amorphous metals (TaNiSi and TaWSi), or polycrystalline TaN and insulators deposited via atomic layer deposition (ALD). It is found that the Ta-based amorphous metals exhibit the largest barrier heights. The effect on the barrier height of a number of interfacial non-idealities are explored, including an interfacial ZrO_x layer on ZrCuAlNi. A comparison is also made between Al and Au top electrodes for devices with a TaWSi bottom electrode, unexpectedly showing an effect of the top electrode on the bottom electrode barrier height. It is found that IPE energy barriers are consistent with current-voltage asymmetry of MIM diodes, whereas ideal Schottky model predictions of barrier heights were inconsistent.

Next, ALD ruthenium top electrodes are investigated in both MIM and MOS structures. ALD metals such as ruthenium are promising electrode materials with growing interest for applications that require conformal, pinhole free conductive films, particularly for high aspect-ratio structures. Ru, due to relatively low bulk resistivity, high work function, a conductive oxide (RuO_2), and ease of etching, is of interest as a gate electrode for MOS transistors, metal-insulator-metal (MIM) capacitors, RRAM, and tunnel diodes, as well as a conductive Cu diffusion barrier/liner for Cu interconnects. IPE

is used to directly measure the φ_{Bn} between ALD dielectrics Al_2O_3 and HfO_2 and ALD Ru, both as-deposited and after a post-metallization anneal. Large barrier heights are found, supporting use of Ru as a gate electrode. It is found that barrier heights are relatively unaffected by the post-metallization anneal. The effects of interfacial oxides and interfacial charge trapping on the measured barrier heights are discussed.

IPE is also utilized to study ALD ferroelectric HfZrOx. There has been increasing interest in ferroelectric materials for non-volatile memory applications. Barrier heights at the interface of ALD ferroelectric HfZrOx films and various metals are determined within MIM structures on TaN bottom electrodes. Knowledge of these technologically relevant barrier heights will assist in integration of ALD ferroelectric HfZrOx into non-volatile memory devices.

Finally, bi-layer stacks of Al_2O_3 and Ta_2O_5 with differing ratios are characterized with current-voltage analysis and preliminary IPE measurements. Conduction mechanisms are proposed for all regions of current-voltage behavior and it is found that device performance may be engineered using the relative thicknesses of the insulators. Preliminary IPE results suggest that the insulator offset within the MIIM device may be determined using a standard IPE approach.

Investigation of Energy Barrier Heights within Metal-insulator-metal Devices via Internal Photoemission Spectroscopy

by
Melanie Ann Jenkins

A DISSERTATION

submitted to

Oregon State University

in partial fulfillment of
the requirements for the
degree of

Doctor of Philosophy

Presented October 18, 2019
Commencement June 2020

Doctor of Philosophy dissertation of Melanie Ann Jenkins presented October 18, 2019.

APPROVED:

John F. Conley, Jr., Major Professor, representing Electrical and Computer Engineering

Head of the School of Electrical Engineering and Computer Science

Dean of the Graduate School

I understand that my dissertation will become part of the permanent collection of Oregon State University libraries. My signature below authorizes release of my dissertation to any reader upon request.

Melanie Ann Jenkins, Author

ACKNOWLEDGEMENTS

I would like to express sincerest appreciation to Dr. John F. Conley, Jr., whose guidance and support has been invaluable in completion of this work. Thank you to my committee members Dr. Alan Wang, Dr. Larry Cheng, Dr. Greg Herman, and Dr. Janet Tate. I would also like to thank Chris Tasker and Rick Presley for equipment support and the Center for Sustainable Materials Chemistry for financial support. Thank you also to the many members of the cleanroom community. Finally, I would like to thank my husband, my parents, and my brother for their unwavering love and support.

CONTRIBUTION OF AUTHORS

In Chapter 2, T. Klarr patterned the ZrO_2, SiO_2, and HfO_2 samples and performed IPE testing on these three devices at NIST. He also developed the first version of Python code for analysis of the IPE data. D.Z. Austin assisted in device fabrication. W. Li and N.V. Nguyen assisted in IPE measurements performed at NIST. In Chapter 3, J.M. McGlone and J.F. Wager deposited the Ta-based amorphous metals and provided valuable input on interpretation of results. In Chapter 4, M.H. Hayes performed all device fabrication. In Chapter 5, S.W. Smith provided fabricated devices. In Chapter 6, D.Z. Austin led project work, deposited ALD films, and performed data analysis. K.E.K. Holden measured devices, performed data analysis, and assisted in manuscript preparation and revision. D. Allman provided project and manuscript input.

TABLE OF CONTENTS

Page

TABLE OF CONTENTS (CONTINUED)

TABLE OF CONTENTS (CONTINUED)

Page

LIST OF FIGURES

LIST OF FIGURES (CONTINUED)

LIST OF FIGURES (CONTINUED)

LIST OF TABLES

1 INTRODUCTION

Internal photoemission (IPE) spectroscopy is an electro-optical technique that allows for direct measurement of specific interfacial energy barriers within a metal-insulator-metal (MIM) or metal-insulator-semiconductor (MOS) device.[1–3] This is particularly useful in work with MIM tunnel diodes, which are of interest for use in high-speed applications such as rectenna based energy harvesting of IR radiation,[4–6] as building blocks for beyond CMOS hot-electron (MIMIM) transistors,[7,8] and for use in resistive random access memory.[9] Many of these devices ideally operate via Fowler-Nordheim tunneling (FNT), which is strongly dependent both on electric field and the height of the energy barriers between the two metal electrodes and the insulator, denoted as φ_B in Fig. 1.1. Ideally, φ_B is defined as the difference between the metal work function (Φ_M) and the insulator electron affinity (χ_i) at a given interface. However, the φ_B at real interfaces generally does not match this ideal value due to a number of potential non-idealities such as interfacial dipoles, charge trapping, and interfacial oxides. Because FNT is strongly dependent on the metal/insulator barrier heights in the device, knowledge of the real barrier heights within devices is critical for predicting, understanding, and optimizing MIM diode device operation. IPE is uniquely qualified for this as it is the only technique to directly measure the insitu energy barrier heights, accounting for any non-idealities at the interface that may affect the barrier height.[10,11]

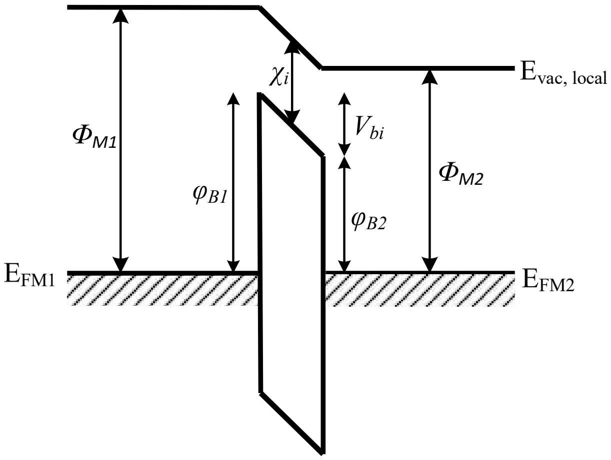

Figure 1.1: Band diagram of a metal-insulator-metal device with dissimilar metal electrodes, showing the two different barrier heights (φ_B) that arise due to the two different metal work functions (Φ_M). V_{bi} is the difference in the two metal work functions.

A schematic of the IPE system at Oregon State University is shown in Fig. 1.2. All components of the system are controlled via LabVIEW. In this system, a sample is exposed to light while electrical measurements are simultaneously performed. The light originates from a 150 W Xe arc lamp with a shutter that can be opened and closed remotely such that measurements may be performed both with and without light on the sample. The light then passes through a monochromator that selects a single wavelength of interest and then a collimating lens. A filter wheel which houses two long pass filters is then placed in the light path to filter out second-order diffraction from the monochromator. From the filter wheel, the light is then shined onto the device of interest using a parabolic mirror focused to a spot size of approximately 1 mm^2. Electrical measurements are performed with bias applied to the bottom electrode from a DC voltage source while the top electrode is held at ground where current is measured with an electrometer.

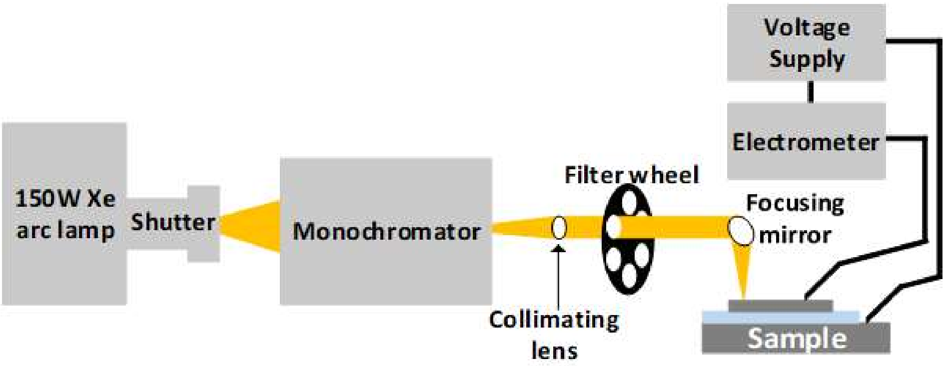

Figure 1.2: Schematic of the internal photoemission (IPE) spectroscopy system at Oregon State University.

Prior to IPE measurement, a standard current-voltage sweep is performed with no illumination. Next, a small bias (+/-2 V) is applied to the device and the voltage is held constant for 3 minutes to allow time for the current to settle, and the “dark-current” measurement is taken. This value is used in analysis. Next, light is shined onto the device and a current measurement is taken at each step in photon energy. Typically, this is done over the photon energy range of 2 to 5 eV with 0.1 eV steps. When the photon energy is approximately equal to the spectral threshold of the interest, there will be an increase in photocurrent as electrons are emitted over the barrier. After the photon energy sweep is completed, the bias is then stepped to the next value and the process is repeated. Measurements are performed at an array of biases, typically +/-2 eV, to allow for emission from both the top and bottom electrodes.

One important design consideration for devices to be measured with IPE is that the top electrode must be semi-transparent to light within the range of photon energies to be tested. Additionally, the insulator thickness must be thick enough such that internal photoemission is the dominant source of current flow in the voltage range used in IPE testing, which is typically +/-2 V. This means that it must be thick enough to prevent direct tunneling or Fowler-Nordheim tunneling within the testing voltage range. The insulator must also have minimal trapping, and the barrier itself should be greater than 1 eV such that internal photoemission dominates over thermionic emission in the measured photocurrent.[12]

The internal photoemission process is typically modeled as a three-step process consisting of the optical excitation of the carrier, transport to the interface, and escape over the barrier. It can be characterized by the quantum yield *Y*, which is the photocurrent normalized to the number of incident photons.[5] The quantum yield can be calculated from the escape probability for carriers over the barrier *P(E)* and the energy distribution function carriers *N(E)* using the equation[13]

$$Y(hv) = \int_0^{hv} N(E)P(E)dE. \tag{1}$$

Near the photoemission threshold, this can be simplified to[14]

$$Y(hv) = A(hv - \Phi)^p. \tag{2}$$

where A is a constant, hv is the photon energy, Φ is the threshold energy, and p is a fitting parameter dependent on the shape of the energy distribution function. In the case of a metal, the energy distribution at the surface is described as a step function, and in the case of a semiconductor it is described as a linear function.[14] This gives a p value of 2 for a metal emitter and a p value of 3 for a semiconductor emitter.

In order to determine barrier heights from IPE data, the measured current is corrected by subtracting the dark current or leakage current at each applied bias such that only photocurrent is analyzed. The quantum yield is then calculated and plotted as $Y^{1/p}$ versus hv and the spectral threshold (Φ_{thresh}) is found, where Φ_{thresh} is the photon energy at which photoemission over the barrier begins. Spectral thresholds are determined using an algorithm to find the largest region of the $Y^{1/2}$ curve with the highest linearity, as determined from the R^2 value of a linear regression. After the region for linearization is determined, the x-intercept is calculated, giving Φ_{thresh} for that specific bias. Φ_{thresh} values are then plotted as a function of the square root of the electric field in the oxide, taking into account the built-in field in the device. The y-intercept of a linear regression of this data is then found in order to obtain the zero-field barrier height, φ_B, to account for field-dependent barrier lowering.[15] Ideally, this field dependence is due to image-force barrier lowering, and the slope of the extraction is dependent on the dielectric constant of the oxide. However, this may not always be the case due to non-idealities such as the presence of charges near the interface or interfacial layers, and is typically reported for metal-insulator barriers [16–18].

In this manner, IPE may be used to extract the insitu barrier height at metal-insulator interfaces. IPE may also be used to determine the slope parameter for new insulators of interest by measuring the barrier height at the interface of this insulator and multiple metals.[18] In addition to the barrier height, there are a number of additional insights that can be gained from IPE data, including information on interfacial layers, dipoles, and charge trapping. For example, the slope of the linear fit to the Schottky plot is related to the dielectric constant of the insulator. However, Schottky plots of the same insulator but different metal interfaces often exhibit differing slopes. Afanas'ev et al. report this for Al_2O_3 and ZrO_2 with the metal-insulator interface showing weaker field dependence than the metal-semiconductor interface and indicate that that could be due to a sheet of negative charges near the metal interface.[18] The slope of the Schottky plot can also be related to lateral non-uniformity of the metal work function.[19]

In this work, several novel MIM and MOS devices have been characterized using internal photoemission spectroscopy and current-voltage measurements. First, the barrier heights at the interface between amorphous metals and ALD insulators are determined with IPE using MIM structures. Amorphous metals are of interest for a number of applications, including as bottom electrodes in tunnel diodes. This is because these amorphous metals are atomically smooth, allowing for a uniform electric field within a MIM device. Three amorphous metals are examined as bottom electrodes in this work. In Chapter 2, ZrCuAlNi is characterized in contact with a number of ALD insulators. This amorphous metal has proven to be beneficial in thin MIM tunnel diodes, however it suffers from poor thermal stability.[20] To address this drawback of ZrCuAlNi, amorphous metals TaWSi and TaNiSi were characterized with IPE in Chapter 3, along with TaN, a metal commonly used in the semicondutor industry. Both of these Ta-based amorphous metals exhibit a larger work functions than ZCAN, improved thermal stability,[21,22] and minimal interfacial layer. In Chapter 4, the barrier height of ruthenium deposited via atomic layer deposition was characterized as a top electrode in both MIM and MOS devices. There has been enhanced interest in Ru in recent years due its high work function, ease of etching, and conductive oxide. Knowledge of the barrier heights present at the interface of ALD oxides and ALD Ru can be beneficial in understanding interface properties and the effect of annealing. In Chapter 5, an ALD ferroelectric insulator, HfZrOx, is characterized via IPE within MIM devices using an array of top electrodes, allowing for determination of barrier heights, the slope parameter for this insulator, and the band gap. In Chapter 6, metal-insulator-insulator-metal devices intended for high voltage applications and one-time-programmable applications are characterized with current-voltage measurements and conduction mechanisms are assessed for each region of operation. In Chapter 7, initial results are presented, including IPE measurements of the devices from Chapter 6 and IPE measurements of solution deposited insulators in comparison with ALD insulators.

1.1 References

[1] [1] V.K. Adamchuk and V.V. Afanas'ev, "Internal Photoemission Spectroscopy of Semiconductor-Insulator Interfaces," Prog. Surf. Sci. **41**, 111 (1992).

[2] V.V. Afanas'ev and A. Stesmans, "Internal Photoemission at Interfaces of High-κ Insulators with Semiconductors and Metals," J. Appl. Phys. **102**, 081301 (2007).

[3] N.V. Nguyen, O.A. Kirillov, W. Jiang, J.E. Maslar, W. Kimes, and J.S. Suehle, "Interface Barrier Determination by Internal Photoemission: Applications to Metal/Oxide/Semiconductor Structure," ECS Trans. **13**, 161 (2008).

[4] A. Sharma, V. Singh, T.L. Bougher, and B.A. Cola, "A Carbon Nanotube Optical Rectenna," Nat. Nanotechnol. **10**, 1027 (2015).

[5] M. Bareib, B.N. Tiwari, A. Hochmeister, G. Jegert, U. Zschieschang, H. Klauk, B. Fabel, G. Scarpa, G. Koblmuller, G.H. Bernstein, W. Porod, and P. Lugli, "Nano Antenna Array for Terahertz Detection," IEEE Trans. Microw. Theory Tech. **59**, 2751 (2011).

[6] G. Moddel and S. Grover, editors , "Rectenna Solar Cells," *Rectenna Solar Cells* (Springer New York, New York, NY, 2013).

[7] M. Heiblum, “Tunneling Hot Electron Transfer Amplifiers (Theta): Amplifiers Operating up to the Infrared,” Solid-State Electron. **24**, 343 (1981).

[8] S. Vaziri, A.D. Smith, M. Östling, G. Lupina, J. Dabrowski, G. Lippert, W. Mehr, F. Driussi, S. Venica, V. Di Lecce, A. Gnudi, M. König, G. Ruhl, M. Belete, and M.C. Lemme, “Going Ballistic: Graphene Hot Electron Transistors,” Solid State Commun. **224**, 64 (2015).

[9] H.-S.P. Wong, H.-Y. Lee, S. Yu, Y.-S. Chen, Y. Wu, P.-S. Chen, B. Lee, F.T. Chen, and M.-J. Tsai, “Metal-Oxide RRAM,” Proc. IEEE **100**, 1951 (2012).

[10] V.V. Afanas’ev, N. Kolomiiets, M. Houssa, and A. Stesmans, “Internal Photoemission Metrology of Inhomogeneous Interface Barriers,” Phys. Status Solidi A **215**, n/a (2017).

[11] V.V. Afanas’ev and A. Stesmans, “Internal Photoemission at Interfaces of High-κ Insulators with Semiconductors and Metals,” J. Appl. Phys. **102**, 081301 (2007).

[12] V.V. Afanas′ev, “Internal Photoemission Spectroscopy: Principles and Applications,” *Internal Photoemission Spectroscopy: Principles and Applications* (Elsevier, Oxford ;Heidelberg [u.a., 2008).

[13] N.V. Nguyen, O. Kirillov, H.D. Xiong, and J.S. Suehle, “Internal Photoemission Spectroscopy of Metal Gate/High-k/Semiconductor Interfaces,” in *AIP Conf. Proc.* (AIP Publishing, 2007), pp. 308–314.

[14] R.J. Powell, “Interface Barrier Energy Determination from Voltage Dependence of Photoinjected Currents,” J. Appl. Phys. **41**, 2424 (1970).

[15] R.J. Powell, “Interface Barrier Energy Determination from Voltage Dependence of Photoinjected Currents,” J. Appl. Phys. **41**, 2424 (1970).

[16] M.A. Jenkins, T. Klarr, D.Z. Austin, W. Li, N.V. Nguyen, and J.F. Conley, Jr., "Assessment of Energy Barriers Between ZrCuAlNi Amorphous Metal and Atomic Layer Deposition Insulators Using Internal Photoemission Spectroscopy," Phys. Status Solidi RRL – Rapid Res. Lett. **12**, 1700437 (2018).

[17] N.V. Nguyen, H.D. Xiong, J.S. Suehle, O.A. Kirillov, E.M. Vogel, P. Majhi, and H.-C. Wen, "Internal Photoemission Spectroscopy of [TaN⁄TaSiN] and [TaN⁄TaCN] Metal Stacks on SiO2 and [HfO2⁄SiO2] Dielectric Stack," Appl. Phys. Lett. **92**, 092907 (2008).

[18] V.V. Afanas'ev, M. Houssa, A. Stesmans, and M.M. Heyns, "Band Alignments in Metal–Oxide–Silicon Structures with Atomic-Layer Deposited Al2O3 and ZrO2," J. Appl. Phys. **91**, 3079 (2002).

[19] V.V. Afanas'ev, N. Kolomiiets, M. Houssa, and A. Stesmans, "Internal Photoemission Metrology of Inhomogeneous Interface Barriers," Phys. Status Solidi A 1700865 (2017).

[20] N. Alimardani, E.W. Cowell, J.F. Wager, J.F. Conley, Jr., D.R. Evans, M. Chin, S.J. Kilpatrick, and M. Dubey, "Impact of Electrode Roughness on Metal-Insulator-Metal Tunnel Diodes with Atomic Layer Deposited Al2O3 Tunnel Barriers," J. Vac. Sci. Technol. A **30**, 01A113 (2012).

[21] J.M. McGlone, K.R. Olsen, W.F. Stickle, J.E. Abbott, R.A. Pugliese, G.S. Long, D.A. Keszler, and J.F. Wager, "TaWSi Amorphous Metal Thin Films: Composition Tuning to Improve Thermal Stability," MRS Commun. **7**, 715 (2017).

[22] J.M. McGlone, K.R. Olsen, W.F. Stickle, J.E. Abbott, R.A. Pugliese, G.S. Long, D.A. Keszler, and J.F. Wager, "Ta-Based Amorphous Metal Thin Films," J. Alloys Compd. **650**, 102 (2015).

2 ASSESSMENT OF ENERGY BARRIERS BETWEEN ZrCuAlNi AMORPHOUS METAL AND ATOMIC LAYER DEPOSITION INSULATORS USING INTERNAL PHOTOEMISSION SPECTROSCOPY

Melanie A. Jenkins,[*] Tyler Klarr,[*] Dustin Z. Austin, Wei Li, Nhan V. Nguyen,
and John F. Conley, Jr.
[*]These authors contributed equally

Phys. Status Solidi RRL **12**, 1700437 (2018)

2.1 Introduction

As scaling becomes increasingly difficult, continued advancement of microelectronics now relies on the introduction of new materials with properties chosen to address current challenges. For example, ultra-smooth electrodes are needed to ensure uniform control of the very high electric fields placed across ultra-thin insulators in metal-insulator-metal (MIM) structures used for capacitors, resistive random access memories (RRAM), hot-electron transistors, single-electron transistors, and tunnel diodes for high speed rectifying applications including rectennas and infrared detection.[1–9] New metal gates with low and uniform work function (Φ_M) are needed to maximize capacitive control of the channel and minimize threshold voltage (V_{th}) variation in metal/oxide/semiconductor field-effect transistors (MOSFETs).[10-13] A promising solution to both of these challenges is the use of amorphous metals. The lack of grain boundaries in an amorphous metal (i) allows an ultra-smooth surface that avoids topography induced electric field enhancement, improving yield and reducing current hot spots and early breakdown in MIM devices,[13-17] and (ii) avoids lateral work function variation due to different grain orientation, improving subthreshold slope and V_{th} control in MOS devices.[10-13] Recently, it was shown that using the amorphous metal zirconium-copper-aluminum-nickel (ZrCuAlNi) as an ultra-smooth bottom electrode with insulators deposited via atomic layer deposition (ALD) enables reproducible fabrication of MIM diodes with stable current-voltage behavior.[14–17]

In order to accurately predict charge transport and confidently integrate new materials such as amorphous metals into microelectronic devices, accurate knowledge of the *in situ* electron energy barrier at each new interface is required. In general, the heights of these metal-insulator barriers may not be accurately predicted using the bulk properties of the materials measured in vacuum (ideally $\varphi_{Bn} = \Phi_M - \chi_I$,[18] where χ_I is the electron affinity) due to processing induced differences, metal induced gap states, and non-idealities such as Fermi-level pinning, charge trapping defects, dipoles, and band tailing, etc. at metal-insulator interfaces.[19,20] The standard method of extracting barrier heights from current-voltage data frequently does not produce accurate results due to temperature dependent conduction mechanisms and a lack of precise knowledge of the built-in voltage (V_{bi}). X-ray photoelectron spectroscopy (XPS) is limited to the material properties in vacuum, rather than in intimate contact with another material with which there may be interactions. Internal photoemission (IPE) spectroscopy, on the other hand, is a well-established electro-optical technique that allows direct measurement of specific interfacial energy barriers within a device structure.[21–23] Although IPE has been widely used to characterize the interfaces between various polycrystalline elemental metals and oxides within MOS structures,[21] there have only been a few reports of IPE within MIM structures,[23–27] many of which were on native oxides rather than high quality deposited oxides, and no reports of IPE on amorphous electrodes.

In this work, IPE spectroscopy is used to directly measure the *in situ* barrier heights in MIM structures between ZrCuAlNi, an amorphous metal alloy bottom electrode, and several technologically relevant insulators deposited via atomic layer deposition (ALD).

2.2 Experimental Procedure

IPE devices in this study were fabricated on silicon substrates with 100 nm of thermally grown SiO_2. ZrCuAlNi bottom electrodes were deposited on the SiO_2 using DC magnetron sputtering from a single alloy target of $Zr_{40}Cu_{35}Al_{15}Ni_{10}$, either at Oregon State University or at the U.S. Army Research Lab. ZrCuAlNi films are amorphous and have a root-mean square roughness of ~ 0.3 nm. A detailed report on the deposition and physical properties of ZrCuAlNi may be found in [16]. Various insulators were deposited on the ZrCuAlNi bottom electrode using ALD to target an insulator thickness of roughly 10 nm. SiO_2 was deposited with plasma-enhanced ALD (PEALD) using bis(diethylamino)silane and oxygen plasma as precursors in a Picosun SUNALE R-200 reactor at 200 °C. Al_2O_3, HfO_2 and ZrO_2 were deposited using thermal ALD in a Picosun SUNALE R-150 reactor at 250 °C. The precursors used for Al_2O_3, HfO_2 and ZrO_2 were trimethylaluminum (TMA), tetrakis(ethylmethylamino)hafnium, and tetrakis(ethylmethylamino)zirconium, respectively, all with water as the oxidizing agent. A 10-15 nm thick 200 μm square of thermally evaporated Al serves as a semi-transparent electrode for the IPE measurements, and a 100 nm thick 100 μm square Al serves as contact pad, with both Al films being polycrystalline.[28] Al_2O_3 and SiO_2 films deposited under these conditions are expected to be amorphous.[16,29] Similarly deposited 5 nm thick HfO_2 on ZrCuAlNi was shown to be amorphous by transmission electron microscopy.[28] For the HfO_2 and ZrO_2 samples deposited on ZrCuAlNi, X-ray diffraction (XRD), performed with a Bruker D8 XRD system, showed no crysallization within the resolution of the tool. To avoid crystallization of the ZrCuAlNi, no post-deposition anneals were performed.

IPE measurements were performed both at the National Institute of Standards and Technology and on a similar system built at Oregon State University. Details of this system are described elsewhere.[30] Bias was applied to the bottom ZrCuAlNi electrode and the top Al electrode was grounded. A 150 W Xe arc lamp light source was passed through a monochromator, followed by a long-pass filter to remove second-order diffraction. The long pass filter is changed at 2.6 and 3.8 eV. The light was then focused onto the device of interest using a parabolic mirror with a final spot size of 1 mm^2. At each applied bias, the current was measured as the photon energy (hv) was swept from 1.5 to 5 eV. The IPE yield (Y) is defined as photocurrent normalized to the incident photon flux. The spectral threshold (φ_{thresh}) of the IPE quantum yield is found using a linear extrapolation of a Fowler plot of $Y^{1/2}$ versus hv to the x-axis.[21,30] The portion of the $Y^{1/2}(hv)$ plot used for determination of φ_{thresh}, referred to as the extraction window, can significantly affect the final extracted barrier height (φ_{Bn}). Considerations for the extraction window include photoconduction at high photon energies, sub-threshold emission at lower energies either into band-tail states of the conduction band or defect levels in the oxide, and lateral non-uniformity of the barrier.[23] In this work, φ_{thresh} extraction was performed using an algorithm which employed a moving window to determine the region of highest linearity from the yield curves by comparing the coefficient of determination for each window.

2.3 Results and Discussion

Shown in Fig. 2.1 are representative plots of $Y^{1/2}$ vs. hv for SiO_2, Al_2O_3, HfO_2, and ZrO_2. Fig. 2.1(a) shows emission from the Al top electrode under negative field in the insulator. Fig. 2.1(b) shows emission from the ZrCuAlNi bottom electrode under positive field. The dashed lines indicate the linear regressions for each sweep that were used to determine φ_{thresh}. The "peak" at 3.2 eV in the Al_2O_3 sample is an artifact due to second-order diffraction in the monochromator (long pass filters were not used for this measurement). Although the 3.2 eV artifact could potentially cause an artificially high barrier height, the impact of this peak is assumed to be insignificant given the location of the window for yield extraction. φ_{thresh} values were determined by extrapolation from the most linear porion of the yield curves. Weak sub-threshold "tails" are observed in the Al_2O_3, HfO_2, and SiO_2 yield spectra (indicated by dotted lines). For emission from Al, the onset of emission occurs as low as 2.0, 1.9, and 3.4 eV; for ZrCuAlNi, the onsets are at 2.6, 2.9, and 3.1 eV for Al_2O_3, HfO_2, and SiO_2, respectively. Emission tails can be caused by conduction band tail states in these amorphous insulators. The broader nature of the subthreshold tails for emission from Al may be due to additional lateral non-uniformities caused by variation of the Al workfunction on different faces of the crystalline Al grains, which is absent for the amorphous ZrCuAlNi.[31]

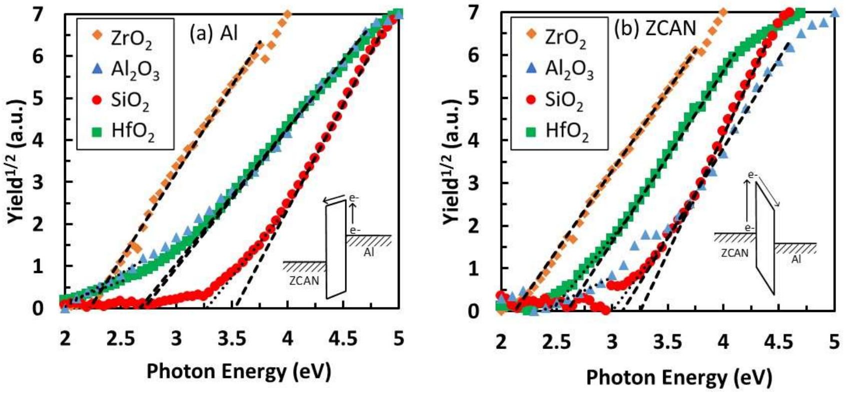

Figure 2.1: Representative plots of $Y^{1/2}$ vs. hv for ZrCuAlNi/insulator/Al devices under (a) negative field (emission from the Al electrode) and (b) positive field (emission from the ZrCuAlNi electrode). Curves are taken at $\xi^{1/2}$ values of +/- 0.7 (MV/cm)$^{1/2}$ for SiO_2 and HfO_2, +0.22/-0.7 (MV/cm)$^{1/2}$ for ZrO_2, and +1/-1.2 (MV/cm)$^{1/2}$ for Al_2O_3, where ξ is defined as the field in the insulator corrected for V_{bi}. The linear extractions for the spectral thresholds are shown as dashed lines, weak "tails" are indicated with dotted lines.

In order to correct for any image force or field induced barrier lowering that may be present, the φ_{thresh} values determined from $Y^{1/2}$ vs. hv plots at multiple applied biases are plotted vs. the square root of the insulator field ($\xi^{1/2}$) at which they were collected. Note that $\xi^{1/2}$ is corrected for the V_{bi} of each device (taken as the voltage at which emission switches from the top to the bottom electrode). Shown in Fig. 2.2 are Schottky plots (hv vs. $\xi^{1/2}$) for all devices at (a) positive and (b) negative ξ. The zero-field barrier heights for (a) the Al interface ($\varphi_{Bn\text{-}Al}$) and (b) the ZrCuAlNi interface ($\varphi_{Bn\text{-}ZrCuAlNi}$) were then extracted from the y-axis intersection of extrapolated linear fits of the φ_{thresh}'s. Although image force barrier lowering should ideally be present in all of these device structures and should be more pronounced for the lower dielectric constant insulators, no correspondence of the slopes of these plots to insulator dielectric constant was found. The lack of correspondence is often reported in IPE of metal-insulator interfaces and has been attributed to interfacial charge or to the presence of an interfacial layer (IL) oxide at the injecting (either Al or ZrCuAlNi) interfaces. [32,33]

Fig. 2.2 (c) shows energy band diagrams based on these experimentally determined φ_{Bn} values (shown as solid lines) superimposed on theoretical band diagrams (dashed lines). The theoretically predicted band diagrams are constructed from literature values of the vacuum metal work functions ($\Phi_{ZrCuAlNi}$ = 4.8 eV, Φ_{Al} = 4.2 eV) and insulator electron affinities ($\chi_{insulator}$), applying the ideal model ($\varphi_{Bn} = \Phi_M - \chi_I$). Literature values of insulator bandgaps are used for both sets of band diagrams. $\varphi_{Bn\text{-}Al}$, $\varphi_{Bn\text{-}ZrCuAlNi}$, and the barrier difference, $\varphi_{Bn,\ ZrCuAlNi\text{-}Al}$, for each insulator are tabulated in Table 2.1.

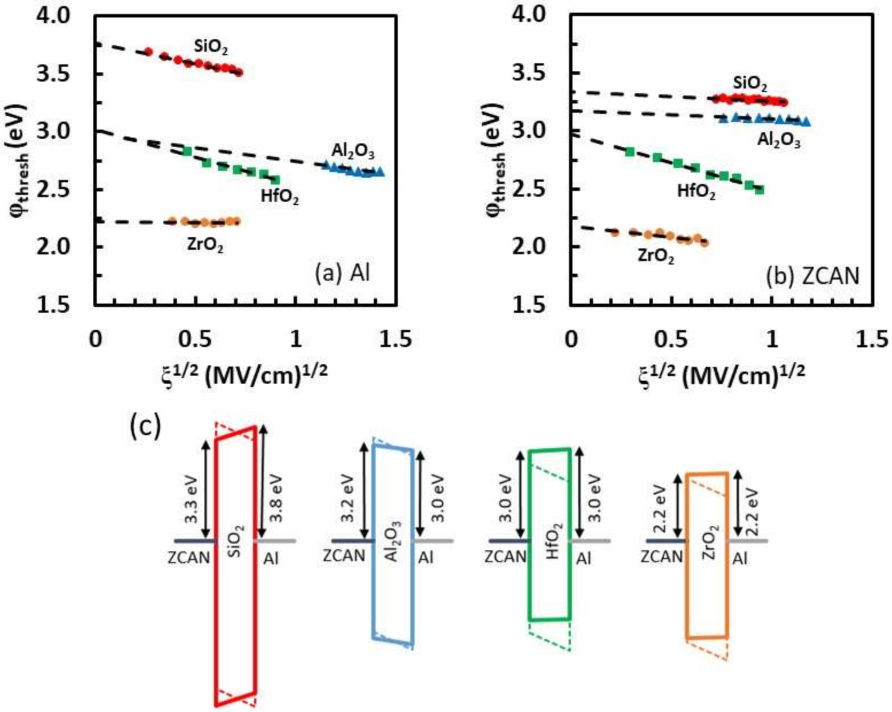

Figure 2.2: Schottky plots of φ_{Bn} vs. $\xi^{1/2}$ for (a) negative bias IPE (emission from Al interface) and (b) positive bias (emission from ZrCuAlNi interface). Dashed lines show the extrapolated linear fits. The φ_{Bn}'s are taken from the intersection with the y-axis. (c) The resulting energy band diagrams of all devices based on IPE barrier heights measured in this work (solid lines) superimposed on band diagrams based on literature values of electron affinity and work function (dashed lines). Bandgap values taken from literature.[15,18]

Table 2.1: Results for barrier heights presented in this work as compared to previously reported values by IPE.

Insulator (χ_i)	Measured			Literature
	$\varphi_{Bn,ZrCuAlNi}$ (eV)	$\varphi_{Bn,Al}$ (eV)	$\varphi_{Bn,\ ZrCuAlNi-Al}$ (eV)	$\varphi_{Bn,Al}$ (eV)
SiO_2 (0.9 eV [40])	3.3	3.8	-0.5	3.15 [33] (thermally grown)
Al_2O_3 (1.4 eV [41])	3.2	3.0	0.2	2.9 [33] (ALD - TMA)
HfO_2 (2.25 eV [42])	3.0	3.0	~0.0	2.5 [34] (CVD)
ZrO_2 (2.75 eV [43])	2.2	2.2	~0.0	2.7 [33] (ALD - $ZrCl_4$)

At the ZrCuAlNi interface, the IPE measured $\varphi_{Bn,ZrCuAlNi}$ were 3.3, 3.2, 3.0, and 2.2 eV for SiO_2, Al_2O_3, HfO_2, and ZrO_2, respectively. This trend is consistent with the trend of literature reported band gaps of the respective oxides. The measured $\varphi_{Bn,ZrCuAlNi}$, however, is smaller than that expected from $\varphi_{Bn,ZrCuAlNi} = \Phi_{ZrCuAlNi} - \chi_{insulator}$ for both SiO_2 and Al_2O_3. In prior work, $\Phi_{ZrCuAlNi}$ was reported to be 4.8 eV *via* Kelvin probe electrostatic voltmeter measurement.[16] Assuming $\Phi_{ZrCuAlNi} = 4.8$ eV, predicts $\varphi_{Bn,ZrCuAlNi} =$ 3.9, 3.4, 2.55, and 2.05 eV, for SiO_2, Al_2O_3, HfO_2, and ZrO_2 respectively. These results suggest a smaller ZrCuAlNi *effective* work function than was previously reported.

At the Al interface, measured $\varphi_{Bn,Al}$ were 3.8, 3.0, 3.0, and 2.2 eV for SiO_2, Al_2O_3, HfO_2, and ZrO_2, respectively. Assuming $\Phi_{Al} = 4.2$ eV predicts $\varphi_{Bn,Al} = 3.3$, 2.8, 1.95, and 1.45 eV, for SiO_2, Al_2O_3, HfO_2, and ZrO_2 respectively. All Al barriers are thus larger than expected from $\Phi_{Al} - \chi_{insulator}$. Also shown in Table 2.1 are previously reported IPE results for $\varphi_{Bn,Al}$ values of 3.15, 2.9, 2.5, and 2.7 eV for SiO_2, Al_2O_3, HfO_2, and ZrO_2 respectively.[33,34] These values are also all larger than predicted. Compared to previous reports, our measured $\varphi_{Bn,Al}$ values for SiO_2 and HfO_2 are larger, while our value for ZrO_2 is smaller. It should be noted that barrier heights depend critically on the microscopic details of the metal insulator interface. For example, metal vacuum work functions are known to vary with crystal face, deposition technique, surface preparation, etc. In addition, all of these previous insulators were synthesized by a different technique (thermal SiO_2, chemical vapor deposited (CVD) HfO_2) or used a different ALD precursor ($ZrCl_4$ for ZrO_2) than used here. It is worth noting that for ALD Al_2O_3 deposited using the same precursor (TMA), the $\varphi_{Bn,Al}$ reported here matches closely with that reported in literature (2.97 vs. 2.9 eV, respectively).

As shown in Fig. 2.1, φ_{thresh} values for the onset of strong emission were determined by extrapolation from the most linear portion of the yield curves. Weak, sub-spectral-threshold "tails" are observed in the Al_2O_3, HfO_2, and SiO_2 yield spectra. For emission from Al, the onset of emission in these tails (dotted fits in Fig. 2.1) occurs as low as 3.4, 2.0, and 1.9 eV; for ZrCuAlNi, the onsets are at 3.1, 2.6, and 2.9 eV, for SiO_2, Al_2O_3, and HfO_2, respectively. These weak low energy emission tails may be caused by conduction band tail states or defect levels in the amorphous insulators or perhaps by a lower bandgap IL oxide (ZrO_2 in the case of ZrCuAlNi).[32] Finally, the broader nature of the subthreshold tails for emission from Al may be due to additional lateral non-uniformities caused by variation of the Al workfunction on different faces of the crystalline Al grains.[31]

Between the two electrodes, the barrier height difference, $\varphi_{Bn,ZrCuAlNi-Al}$, should ideally be equal to the metal vacuum work function difference, $\Phi_{Bn,ZrCuAlNi-Al} \sim +0.6$ eV. The findings presented in this work, however, show that $\varphi_{Bn,ZrCuAlNi-Al}$ is much smaller than $\Phi_{Bn,ZrCuAlNi\text{-}Al}$, with $\varphi_{Bn,ZrCuAlNi\text{-}Al}$ values ranging from +0.2 to -0.5 eV depending on the insulator (see Table 2.1), meaning that for some MIM devices measured, the ZrCuAlNi barrier is actually *lower* than the Al barrier. Variation of electrode work function difference across different insulators has also been reported in MOS structures.[33] The fact that $\varphi_{Bn,ZrCuAlNi\text{-}Al} < 0.6$ eV across all four insulators tested again points towards the effective work function of ZrCuAlNi being significantly lower than previously reported.

These results indicate several non-idealities: (i) measured ZrCuAlNi barriers are smaller than expected for SiO_2 and Al_2O_3, (ii) all Al barriers are all larger than expected, and (iii) $\varphi_{Bn,ZrCuAlNi\text{-}Al}$ is not consistent across the four insulators tested. One key difference between IPE and the Kelvin probe is that the Kelvin probe measures Φ_M with respect to vacuum, missing any potential contributions from IL oxides, interfacial dipoles, Fermi-level pinning, or oxide charging in the MIM device structure used for IPE.[27,33–35]

Fermi-level pinning can play a role in determining barrier heights of high-k dielectrics.[36] Because only two metals were measured, we cannot confidently state whether Fermi-level pinning plays a strong role here. However, pinning is typically absent in SiO_2, is weak in unannealed metals on HfO_2,[36] and previous IPE measurements show only weakly pinned Fermi levels for Al_2O_3 and ZrO_2.[21] The potential impact of IL oxides and dipoles at either or both the ZrCuAlNi or Al interface is considered below.

One possible cause for the non-idealities is the presence of oxide ILs at the metal electrode interfaces. Al has a large enthalpy of reaction with oxygen (ΔH_{ox}), meaning that when Al is in contact with an oxide that has a cation with a lower ΔH_{ox}, the Al will tend to react with the oxygen at or near the interface, potentially creating positively charged oxygen vacancies in the ALD oxide[37] or forming a thin Al_2O_3 IL. While it was shown that insertion of an SiO_2 IL of sufficient thickness can alter the barrier height between ZrO_2 and Si by suppressing emission over the Si/ZrO_2 barrier, an Al_2O_3 IL did not have the same effect because the height of the barrier was too low.[38] This suggests that an Al_2O_3 IL alone would not alter the barrier heights of the high-κ oxides.

At the other interface, ZrCuAlNi is known to grow a thin (~1.5 nm) native oxide consisting primarily of ZrO_x.[16] The low barrier height of a ZrO_x IL would also not be expected to suppress emission into any of the oxides tested in this work. However, it is possible that the low barrier of the sub-stoichiometric ZrO_x is acting to effectively decrease the barrier height at the ZrCuAlNi/SiO_2 and ZrCuAlNi/Al_2O_3 interfaces by acting as a step for photo-excited electrons at lower energies.[32] If this were true, the ZrCuAlNi/SiO_2 and ZrCuAlNi/Al_2O_3 barriers would be most reduced and the ZrO_2 device would still have a near expected $\varphi_{Bn,ZrCuAlNi\text{-}Al}$ of 0.6 eV, but this is not the case. In fact, the Al_2O_3 device has the closest $\varphi_{Bn,ZrCuAlNi\text{-}Al}$ to the Kelvin probe result while the ZrO_2 device has a $\varphi_{Bn,ZrCuAlNi\text{-}Al}$ of nearly zero. This indicates that the ZrO_2 layer at the ZrCuAlNi interface is also not solely responsible for the $\varphi_{Bn,ZrCuAlNi\text{-}Al}$ deviations though it may contribute to the broad sub-threshold emission observed in SiO_2, Al_2O_3, and HfO_2, as discussed above.

Another possible cause for the $\varphi_{Bn,ZrCuAlNi\text{-}Al}$ discrepancies are interfacial dipoles at each insulator/electrode interface as well as the interfaces between the ALD oxides and the IL oxides. Any dipole that arises near the ZrCuAlNi electrode would likely be between the native ZrO_x IL and the ALD oxide. Previous studies on interfacial dipoles between various high-κ oxides and SiO_2 showed a relationship between the oxygen areal density (σ) difference between the oxides and the resultant flatband voltage shift.[35,39] Assuming that this model applies to all pairs of insulators, since σ is similar for HfO_2 and ZrO_2 there would not be an appreciable dipole present at the ZrCuAlNi electrode in either of these devices. However, SiO_2 has a larger σ than ZrO_2 and Al_2O_3 has a smaller σ than ZrO_2. This would lead to dipoles of opposite polarity for the SiO_2 device and Al_2O_3 device, contrary to the measured $\varphi_{Bn,ZrCuAlNi-Al}$ values in Table 2.1.

At the Al electrode, oxygen-scavenging induced creation of positively charged oxygen vacancies in the ALD oxide could lead to the formation of a dipole which would lower barriers at the Al interfaces. However, the Al barrier heights for all devices are the same or greater than the barriers expected based on $\Phi_{Al} - \chi_{ALD\ insulator}$. Alternatively, it has been shown that high-κ ALD insulators in MOS structures tend to exhibit a negative dipole layer at the metal interface.[33] This effect was more pronounced in ZrO_2 than Al_2O_3 and for lower Φ_M metals. In our MIM structures, it would be expected that this negative dipole would be present on both sides of the insulator, raising both barrier heights. Assuming that $\Phi_{ZrCuAlNi}$ is indeed lower than previously reported, a negative dipole at the ZrCuAlNi interface would also account for the relatively larger than expected ZrCuAlNi barrier heights for the smaller bandgap insulators. Yet another additional dipole contribution at the Al interface could arise due to differences in σ. Again assuming that the oxygen areal density model[39] applies to all pairs of insulators, there would be an additional negative dipole contribution between the previously discussed Al_2O_3 IL and the ALD SiO_2, HfO_2, and ZrO_2 insulators. This additional negative dipole could account for the opposite polarity $\varphi_{Bn,ZrCuAlNi-Al}$ measured for these three devices and would be strongest for SiO_2. Taken together, these latter two dipole contributions could account for the larger than expected $\varphi_{Bn,Al}$ for all insulators as well as for the variation seen in $\varphi_{Bn,ZrCuAlNi\text{-}Al}$ between each insulator.

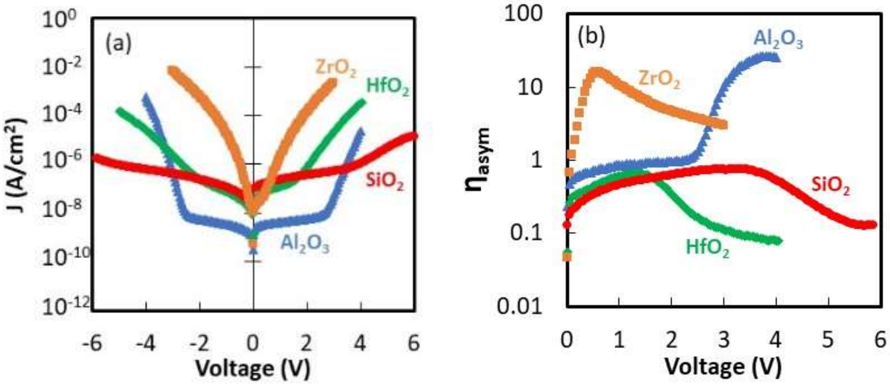

Figure 2.3: Representative (a) current density and (b) asymmetry vs. voltage plots of the ZrCuAlNi/*insulator*/Al devices used for IPE measurements.

Finally, shown in Fig. 2.3 are (a) current density (J) and (b) conduction asymmetry (η_{asym}) vs. voltage (V) plots of all devices. Note that although thermally grown SiO_2 exhibits significantly less leakage current than ALD SiO_2, it is not possible to thermally grow SiO_2 on a metal electrode. η_{asym} is defined as the current density at negative bias (J_-) divided by the corresponding positive bias (J_+) when grounding the ZrCuAlNi electrode ($\eta_{asym} = |J_-/J_+|$), so that $\eta_{asym} = 1$ indicates symmetric J-V behavior. Qualitatively, the relationship between the top and bottom electrode $\varphi_{Bn's}$ can be estimated from the asymmetry in the Fowler-Nordheim tunneling (FNT) region, assuming a single layer insulator with no IL oxides. If $\eta_{asym} > 1$, then the ZrCuAlNi barrier is greater than the Al barrier; if $\eta_{asym} < 1$, the opposite is true. Based on $\Phi_{ZrCuAlNi\text{-}Al} = +0.6$ eV, all devices should show $\eta_{asym} < 1$. In the FNT regions of Fig. 2.3(b), $\eta_{asym} > 1$ for Al_2O_3, indicating that $\varphi_{Bn,ZrCuAlNi\text{-}Al} > 0$, in line with predictions. However, both SiO_2 and HfO_2 show $\eta_{asym} < 1$, consistent with $\varphi_{Bn,ZuCrAlNi\text{-}Al} < 0$, opposite of predictions. These qualitative assessments of the relative barrier heights of SiO_2, HfO_2, and Al_2O_3 from the electrical data are all consistent with the measured IPE $\varphi_{Bn,ZrCuAlNi\text{-}Al}$ values (listed in Table 2.1 and illustrated in the band diagrams in Fig. 2.2). For the ZrO_2 device, FNT is overwhelmed by other conduction processes, and thus it cannot be analyzed in this way. It is seen that the IPE measured $\varphi_{Bn's}$ explain well the electrical behavior of these MIM devices whereas the ideal model does not.

2.4 Conclusion

IPE spectroscopy was used to directly measure energy barriers between an amorphous metal, ZrCuAlNi, and various ALD insulators in MIM device structures. These results were compared to barrier heights measured on an opposing Al electrode. The ZrCuAlNi barrier heights across all insulators were found to be lower than expected from the vacuum properties of the materials, while all Al barrier heights were found to be higher than expected. Despite the reported vacuum work function of ZrCuAlNi being greater than Al, the Al barrier was found to be *higher* than the ZrCuAlNi barrier for all but the Al_2O_3 device. These results point toward the effective work function of ZrCuAlNi being close to that of Al and are consistent with the presence of negative dipoles between the ALD insulators and each metal. These unexpected barrier heights measured using IPE were found to agree qualitatively with current-voltage measurements on identical devices, whereas ideal theory ($\varphi_{Bn} = \Phi_M - \chi_i$) does not. These results demonstrate that bulk vacuum parameters are insufficient to accurately predict barrier heights and device performance in MIM device structures and that experimental determination of barrier heights at the actual interfaces is needed.

2.5 Acknowledgements

This work is supported by NSF Center for Sustainable Materials Chemistry, grant CHE-1102637. The authors thank J. McGlone, and Prof. J.F. Wager for the ZrCuAlNi bottom electrodes deposited at OSU, C. Tasker for equipment support, and the U.S. Army Research Lab for use of facilities. Part of this work was conducted at the Materials Synthesis and Characterization (MaSC) Center, a National Nanotechnology Coordinated Infrastructure (NNCI) Northwest Nanotechnology Infrastructure (NWNI) user facility at Oregon State University, which is supported in part by the National Science Foundation (Grant ECC-1542101) and Oregon State University.

2.6 References

[1] H.-S.P. Wong, H.-Y. Lee, S. Yu, Y.-S. Chen, Y. Wu, P.-S. Chen, B. Lee, F.T. Chen, and M.-J. Tsai, “Metal-Oxide RRAM,” Proceedings of the IEEE **100**, 1951 (2012).

[2] D.Z. Austin, K.E.K. Holden, J. Hinz, and J.F. Conley, Jr., “Electrode Modulated Capacitance-Electric Field Nonlinearity in Metal-Insulator-Metal Capacitors,” Applied Physics Letters **110**, 263503 (2017).

[3] C.A. Mead, “Operation of Tunnel-Emission Devices,” Journal of Applied Physics **32**, 646 (1961).

[4] M. Heiblum, “Tunneling Hot Electron Transfer Amplifiers (Theta): Amplifiers Operating up to the Infrared,” Solid-State Electronics **24**, 343 (1981).

[5] S. Vaziri, A.D. Smith, M. Östling, G. Lupina, J. Dabrowski, G. Lippert, W. Mehr, F. Driussi, S. Venica, V. Di Lecce, A. Gnudi, M. König, G. Ruhl, M. Belete, and M.C.

Lemme, "Going Ballistic: Graphene Hot Electron Transistors," Solid State Commun. **224**, 64 (2015).

[6] A. Sharma, V. Singh, T.L. Bougher, and B.A. Cola, "A Carbon Nanotube Optical Rectenna," Nat Nano **10**, 1027 (2015).

[7] G. Moddel and S. Grover, editors , *Rectenna Solar Cells*, (Springer New York, New York, NY, 2013).

[8] M. Bareib, B.N. Tiwari, A. Hochmeister, G. Jegert, U. Zschieschang, H. Klauk, B. Fabel, G. Scarpa, G. Koblmuller, G.H. Bernstein, W. Porod, and P. Lugli, "Nano Antenna Array for Terahertz Detection," IEEE Transactions on Microwave Theory and Techniques **59**, 2751 (2011).

[9] G. Karbasian, M.S. McConnell, H. George, L.C. Schneider, M.J. Filmer, A.O. Orlov, A.N. Nazarov, and G.L. Snider, "Metal-Insulator-Metal Single Electron Transistors with Tunnel Barriers Prepared by Atomic Layer Deposition," Appl. Sci. **7**, 246 (2017).

[10] K. Ohmori, T. Matsuki, D. Ishikawa, T. Morooka, T. Aminaka, Y. Sugita, T. Chikyow, K. Shiraishi, Y. Nara, and K. Yamada, "Impact of Additional Factors in Threshold Voltage Variability of Metal/High-k Gate Stacks and Its Reduction by Controlling Crystalline Structure and Grain Size in the Metal Gates," in *2008 IEEE International Electron Devices Meeting* (2008), pp. 1–4.

[11] H.F. Dadgour, K. Endo, V.K. De, and K. Banerjee, "Grain-Orientation Induced Work Function Variation in Nanoscale Metal-Gate Transistors #x2014;Part II: Implications for Process, Device, and Circuit Design," IEEE Transactions on Electron Devices **57**, 2515 (2010).

[12] S.H. Bae, W.P. Bai, H.C. Wen, S. Mathew, L.K. Bera, N. Balasubramanian, N. Yamada, M.F. Li, and D.L. Kwong, "Laminated Metal Gate Electrode with Tunable Work Function for Advanced CMOS," in *Digest of Technical Papers. 2004 Symposium on VLSI Technology, 2004.* (2004), pp. 188–189.

[13] H.C. Wen, H.N. Alshareef, H. Luan, K. Choi, P. Lysaght, H.R. Harris, C. Huffman, G.A. Brown, G. Bersuker, P. Zeitzoff, H. Huff, P. Majhi, and B.H. Lee, "Systematic Investigation of Amorphous Transition-Metal-Silicon-Nitride Electrodes for Metal Gate CMOS Applications," in *Digest of Technical Papers. 2005 Symposium on VLSI Technology, 2005.* (2005), pp. 46–47.

[14] N. Alimardani, E.W. Cowell, J.F. Wager, J.F. Conley, Jr., D.R. Evans, M. Chin, S.J. Kilpatrick, and M. Dubey, "Impact of Electrode Roughness on Metal-Insulator-Metal Tunnel Diodes with Atomic Layer Deposited Al2O3 Tunnel Barriers," J. Vac. Sci. Technol. A **30**, 01A113 (2012).

[15] N. Alimardani, S.W. King, B.L. French, C. Tan, B.P. Lampert, and J.F. Conley, Jr., "Investigation of the Impact of Insulator Material on the Performance of Dissimilar Electrode Metal-Insulator-Metal Diodes," Journal of Applied Physics **116**, 024508 (2014).

[16] E.W. Cowell, N. Alimardani, C.C. Knutson, J.F. Conley, Jr., D.A. Keszler, B.J. Gibbons, and J.F. Wager, "Advancing MIM Electronics: Amorphous Metal Electrodes," Advanced Materials **23**, 74 (2011).

[17] N. Alimardani and J.F. Conley, Jr., "Enhancing Metal-Insulator-Insulator-Metal Tunnel Diodes via Defect Enhanced Direct Tunneling," Applied Physics Letters **105**, 082902 (2014).

[18] J. Robertson, “Band Offsets of Wide-Band-Gap Oxides and Implications for Future Electronic Devices,” Journal of Vacuum Science & Technology B **18**, 1785 (2000).

[19] V.V. Afanas′ev, “Internal Photoemission Spectroscopy: Principles and Applications,” *Internal Photoemission Spectroscopy: Principles and Applications* (Elsevier, Oxford ;Heidelberg, 2008).

[20] Zhu, Li Qiang, “Interfacial Dipole Effects on High-k Gate Stacks,” in *High-k Gate Dielectrics for CMOS Technology* (Wiley-VCH Verlag GmbH & Co. KGaA, 2012), pp. 319–353.

[21] V.V. Afanas’ev and A. Stesmans, “Internal Photoemission at Interfaces of High-κ Insulators with Semiconductors and Metals,” Journal of Applied Physics **102**, 081301 (2007).

[22] N.V. Nguyen, O.A. Kirillov, W. Jiang, J.E. Maslar, W. Kimes, and J.S. Suehle, “Interface Barrier Determination by Internal Photoemission: Applications to Metal/Oxide/Semiconductor Structure,” ECS Trans. **13**, 161 (2008).

[23] V. Afanas’ev, N. Kolomiiets, M. Houssa, and A. Stesmans, “Internal Photoemission Metrology of Inhomogeneous Interface Barriers,” Phys. Status Solidi A **215**, n/a (2017).

[24] W. Ludwig and B. Kornefpel, “Photoemission Studies on Thin Metal-Insulator-Metal Sandwiches,” Phys. Stat. Sol. (b) **24**, K137 (1967).

[25] K.H. Gundlach and J. Kadlec, “Spectral Dependence of the Photoresponse in MIM Structures: Influence of the Electrode Thickness,” Thin Solid Films **28**, 107 (1975).

[26] J. Kadlec and K.H. Gundlach, “Results and Problems of Internal Photoemission in Sandwich Structures,” Phys. Stat. Sol. (a) **37**, 11 (1976).

[27] V.V. Afanas'ev, A. Stesmans, L. Pantisano, S. Cimino, C. Adelmann, L. Goux, Y.Y. Chen, J.A. Kittl, D. Wouters, and M. Jurczak, "TiNx/HfO2 Interface Dipole Induced by Oxygen Scavenging," Applied Physics Letters **98**, 132901 (2011).

[28] N. Alimardani and J.F. Conley, Jr., "Step Tunneling Enhanced Asymmetry in Asymmetric Electrode Metal-Insulator-Insulator-Metal Tunnel Diodes," Appl. Phys. Lett. **102**, 143501 (2013).

[29] S. Jakschik, U. Schroeder, T. Hecht, M. Gutsche, H. Seidl, and J.W. Bartha, "Crystallization Behavior of Thin ALD-Al2O3 Films," Thin Solid Films **425**, 216 (2003).

[30] N.V. Nguyen, O. Kirillov, H.D. Xiong, and J.S. Suehle, "Internal Photoemission Spectroscopy of Metal Gate/High-k/Semiconductor Interfaces," AIP Conference Proceedings **931**, 308 (2007).

[31] S. Shamuilia, V.V. Afanas'ev, A. Stesmans, T. Schram, and L. Pantisano, "Internal Photoemission of Electrons from Ta-Based Conductors into SiO2 and HfO2 Insulators," Journal of Applied Physics **104**, 073722 (2008).

[32] N.V. Nguyen, H.D. Xiong, J.S. Suehle, O.A. Kirillov, E.M. Vogel, P. Majhi, and H.-C. Wen, "Internal Photoemission Spectroscopy of [TaN⁄TaSiN] and [TaN⁄TaCN] Metal Stacks on SiO2 and [HfO2⁄SiO2] Dielectric Stack," Applied Physics Letters **92**, 092907 (2008).

[33] V.V. Afanas'ev, M. Houssa, A. Stesmans, and M.M. Heyns, "Band Alignments in Metal–Oxide–Silicon Structures with Atomic-Layer Deposited Al_2O_3 and ZrO_2," Journal of Applied Physics **91**, 3079 (2002).

[34] V.V. Afanas'ev, A. Stesmans, F. Chen, X. Shi, and S.A. Campbell, "Internal Photoemission of Electrons and Holes from (100)Si into HfO2," Applied Physics Letters **81**, 1053 (2002).

[35] J. Widiez, K. Kita, K. Tomida, T. Nishimura, and A. Toriumi, "Internal Photoemission over HfO2 and Hf(1-x)SixO2 High-k Insulating Barriers: Band Offset and Interfacial Dipole Characterization," Jpn. J. Appl. Phys. **47**, 2410 (2008).

[36] J. Robertson, O. Sharia, and A.A. Demkov, "Fermi Level Pinning by Defects in HfO2-Metal Gate Stacks," Appl. Phys. Lett. **91**, 132912 (2007).

[37] C. Vallée, P. Gonon, C. Jorel, and F. El Kamel, "Electrode Oxygen-Affinity Influence on Voltage Nonlinearities in High-k Metal-Insulator-Metal Capacitors," Applied Physics Letters **96**, 233504 (2010).

[38] V.V. Afanas'ev, M. Houssa, A. Stesmans, and M.M. Heyns, "Electron Energy Barriers between (100)Si and Ultrathin Stacks of SiO_2, Al_2O_3, and ZrO_2 Insulators," Applied Physics Letters **78**, 3073 (2001).

[39] K. Kita and A. Toriumi, "Origin of Electric Dipoles Formed at High-k/SiO2 Interface," Appl. Phys. Lett. **94**, 132902 (2009).

[40] D. Hiller, R. Zierold, J. Bachmann, M. Alexe, Y. Yang, J.W. Gerlach, A. Stesmans, M. Jivanescu, U. Müller, J. Vogt, H. Hilmer, P. Löper, M. Künle, F. Munnik, K. Nielsch, and M. Zacharias, "Low Temperature Silicon Dioxide by Thermal Atomic Layer Deposition: Investigation of Material Properties," Journal of Applied Physics **107**, 064314 (2010).

[41] S. Swaminathan, Y. Sun, P. Pianetta, and P.C. McIntyre, “Ultrathin ALD-Al2O3 Layers for Ge(001) Gate Stacks: Local Composition Evolution and Dielectric Properties,” Journal of Applied Physics **110**, 094105 (2011).

[42] S. Monaghan, P.K. Hurley, K. Cherkaoui, M.A. Negara, and A. Schenk, “Determination of Electron Effective Mass and Electron Affinity in HfO2 Using MOS and MOSFET Structures,” Solid-State Electronics **53**, 438 (2009).

[43] M. Houssa, M. Tuominen, M. Naili, V. Afanas’ev, A. Stesmans, S. Haukka, and M.M. Heyns, “Trap-Assisted Tunneling in High Permittivity Gate Dielectric Stacks,” Journal of Applied Physics **87**, 8615 (2000).

3 INTERNAL PHOTOEMISSION SPECTROSCOPY DETERMINATION OF BARRIER HEIGHTS BETWEEN TA-BASED AMORPHOUS METALS AND ATOMIC LAYER DEPOSITED INSULATORS

M.A. Jenkins, J.M. McGlone, J.F. Wager, and J.F. Conley, Jr.

Journal of Applied Physics **125**, 055301 (2019)

3.1 Introduction

Metal-insulator-metal (MIM) and dual-insulator MIM (MIIM) structures are used in rectifying antennas (rectennas) for infrared energy harvesting,[1–3] hot-electron transistors,[4,5] single electron transistors,[6] resistive random access memory (RRAM),[7] and capacitors.[8,9] These devices require the use of a smooth bottom electrode in order to produce a uniform electric field across the ultra-thin sandwiched insulator(s).[10,11] ZrCuAlNi, an ultrasmooth amorphous metal, has seen use as the bottom electrode in MIM devices,[10,12,13] however it is limited by the presence of a ZrO_x interfacial layer, a relatively low effective work function near that of aluminum,[14] and most significantly, a low thermal stability limited to less than about 400 °C.[12,14] TaWSi and TaNiSi are two alternative amorphous metals that show much greater thermal stability, up to 900 °C for TaWSi and 600-700 °C for TaNiSi, and are expected to have minimal interfacial oxides.[15,16] Based on the vacuum work functions of their constituent elements, both TaWSi and TaNiSi are expected to have larger effective work functions than ZrCuAlNi and are thus more desirable as electrodes for these applications.

Precise knowledge of metal/insulator barrier heights, φ_{Bn}, is critical for predicting, understanding, and optimizing MIM device charge transport and operation.[17] In the simplest model, charge transfer across the interface is neglected, and φ_{Bn} should vary with the vacuum work function of the metal, $\Phi_{M,vac}$, so that $\varphi_{Bn} = \Phi_{M,vac} - \chi_i$ where χ_i is the insulator electron affinity. However, this is not typically the case.[17,18] In metal induced gap state (MIGS) theory, charge transfer at *intrinsic* interface traps creates an interfacial dipole that drives the metal Fermi level, E_{Fm}, towards the charge neutral level of the insulator, $E_{CNL,i}$, the energy at which the dominant character of the interface states in the forbidden gap switches from donor-like to acceptor-like.[19,20] Thus, the metal behaves as if it has an effective work function, $\Phi_{M\text{-}eff}$, different from $\Phi_{M,vac}$, where

$$\Phi_{M,eff} = E_{CNL,i} + S(\Phi_{M,vac} - E_{CNL,i}) \qquad (1)$$

and where S is the slope of a plot of φ_{Bn} versus $\Phi_{M,vac}$ for a given insulator,

$$S = \frac{\partial \varphi_{Bn}}{\partial \Phi_M}.^{21} \qquad (2)$$

S describes how much $\Phi_{M\text{-}eff}$ actually changes in response to a change in $\Phi_{M,vac}$, where $S = 0$ indicates complete "pinning" of E_{Fm} at $E_{CNL,i}$ and $S = 1$ indicates an absence of pinning.

Despite good success of this theory, it is difficult to calculate or determine the E_{CNL} for a given material and it is often observed that φ_{Bn}'s can deviate substantially from predictions due to *extrinsic* defects that can arise from processing details such as deposition method, interface traps and near interfacial trapped charge due to point defects, dipoles due to interfacial chemical reactions, and remote scavenging of oxygen. It is therefore necessary to directly measure φ_{Bn} for each metal/insulator combination.

An electro-optical technique that allows for the direct measurement of specific interfacial energy barriers within a device structure is internal photoemission (IPE) spectroscopy.[17] Although IPE has been widely used to characterize the interfaces between various polycrystalline elemental metals and oxides within MOS structures,[18,22,23] there have been only a few reports of IPE within MIM structures,[17,24–27] and only one previous report of IPE on an amorphous electrode.[14]

In this work, we use IPE spectroscopy to directly measure barrier heights in MIM device structures between two new Ta-based amorphous metals (TaNiSi and TaWSi), TaN, and insulators (Al_2O_3 and HfO_2) deposited via atomic layer deposition (ALD).

3.2 Experimental

MIM devices were fabricated on Si substrates with 100 nm of thermally grown SiO_2 to provide electrical isolation from the underlying Si. TaWSi and TaNiSi bottom electrodes were deposited using DC magnetron sputtering from single alloy targets targeting a thickness of 100 nm, verified via profilometry.[15,16] TaN bottom electrode substrates (obtained from ON semiconductor, Gresham, OR) consisted of a Si/SiO_2/Ta/TaN stack that was planarized via chemical mechanical polishing. Insulators were deposited on the bottom electrodes using atomic layer deposition (ALD), targeting a thickness of roughly 15 nm, such that the insulator was thick enough to prevent direct tunneling from dominating charge transport. Al_2O_3 and HfO_2 were deposited using thermal ALD in a Picosun SUNALE R-150 reactor at 250 °C. The precursors used for Al_2O_3 and HfO_2 were trimethylaluminum (TMA) and tetrakis(ethylmethylamino)hafnium (TEMA-Hf), respectively, with H_2O as the oxidizing agent. Insulator thickness was monitored by including a Si witness wafer (with a ~1.2 nm layer of native SiO_2) in the ALD chamber for each deposition. For the semi-transparent top contact needed for IPE measurements, approximately 10 nm of either Al or Au was deposited via thermal evaporation, monitored with a quartz crystal microbalance. Au top electrodes were patterned with a shadow mask to yield circular devices with a diameter of 250 μm. Al top electrodes were patterned with photolithography into 200 by 200 μm squares. No anneals were performed.

IPE measurements were conducted using a 150 W Xe arc lamp source that was passed through a monochromator and then a long-pass filter (to remove second-order diffraction). The light was then shined onto the device of interest using a parabolic mirror focused to a spot size of 1 mm^2. Electrical bias was applied to the MIM bottom electrode and the top electrode was held at ground. At each applied bias, V, the electrical current was measured as the photon energy ($h\nu$) was swept from 2 to 5 eV (620-248 nm). A large increase in current is detected as $h\nu$ approaches the height of the electron energy barrier between the metal and the insulator. The current was normalized by subtracting the dark current for each applied bias, such that only photo-induced current was analyzed. The quantum yield, Y, was calculated from normalized current, and spectral thresholds, φ_{thresh}, the photon energy at which photo-induced current exceeds the dark current for a given applied bias, were determined from plots of $Y^{1/2}$ versus $h\nu$.[18,28] To determine φ_{thresh} for each applied bias, an algorithm was implemented to find the largest region of the $Y^{1/2}$ curve with the highest linearity, as determined from the R^2 value of a linear regression. A linear regression of this region intercepted with the baseline gives φ_{thresh} for that specific bias. The zero-field barrier height, φ_{Bn}, for each interface was then found as the y-intercept of a Schottky plot of φ_{thresh} vs. the square root of the field across the insulator, $\xi^{1/2}$. The $\xi^{1/2}$ values are corrected for the built-in field, ξ_{bi}, of each device (taken as the field at which emission switches from the top to the bottom electrode). Reported φ_{Bn} values have estimated accuracy of +/- 0.1 eV. This is in line with commonly reported error values ranging from 0.05 to 0.1 eV.[29]

3.3 Results and Discussion

Shown in Fig. 3.1 are representative yield plots of $Y^{1/2}$ vs. $h\nu$ taken at various applied biases ranging between 0.4 to 1.2 $|MV^2/cm^2|$ for (a) Al_2O_3 and (b) HfO_2 insulators in Au top electrode MIM devices with TaN, TaNiSi, or TaWSi bottom electrodes. The dashed lines indicate the linear regressions that were used to determine the φ_{thresh}.

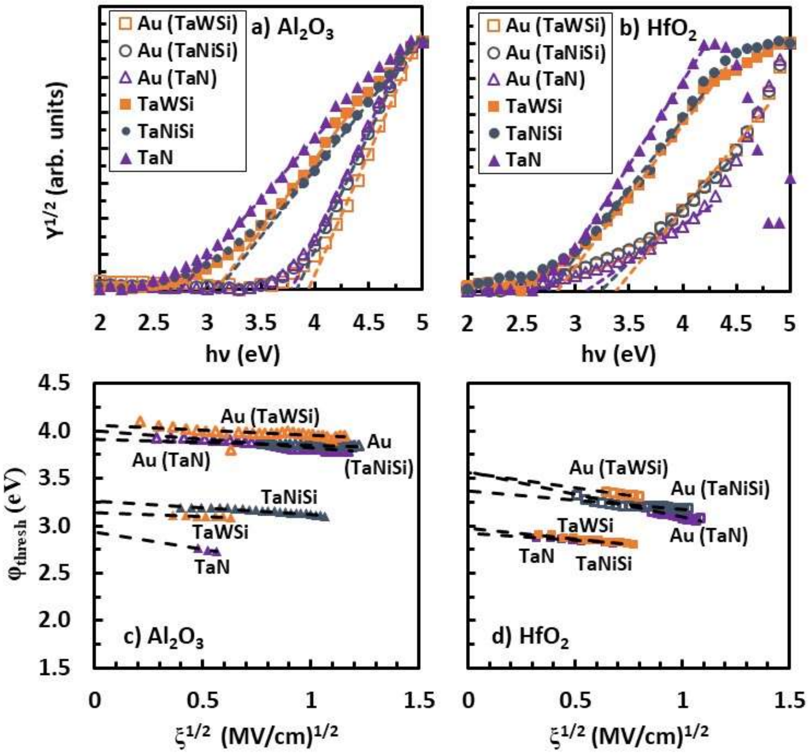

Figure 3.1: Representative plots of $Y^{1/2}$ vs. hv for (a) Al_2O_3 and (b) HfO_2 in MIM devices with Au top electrodes and with either a TaN, TaWSi, or TaNiSi bottom electrode as indicated. The dashed lines show the linear φ_{thresh} extraction for each interface. Also shown are Schottky plots of φ_{thresh} vs. $\xi^{1/2}$ used to extrapolate the φ_{bn} from IPE-derived φ_{thresh} values for (c) Al_2O_3 and (d) HfO_2.

Next, to determine whether image force barrier lowering is present, Schottky plots of the φ_{thresh} values vs. $\xi^{1/2}$ for the MIM devices from (a) and (b) are shown in (c) and (d) for Al_2O_3 and HfO_2 insulators, respectively, under both positive and negative ξ. The zero-field barrier heights for the Au interfaces ($\varphi_{Bn\text{-}Au}$) and the Ta-based metal interfaces ($\varphi_{Bn\text{-}TaX}$) were determined from the y-axis intersection of extrapolated linear fits of the φ_{thresh}'s. $\varphi_{Bn's}$ and top-bottom barrier differences ($\Delta\varphi_{Bn}$) for each insulator are listed in Table 3.1.

Although the φ_{thresh} values are field dependent, the slopes of the Schottky plots do not correlate with the insulator dielectric constant for any of the devices tested. An absence of image-force barrier lowering for IPE measurements is not unusual and has previously been reported in IPE of metal-insulator interfaces where it was attributed to interfacial charge or to the presence of an interfacial layer.[24,30–32] A plane of charge located near the injecting interface can effectively "pin" the top of the barrier reducing the influence of electric field on the barrier height.[18] Likewise, a higher κ interfacial oxide at the injecting interface can also reduce expected electric field lowering.[29]

Table 3.1: Barrier heights extracted from devices with Au top electrodes, compared to literature values for the respective Au barrier height. Measured barrier heights are given with an expected error of +/- 0.1 eV. Electron affinities from literature are provided.

Insulator (χ_i)	**Measured φ_{Bn} (+/- 0.1 eV)**				**Literature**
	TaN	**TaWSi**	**TaNiSi**	**Au (TaN, TaWSi, TaNiSi)**	**$\varphi_{Bn,Au}$ (eV)**
Al_2O_3 (1.4 eV [33])	2.9	3.1	3.3	4.0, 4.1, 3.9	**4.1** [30]
HfO_2 (2.25 eV [34])	2.9	3.0	3.0	3.5, 3.5, 3.4	**3.7** [31]

Note that there are two non-idealities that can be seen in the yield curves in (a) and (b). First, the yield curves for the barrier between HfO_2 and the top electrode show "tailing" at photon energies below the spectral threshold. This has been reported previously and may be attributed to conduction band tailing or charge in the HfO_2.[14,30] Second, the low positive bias yield curves (emission from the bottom electrode) for HfO_2 shows a rollover at high photon energies that appears most prominently with TaN bottom electrodes. This was also seen in our previous report of SiO_2 devices with the same electrodes.[35] The rollover becomes less prominent with increasing applied positive bias. It is likely that this rollover at high photon energy is due to photoelectron emission from the top Au electrode overwhelming emission from the bottom TaN electrode when there is a low positive bias / weak field across the insulator. At higher positive biases, the insulator field will repel photoelectrons back into the Au electrode. The reasons for stronger emission from the Au electrode at large photon energy are (i) photon absorption and thus photoelectron generation in the top electrode is much stronger than in the bottom electrode and (ii) the Au barrier heights are larger than the TaN barrier heights so that photoemission over the Au/insulator barrier does not start until higher photon energies.

Energy band diagrams based on the experimentally determined φ_{Bn} values listed in Table 3.1 are shown in Fig. 3.2. There are several interesting aspects of these results. At the top electrode, the Au/insulator barrier heights are consistent for each insulator (within the +/- 0.1 eV error), regardless of the bottom electrode used. Additionally, the $\varphi_{Bn,Au}$ value of ~ 4.0 eV for Al_2O_3 is roughly consistent with the ideal Schottky model prediction ($\varphi_{Bn,Au\text{-}ideal} = \Phi_M - \chi_I$) given $\Phi_{Au} \sim 5.2$ eV and $\chi_{\mathrm{Al2O3}} \sim 1.4$.[33] The $\varphi_{Bn,Au}$ of ~ 3.5 eV for HfO_2, however, is higher than expected from the ideal theory prediction by about 1.1 eV.[34] φ_{Bn} values for both Au barriers are roughly consistent with previous IPE reports.

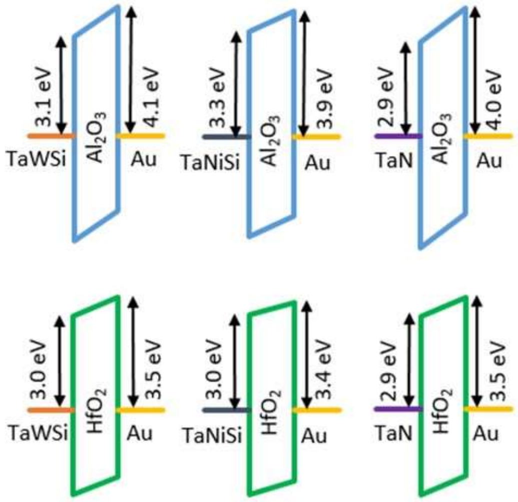

Figure 3.2: IPE based energy band diagrams for Al_2O_3 and HfO_2 MIM devices with Au top electrodes and TaWSi, TaNiSi, or TaN bottom electrodes as indicated.

Considering next the Ta-based metal bottom electrodes, previous Kelvin probe work with TaWSi has determined Φ_{TaWSi} = 5.06 eV.[36] Based on the average vacuum work functions of the constituent metals, it is expected that TaNiSi should have larger barrier heights than TaWSi which in turn should have larger barrier heights than TaN. This expected relative trend of $\varphi_{Bn,TaNiSi} > \varphi_{Bn,TaWSi} > \varphi_{Bn,TaN}$ is indeed observed for Al_2O_3. For HfO_2, however, the barrier heights are essentially the same for all three metals ($\varphi_{Bn,TaNiSi} \approx \varphi_{Bn.TaWSi} \approx \varphi_{Bn.TaN}$). Prior IPE work also appears to show a lack of a trend between various Φ_M metals and $\varphi_{Bn,M/HfO2}$.[18]

The insensitivity of the HfO_2 barrier heights to the various metals suggests that a strong degree of E_{Fm} pinning at E_{CNL} is likely occurring at the HfO_2 interfaces. To quantify the degree of pinning, the slope parameter, S, from Eqn. (2) is determined from the plots of φ_{Bn} versus $\Phi_{M,vac}$ (Au, Al, and TaWSi) shown in Fig. 3.3 for (a) HfO_2 and (b) Al_2O_3. For HfO_2, considering experimental error, an S_{HfO2} range roughly between 0.44 to

0.69 is found with $S_{HfO2} = 0.56$ giving the best fit and shown by the dashed line in 3(a). This value is consistent with the 0.53 calculated by Robertson *et al.*,[37] as well as reported experimental values of around 0.5.[21,38] While the $S_{Al2O3} = 0.89$ determined from 3(b) is considerably higher than the calculated value of 0.63,[37] it is in reasonably good agreement with the 0.83 value reported based on more recently measured IPE barrier heights from the literature.[18]

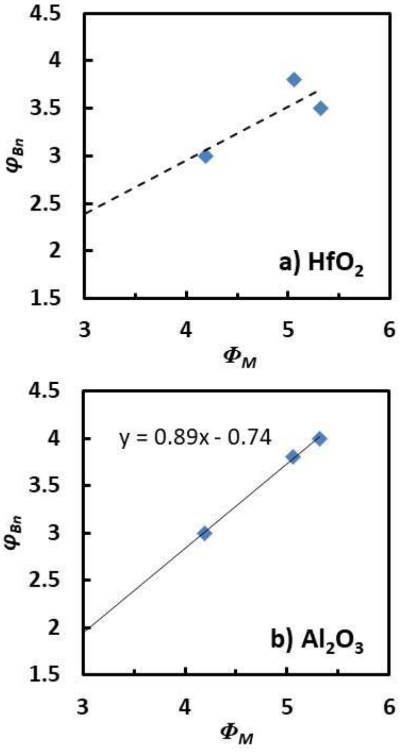

Figure 3.3: Plots of φ_{Bn} vs. Φ_M (Al, Au, and TaWSi) for (a) HfO_2 and (b) Al_2O_3

According to Mönch,[20] S may also be correlated with the high-frequency dielectric constant (ε_∞) of an insulator as

$$S = \frac{1}{1+0.1(\varepsilon_{\infty-1})^2}. \tag{3}$$

This empirical relation reveals that as ε_∞ increases, S decreases indicating that E_{Fm} is more effectively pinned at $E_{CNL,i}$. The fact that $\varepsilon_{\infty,HfO2} > \varepsilon_{\infty,Al2O3}$ explains in part why $S_{HfO2} < S_{Al2O3}$ and why barrier heights on HfO_2 are relatively independent of $\Phi_{M,vac}$. As ε_∞ is also influenced by film morphology and crystallographic direction, it is likely that much of the difference between the theoretical calculation of the S parameter for Al_2O_3 and the value found in this work is because the calculations were performed for crystalline Al_2O_3, which has a higher dielectric constant than the thin film amorphous Al_2O_3 deposited in this work. Using S values determined in this work and Eqn. 3 yields $\varepsilon_{\infty,HfO2} = 3.8$ and $\varepsilon_{\infty,Al2O3} = 2.1$. These values are both slightly lower than the range of 4.2-4.5 for HfO_2 and 2.5-3.0 for Al_2O_3 that were estimated from the square of the ellipsometric refractive index (R.I.^{2}) for similarly deposited materials,[9] and may point to the presence of low κ interfacial layer at the Ta based metal interface.[38]

Since we are directly measuring φ_{Bn}, rather than $\Phi_{M,eff}$, Eqn. (1) can be rewritten as

$$\varphi_{Bn} = S\Phi_{M,vac} - \left(\chi_i - \mathrm{E}_{CNL}(1-S)\right),^{39} \tag{4}$$

assuming that the E_{CNL} is referenced to the vacuum level, E_{vac}, rather than the insulator valence band edge, E_v. By finding the y-intercept of a linear regression of the data in Fig. 3.3 and assuming $\chi_{HfO2} = 2.25$ eV[34] and $\chi_{Al2O3} = 1.4$ eV,[33] we roughly estimate $E_{CNL\text{-}vac,HfO2} = 6.3\text{-}7.6$ eV and $E_{CNL\text{-}vac,Al2O3} = 6.2$ eV, both referenced to E_{vac}. Assuming $E_{G,HfO2} = 5.6$ eV and $E_{G,Al2O3} = 6.4$ eV,[9] typical values for ALD films, this translates to a rough estimate of $E_{CNL\text{-}v,HfO2} = 0.25\text{-}1.6$ eV and $E_{CNL\text{-}v,Al2O3} = 1.6$ eV, referenced to E_v. Robertson calculated $E_{CNL\text{-}v}$ values of 3.7 and 5.5 eV for HfO_2 and Al_2O_3, respectively.[37] Using $\Phi_{M,eff}$ values extracted from flatband voltage shifts of capacitance-voltage measurements on arrays of MOS structures, Yeo et al.[21] report experimental E_{CNL} values of 3.64 and 6.62 eV for HfO_2 and Al_2O_3, respectively, while Samavedam et al.[38] reported values of 4.5 and 5.2 eV for HfO_2 and Al_2O_3, respectively, all referenced to E_v. Clearly the E_{CNL} values determined here are significantly lower than these previous reports. It is important to note that the calculations were performed for crystalline systems,[37] where the ALD thin films in this work are amorphous. In addition, all of the previous reports assume the crystalline $E_{G,Al2O3}$ = 8.8 eV, much larger than the 6.4 eV measured by reflection electron energy loss spectroscopy (REELS) for similarly deposited unannealed ALD Al_2O_3 used in this work and the 6.4-6.9 eV values typically reported for unannealed ALD Al_2O_3.[9,40] For example, the $E_{CNL,Al2O3}$ = 6.62 eV reported by Yeo et al. would be above the conduction band of ALD Al_2O_3. The discrepancy between the E_{CNL} values in this work and previously reported values is likely attributable to extrinsic effects. Whereas the MIGS model described by Eqn. 1 is based entirely on ideal intrinsic induced interface states, barrier heights in real devices may be heavily influenced by *extrinsic* effects due to processing, etc., such as interface trap point defects,[41] additional dipoles due to interfacial chemical reactions, interface layer formation, trapped charge in the dielectric near the interface, and remote oxygen scavenging from the opposing metal electrode.[42] In this work, no post-deposition anneal is performed. In addition, MIM rather than MOS structures were used.

The absolute magnitudes of the extracted barrier heights for the Ta-based metals are much lower than predicted by the ideal model ($\varphi_{Bn\text{-}ideal} = \Phi_M - \chi_I$) based on their vacuum metal work functions. Two possible explanations to consider for the reduced barriers are hole emission and charge in the dielectric.

Although there are no reports of experimental IPE of holes from a metal into an insulator with a barrier above 2 eV,[29,43] it worth considering whether the lower than expected barrier measurements might be explained instead by hole emission from the Au electrode rather than electron emission from the bottom electrode. In this were the case, the measured barrier height would correspond to the Au/insulator hole barrier height ($\varphi_{Bp,Au/HfO2}$) rather than the TaWSi/insulator electron barrier height. Considering first HfO_2, the bandgap of HfO_2 should be equal to the sum of the electron and hole barriers: $E_{G,HfO2} = \varphi_{Bn,Au/HfO2} + \varphi_{Bp,Au/HfO2}$. The $\varphi_{Bn,Au/HfO2}$ measured is 3.5 eV (close to the 3.7 eV reported in [30]). The E_G for these films was measured to be 5.6 eV via REELS,[9] consistent with other reports for ALD HfO_2. Thus the expected $\varphi_{Bp,Au/HfO2} = E_{G,HfO2} - \varphi_{Bn,Au/HfO2} = 5.6$ eV – 3.5 eV = 2.2 eV. This is well below the $\varphi_{Bn,TaWSi/HfO2} = 3.0$ eV barrier measured in Fig. 3.1, evidence that the measured HfO_2 barrier is indeed due to electrons rather than holes. For Al_2O_3, $E_{G,\ Al2O3} = \varphi_{Bn,Au/Al2O3} + \varphi_{Bp,Au/Al2O3}$. The measured $\varphi_{Bn,Au/Al2O3} = 4.1$ eV +/- 0.1 eV. The E_G for these films was measured via REELS to be 6.4 eV,[9] consistent with other reports for ALD Al_2O_3.[30] Thus the expected $\varphi_{Bp,Au/Al2O3} = E_{G,\ HfO2} - \varphi_{Bn,Au/Al2O3} = 6.4$ eV – 4.1 eV = 2.3 eV. The is well below the $\varphi_{Bn,TaWSi/Al2O3} = 3.1$ eV barrier measured in Fig. 3.1, evidence that the measured Al_2O_3 barrier is also due to electrons rather than holes.

Considering oxide charge, previous work with Ta-based metals postulated that negative Ta ion migration into the oxide following a post-deposition anneal could lead to an increase in barrier height.[44] While Ta diffusion could be playing a role, barrier heights here are reduced, rather than increased. Previous work has also shown that hole trapping ($\sim 10^{12}$ / cm^2) can result in a local reduction of barrier height by 0.3 eV and Li^+ ions

(~10^{14} / cm^2) can reduce barrier heights by up to1 eV.[29] Positively charged Au^+ ions are known to migrate rapidly through oxides and have even been shown to form conductive bridges that enable switching behavior in conductive bridging random access memory (CBRAM).[45,46] Determination of the bottom electrode barrier heights in this work is performed with a positive bias applied to the Au top electrodes over a relatively long period of time (hours compared to less than a second for CBRAM devices), giving ample time for Au^+ ions to drift to the bottom electrode where they would contribute to a reduction in barrier height. In fact, in support of this possibility, we have observed reversible breakdown / resistive switching behavior in the Au/SiO_2/TaWSi devices whereas the Al/SiO_2/TaWSi devices did not show switching.[35]

To assess whether Au may be impacting the extracted barrier heights of the opposing Ta based electrodes, Al was used as a top electrode for devices with a TaWSi bottom electrode and either Al_2O_3 or HfO_2. Shown in Fig. 3.4 are representative yield plots of $Y^{1/2}$ vs. $h\nu$ for Al top electrode MIM devices with (a) Al_2O_3 and (b) HfO_2 insulators and TaWSi bottom electrodes. Schottky plots of the φ_{thresh} values vs. $\xi^{1/2}$ for these devices are shown in (c). Note that the yield curve for the HfO_2 barriers in (b) shows tailing at photon energies below the indicated spectral threshold and, as is typically reported for IPE of metal/insulator interfaces, the slopes of the Schottky plot of electric field barrier lowering in (c) do not correspond to the dielectric constant of the insulator.[45] Both of these observations are consistent with our previous IPE measurements on ZrCuAlNi amorphous metal bottom electrode / Al top electrode devices[14] and have been attributed to either conduction band tailing / defects, charged defect levels, or an interfacial layer (IL) oxide at the injecting interface.[24,30–32,45] Conduction band tailing is likely not solely responsible for the observed IPE threshold tailing as the energy spread of the tail is about 1 eV, larger than what would be typically expected for band tailing, though oxygen vacancy related defects have been detected using REELS at roughly 2 eV above the valance band edge in Ar^+ sputtered HfO_2.[9] Potential contributions from ILs would be either an Al_2O_3 IL at the top Al interface and a TaO_x IL at the Ta-based metal interface.[47] Given that the tailing was also seen with Al top electrodes and ZrCuAlNi bottom electrodes (which do not contain Ta), both a TaO_x and Al_2O_3 ILs can be ruled out as the major source of tailing. Charge in the dielectric seems the most likely explanation as lateral charge non-uniformities can cause IPE threshold tailing. As previously discussed, Au^+ charge in the insulator may also be responsible for the reduction of barrier height in the Au top electrode devices. In addition, charge at the interface can reduce influence of electric field on barrier height.[18]

Table 3.2: Barrier heights extracted from devices in this work with Al top electrodes, compared to literature values for the respected Al barrier height. Measured barrier heights are given with an expected error of +/- 0.1 eV.

Insulator (χ_i)	**Measured φ_{Bn} (+/- 0.1 eV)**		**Literature**
	TaWSi	**Al**	**$\varphi_{Bn,Al}$ (eV)**
Al_2O_3 (1.4 eV [33])	3.8	3.0	**2.9** [30]
HfO_2 (2.25 eV [34])	3.8	3.0	**2.5** [31]

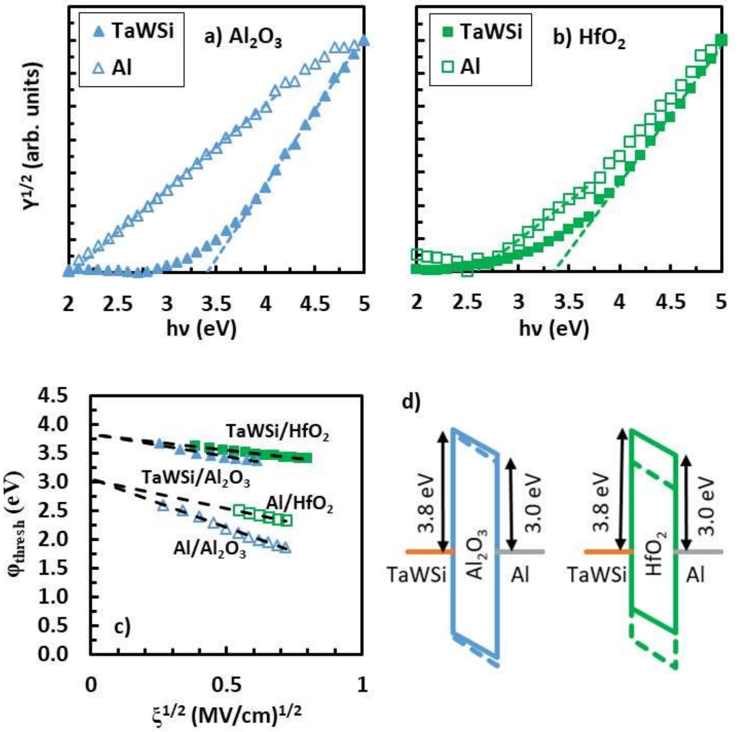

Figure 3.4: Representative plots of $Y^{1/2}$ vs. *hv* for (a) Al$_2$O$_3$ and (b) HfO$_2$ in MIM devices with Al top electrodes and TaWSi bottom electrodes, where the dashed lines show the linear φ_{thresh} extraction for each interface. Each plot shown was taken at an applied field in the range of 0.4 to 1.2 |MV^2/cm^2|. (c) Schottky plots of φ_{thresh} vs. $\xi^{1/2}$ used to extrapolate the φ_{Bn} from IPE-derived spectral thresholds for the indicated interface, and (d) the IPE based (solid lines) vs. ideal (dashed lines) band diagrams.

The φ_{Bn} values for each insulator are listed in Table 3.2. In Fig. 3.4(d), energy band diagrams of the Al top gate devices based on the experimentally determined φ_{Bn} values from Table 3.2 (solid lines) are superimposed on band diagrams predicted by $\varphi_{Bn} = \Phi_M - \chi_I$ (dashed lines). We find much larger (~0.7–0.8 eV) TaWSi/insulator barriers than for Au top electrode devices, suggesting that Au$^+$ ion migration may indeed play a role in reducing opposing electrode barrier heights.

The Al top gate TaWSi/Al$_2$O$_3$ φ_{Bn} (3.8 eV) is within error equivalent to that predicted by the ideal Schottky model. The TaWSi/HfO$_2$ φ_{Bn}, on the other hand, is higher than the Schottky model prediction by about 0.9 eV. For HfO_2, the φ_{Bn} increase over the ideal model for both TaWSi bottom and Al top electrodes is similar, with an approximately 0.8-0.9 eV increase. This points to negative fixed charge in the HfO_2 or perhaps formation of an Al_2O_3 IL at the top Al electrode. Comparing the Al with the Au top electrode devices, it is seen that the Al/insulator barrier heights are smaller than the Au/insulator barrier heights for all insulators. For both HfO_2 and Al_2O_3, this difference is roughly equal to the expected $\Phi_{M,vac}$ difference between Au and Al ($\Delta\Phi_{Au\text{-}Al} \sim 0.9$ eV). Comparing to our previous work with a ZrCuAlNi bottom electrode, the Al/insulator barrier heights are equal, within experimental error.[14] The TaWSi barriers are 0.8 eV and 0.6 eV greater than that measured for ZrCuAlNi with Al_2O_3 and HfO_2, respectively,[14] confirming that TaWSi has a larger effective workfunction than ZrCuAlNi.

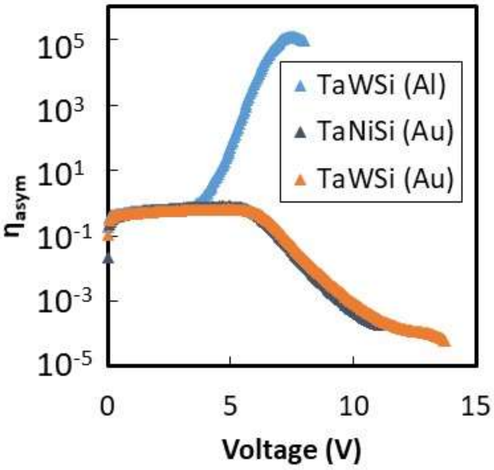

Figure 3.5: Voltage vs. current asymmetry for Al_2O_3 MIM devices with the indicated bottom (top) electrodes.

Finally, the goal of this work is to use IPE to directly measure metal/semiconductor φ_{Bn}'s in a device stack so as to be able to better predict device behavior. For high quality ALD Al_2O_3, thick enough so that conduction is not dominated by direct tunneling, and moderate to high Φ_M electrodes, Fowler-Nordheim tunneling (FNT) dominates conduction. The onset of FNT appears as a distinct "knee" in the current density vs. voltage curve, at a voltage dependent on φ_{Bn} of the electrode opposite the injecting electrode and the thickness of the insulator. Above the knee, the magnitude of conduction with the bottom electrode held at ground and positive (negative) bias applied to the top electrode depends inversely on $\varphi_{Bn,bottom}$ ($\varphi_{Bn,top}$). In other words, the greater the conduction, the smaller the barrier height at the injecting electrode. Therefore, by looking at asymmetry, defined here as the negative bias current over the positive bias current at the same absolute voltage ($\eta_{\mathrm{asym}} = I^-/I^+$), the relative size of the barriers may be assessed. $\eta_{\mathrm{asym}} > 1$ indicates that the barrier height of the top electrode is less than the bottom electrode, $\varphi_{Bn,\ top} < \varphi_{Bn,bottom}$, meaning $\Phi_{eff,top} < \Phi_{eff,bottom}$ and $\eta_{\mathrm{asym}} < 1$ indicates that $\Phi_{eff,top} > \Phi_{eff,bottom}$. Shown in Fig. 3.5 are plots of η_{asym} vs. voltage for Al_2O_3 MIM devices with either TaWSi or TaNiSi amorphous metal bottom electrodes and either Au or Al top electrodes. For TaWSi bottom electrode devices, $\eta_{\mathrm{asym}} > 1$ for an Al top electrode and $\eta_{\mathrm{asym}} < 1$ for a Au top electrode, indicating that $\Phi_{eff,Al} < \Phi_{eff,TaWsi} < \Phi_{eff,Au}$ and that $\varphi_{Bn,Al} < \varphi_{Bn,TaWSi} < \varphi_{Bn,Au}$. $\eta_{\mathrm{asym}} < 1$ is also seen for the TaNiSi/Al_2O_3/Au device. These results are inconsistent with ideal Schottky model predictions, but consistent with our IPE measurements which show $\Delta\varphi_{\mathrm{Bn,\ TaWSi\text{-}Au}} = -1.0$ eV, $\Delta\varphi_{\mathrm{Bn,\ TaWSi\text{-}Al}} = +0.8$ eV, and $\Delta\varphi_{\mathrm{Bn,\ TaNiSi\text{-}Au}} = -0.6$ eV.

3.4 Summary and Conclusion

The electron energy barrier heights between two recently reported Ta-based amorphous metals (TaWSi and TaNiSi), TaN, and ALD Al_2O_3 and HfO_2 insulators with

Al top electrodes are measured experimentally using internal photoemission (IPE) spectroscopy. A comparison is also made between Al and Au top electrodes for devices with a TaWSi bottom electrode. The measured barrier heights for both the Al and Au top electrodes are near the Schottky model values ($\varphi_{Bn} = \Phi_M - \chi_I$) and consistent with previous IPE reports for each insulator. For the Ta-based metal bottom electrodes with Al_2O_3, φ_{Bn} increases with increasing Φ_M: φ_{Bn} = 2.9, 3.1, and 3.1 eV for TaN, TaWSi, and TaNiSi, respectively. For HfO_2, however, the barrier heights are relatively independent of Φ_M: $\varphi_{Bn,TaNiSi} \approx \varphi_{Bn.TaWSi} \approx \varphi_{Bn.TaN} \approx 3.0$ eV. The difference between HfO_2 and Al_2O_3 is attributed to enhanced Fermi-level pinning due to a larger dielectric constant – confirmed by the slope parameter, S, which was found to be 0.89 and 0.44-0.69 for Al_2O_3 and HfO_2, respectively. In devices with a TaWSi bottom electrode, an Au top electrode lead to significantly lower barrier heights than were obtained with Al, 0.6 eV and 0.8 eV lower for HfO_2 and Al_2O_3, respectively. Measurements of the current-voltage asymmetry of MIM diodes are consistent with the IPE measured barriers, whereas the asymmetry is inconsistent with the Schottky model predictions of barrier heights.

A comparison to previous work with amorphous ZrCuAlNi bottom and Al top electrodes indicates that the electron barriers for TaWSi with HfO_2 and Al_2O_3 are 0.8 eV and 0.6 eV greater, respectively, than the same barriers with ZrCuAlNi. This confirms that for Al_2O_3, TaWSi has a larger effective work function than ZrCuAlNi, ~5.2 eV vs. ~4.7 eV, respectively.[14] Combined with low roughness and significantly higher temperature stability than ZrCuAlNi (greater than 900 °C vs. less than 400 °C), TaWSi appears promising for use as a high work function bottom electrode in MIM device applications.

3.5 Acknowledgements

This work was supported by NSF Center for Sustainable Materials Chemistry, grant CHE-1606982. The authors thank C. Tasker for equipment support and T. Klarr (now at Micron, Boise, ID) for device fabrication assistance. Part of this work was conducted at the Materials Synthesis and Characterization (MaSC) Center, a National Nanotechnology Coordinated Infrastructure (NNCI) Northwest Nanotechnology Infrastructure (NWNI) user facility at Oregon State University, which is supported in part by the National Science Foundation (Grant ECC-1542101) and Oregon State University.

3.6 References

[1] A. Sharma, V. Singh, T.L. Bougher, and B.A. Cola, "A Carbon Nanotube Optical Rectenna," Nat. Nanotechnol. **10**, 1027 (2015).

[2] M. Bareib, B.N. Tiwari, A. Hochmeister, G. Jegert, U. Zschieschang, H. Klauk, B. Fabel, G. Scarpa, G. Koblmuller, G.H. Bernstein, W. Porod, and P. Lugli, "Nano Antenna Array for Terahertz Detection," IEEE Trans. Microw. Theory Tech. **59**, 2751 (2011).

[3] G. Moddel and S. Grover, *Rectenna Solar Cells*, (Springer Science & Business Media, New York, 2013).

[4] M. Heiblum, "Tunneling Hot Electron Transfer Amplifiers (Theta): Amplifiers Operating up to the Infrared," Solid-State Electron. **24**, 343 (1981).

[5] S. Vaziri, A.D. Smith, M. Östling, G. Lupina, J. Dabrowski, G. Lippert, W. Mehr, F. Driussi, S. Venica, V. Di Lecce, A. Gnudi, M. König, G. Ruhl, M. Belete, and M.C.

Lemme, “Going Ballistic: Graphene Hot Electron Transistors,” Solid State Commun. **224**, 64 (2015).

[6] G. Karbasian, M.S. McConnell, H. George, L.C. Schneider, M.J. Filmer, A.O. Orlov, A.N. Nazarov, and G.L. Snider, “Metal-Insulator-Metal Single Electron Transistors with Tunnel Barriers Prepared by Atomic Layer Deposition,” Appl. Sci. **7**, 246 (2017).

[7] H.-S.P. Wong, H.-Y. Lee, S. Yu, Y.-S. Chen, Y. Wu, P.-S. Chen, B. Lee, F.T. Chen, and M.-J. Tsai, “Metal-Oxide RRAM,” Proc. IEEE **100**, 1951 (2012).

[8] D.Z. Austin, K.E.K. Holden, J. Hinz, and J.F. Conley, Jr., “Electrode Modulated Capacitance-Electric Field Nonlinearity in Metal-Insulator-Metal Capacitors,” Appl. Phys. Lett. **110**, 263503 (2017).

[9] N. Alimardani, S.W. King, B.L. French, C. Tan, B.P. Lampert, and J.F. Conley, Jr., “Investigation of the Impact of Insulator Material on the Performance of Dissimilar Electrode Metal-Insulator-Metal Diodes,” J. Appl. Phys. **116**, 024508 (2014).

[10] N. Alimardani, E.W. Cowell, J.F. Wager, J.F. Conley, Jr., D.R. Evans, M. Chin, S.J. Kilpatrick, and M. Dubey, “Impact of Electrode Roughness on Metal-Insulator-Metal Tunnel Diodes with Atomic Layer Deposited Al2O3 Tunnel Barriers,” J. Vac. Sci. Technol. A **30**, 01A113 (2012).

[11] A.A. Khan, G. Jayaswal, F.A. Gahaffar, and A. Shamim, “Metal-Insulator-Metal Diodes with Sub-Nanometre Surface Roughness for Energy-Harvesting Applications,” Microelectron. Eng. **181**, 34 (2017).

[12] E.W. Cowell, N. Alimardani, C.C. Knutson, J.F. Conley, Jr., D.A. Keszler, B.J. Gibbons, and J.F. Wager, “Advancing MIM Electronics: Amorphous Metal Electrodes,” Adv. Mater. **23**, 74 (2011).

[13] N. Alimardani and J.F. Conley, Jr., “Enhancing Metal-Insulator-Insulator-Metal Tunnel Diodes via Defect Enhanced Direct Tunneling,” Appl. Phys. Lett. **105**, 082902 (2014).

[14] M.A. Jenkins, T. Klarr, D.Z. Austin, W. Li, N.V. Nguyen, and J.F. Conley, Jr., “Assessment of Energy Barriers Between ZrCuAlNi Amorphous Metal and Atomic Layer Deposition Insulators Using Internal Photoemission Spectroscopy,” Phys. Status Solidi RRL – Rapid Res. Lett. **12**, 1700437 (2018).

[15] J.M. McGlone, K.R. Olsen, W.F. Stickle, J.E. Abbott, R.A. Pugliese, G.S. Long, D.A. Keszler, and J.F. Wager, “TaWSi Amorphous Metal Thin Films: Composition Tuning to Improve Thermal Stability,” MRS Commun. **7**, 715 (2017).

[16] J.M. McGlone, K.R. Olsen, W.F. Stickle, J.E. Abbott, R.A. Pugliese, G.S. Long, D.A. Keszler, and J.F. Wager, “Ta-Based Amorphous Metal Thin Films,” J. Alloys Compd. **650**, 102 (2015).

[17] V. Afanas’ev, N. Kolomiiets, M. Houssa, and A. Stesmans, “Internal Photoemission Metrology of Inhomogeneous Interface Barriers,” Phys. Status Solidi A 1700865 (2017).

[18] V.V. Afanas’ev and A. Stesmans, “Internal Photoemission at Interfaces of High-κ Insulators with Semiconductors and Metals,” J. Appl. Phys. **102**, 081301 (2007).

[19] J. Tersoff, “Schottky Barrier Heights and the Continuum of Gap States,” Phys. Rev. Lett. **52**, 465 (1984).

[20] W. Mönch, "Role of Virtual Gap States and Defects in Metal-Semiconductor Contacts," Phys. Rev. Lett. **58**, 1260 (1987).

[21] Y.-C. Yeo, T.-J. King, and C. Hu, "Metal-Dielectric Band Alignment and Its Implications for Metal Gate Complementary Metal-Oxide-Semiconductor Technology," J. Appl. Phys. **92**, 7266 (2002).

[22] V.K. Adamchuk and V.V. Afanas'ev, "Internal Photoemission Spectroscopy of Semiconductor-Insulator Interfaces," Prog. Surf. Sci. **41**, 111 (1992).

[23] N.V. Nguyen, O.A. Kirillov, W. Jiang, J.E. Maslar, W. Kimes, and J.S. Suehle, "Interface Barrier Determination by Internal Photoemission: Applications to Metal/Oxide/Semiconductor Structure," ECS Trans. **13**, 161 (2008).

[24] V.V. Afanas'ev, A. Stesmans, L. Pantisano, S. Cimino, C. Adelmann, L. Goux, Y.Y. Chen, J.A. Kittl, D. Wouters, and M. Jurczak, "TiNx/HfO2 Interface Dipole Induced by Oxygen Scavenging," Appl. Phys. Lett. (2011).

[25] W. Ludwig and B. Kornefpel, "Photoemission Studies on Thin Metal-Insulator-Metal Sandwiches," Phys. Status Solidi B **24**, K137 (1967).

[26] K.H. Gundlach and J. Kadlec, "Spectral Dependence of the Photoresponse in MIM Structures: Influence of the Electrode Thickness," Thin Solid Films **28**, 107 (1975).

[27] J. Kadlec and K.H. Gundlach, "Results and Problems of Internal Photoemission in Sandwich Structures," Phys. Status Solidi A **37**, 11 (1976).

[28] N.V. Nguyen, O. Kirillov, H.D. Xiong, and J.S. Suehle, "Internal Photoemission Spectroscopy of Metal Gate/High-k/Semiconductor Interfaces," in *AIP Conf. Proc.* (AIP Publishing, 2007), pp. 308–314.

[29] V.V. Afanas'ev, *Internal Photoemission Spectroscopy: Fundamentals and Recent Advances*, (Elsevier, 2014).

[30] V.V. Afanas'ev, M. Houssa, A. Stesmans, and M.M. Heyns, "Band Alignments in Metal–Oxide–Silicon Structures with Atomic-Layer Deposited Al2O3 and ZrO2," J. Appl. Phys. **91**, 3079 (2002).

[31] V.V. Afanas'ev, A. Stesmans, F. Chen, X. Shi, and S.A. Campbell, "Internal Photoemission of Electrons and Holes from (100)Si into HfO2," Appl. Phys. Lett. **81**, 1053 (2002).

[32] J. Widiez, K. Kita, K. Tomida, T. Nishimura, and A. Toriumi, "Internal Photoemission over HfO2 and Hf(1-x)SixO2 High-k Insulating Barriers: Band Offset and Interfacial Dipole Characterization," Jpn. J. Appl. Phys. **47**, 2410 (2008).

[33] S. Swaminathan, Y. Sun, P. Pianetta, and P.C. McIntyre, "Ultrathin ALD-Al2O3 Layers for Ge(001) Gate Stacks: Local Composition Evolution and Dielectric Properties," J. Appl. Phys. **110**, 094105 (2011).

[34] S. Monaghan, P.K. Hurley, K. Cherkaoui, M.A. Negara, and A. Schenk, "Determination of Electron Effective Mass and Electron Affinity in HfO2 Using MOS and MOSFET Structures," Solid-State Electron. **53**, 438 (2009).

[35] M.A. Jenkins, T. Klarr, J.M. McGlone, J.F. Wager, and J.F. Conley, Jr., "Internal Photoemission Spectroscopy Measurements of the Energy Barrier Heights between ALD SiO2 and Ta-Based Amorphous Metals," ECS Trans. **85**, 729 (2018).

[36] J.M. McGlone, "Thermally-Stable Amorphous Metal Thin Films," Thermally-Stable Amorphous Metal Thin Films, Masters Thesis, Oregon State University, 2014.

[37] J. Robertson, “Band Offsets of Wide-Band-Gap Oxides and Implications for Future Electronic Devices,” J. Vac. Sci. Technol. B **18**, 1785 (2000).

[38] S.B. Samavedam, L.B. La, P.J. Tobin, B. White, C. Hobbs, L.R.C. Fonseca, A.A. Demkov, J. Schaeffer, E. Luckowski, A. Martinez, M. Raymond, D. Triyoso, D. Roan, V. Dhandapani, R. Garcia, S.G.H. Anderson, K. Moore, H.H. Tseng, C. Capasso, O. Adetutu, D.C. Gilmer, W.J. Taylor, R. Hegde, and J. Grant, “Fermi Level Pinning with Sub-Monolayer MeOx and Metal Gates [MOSFETs],” in *Electron Devices Meet. 2003 IEDM 03 Tech. Dig. IEEE Int.* (2003), pp. 13.1.1-13.1.4.

[39] J.F. Wager and K. Kuhn, “Device Physics Modeling of Surfaces and Interfaces from an Induced Gap State Perspective,” Crit. Rev. Solid State Mater. Sci. **42**, 373 (2017).

[40] X. Qin and R.M. Wallace, “In Situ Plasma Enhanced Atomic Layer Deposition Half Cycle Study of Al2O3 on AlGaN/GaN High Electron Mobility Transistors,” Appl. Phys. Lett. **107**, 081608 (2015).

[41] P.M. Lenahan and J.F. Conley Jr, “What Can Electron Paramagnetic Resonance Tell Us about the Si/SiO2 System?,” J. Vac. Sci. Technol. B **16**, 2134 (1998).

[42] L. Pantisano, V.V. Afanas’ev, S. Cimino, C. Adelmann, L. Goux, Y.Y. Chen, J.A. Kittl, D. Wouters, and M. Jurczak, “Towards Barrier Height Modulation in HfO2/TiN by Oxygen Scavenging – Dielectric Defects or Metal Induced Gap States?,” Microelectron. Eng. **88**, 1251 (2011).

[43] R.J. Powell, “Photoinjection into SiO2: Use of Optical Interference to Determine Electron and Hole Contributions,” J. Appl. Phys. **40**, 5093 (1969).

[44] S. Shamuilia, V.V. Afanas'ev, A. Stesmans, T. Schram, and L. Pantisano, "Internal Photoemission of Electrons from Ta-Based Conductors into SiO2 and HfO2 Insulators," J. Appl. Phys. **104**, 073722 (2008).

[45] J.G. Simmons and R.R. Verderber, "New Conduction and Reversible Memory Phenomena in Thin Insulating Films," Proc R Soc Lond A **301**, 77 (1967).

[46] C.-N. Peng, C.-W. Wang, T.-C. Chan, W.-Y. Chang, Y.-C. Wang, H.-W. Tsai, W.-W. Wu, L.-J. Chen, and Y.-L. Chueh, "Resistive Switching of Au/ZnO/Au Resistive Memory: An in Situ Observation of Conductive Bridge Formation," Nanoscale Res. Lett. **7**, 559 (2012).

[47] M. He and T.-M. Lu, *Metal-Dielectric Interfaces in Gigascale Electronics: Thermal and Electrical Stability*, (Springer, New York, 2012).

4 INTERNAL PHOTOEMISSION SPECTROSCOPY MEASUREMENT OF BARRIER HEIGHTS BETWEEN ATOMIC LAYER DEPOSITED (ALD) RU AND ALD INSULATORS

M.A. Jenkins, M.H. Hayes, and J.F. Conley, Jr.

Manuscript in preparation

4.1 Introduction

Atomic layer deposited metals are of growing interest for applications that require conformal, pinhole free conductive films. ALD metals are particularly of interest for use in high aspect-ratio structures due to the conformal nature of ALD, making them ideal candidates for liners in interconnects. There has also been growing interest in the use of ALD metals for selective deposition of contacts, where selective deposition may be performed using inhibitors or inherently selective chemistry of the precursors used. Ruthenium is one such ALD metal of interest due to a relatively low bulk resistivity (~7.1 μΩ-cm) and high work function (4.7 eV). Ruthenium is also easily etched, making for straightforward integration within existing process flows. These properties lead to interest in ALD Ru as a gate electrode for MOS transistors, metal-insulator-metal (MIM) based capacitors, RRAM, and tunnel diodes, as well as a conductive Cu diffusion barrier/liner for Cu interconnects. A recent ALD process for Ru using $Ru(DMBD)(CO)_3$ and O_2 shows near zero nucleation, low roughness, and low resistivity.[1]

For many of the applications listed above, device performance is dependent on the energy barrier height (φ_{Bn}) between the metal electrode and insulator, where φ_{Bn} is ideally defined as

$$\varphi_{Bn} = \Phi_{M,vac} - \chi_i \tag{1}$$

where $\Phi_{M,vac}$ is the metal work function and χ_i is the electron affinity of the insulator. However, this is not generally the real barrier height when these materials are in physical contact with one another due to non-idealities such as dipoles from various sources or interfacial layers. In the case of metal-insulator-semiconductor (MOS) devices, these non-idealities are accounted for with an effective work function, $\Phi_{M,eff}$, which depends on insulator in question. This is of use in MOS devices, specifically, because $\Phi_{M,eff}$ may be measured using capacitance-voltage (CV) measurements on MOS devices. This is achieved by making multiple samples with varying insulator thickness and finding the flatband voltage for each thickness. However, this technique is not viable for MIM devices because the CV output characteristics for MIM devices do not exhibit the same flatband voltage. As such, a technique that directly measures the barrier height is particularly useful for MIM devices, though still useful for MOS devices. Internal photoemission (IPE) spectroscopy is the only analytical technique capable of directly determining φ_{Bn} in device structures.[2-5] Internal photoemission (IPE) spectroscopy is an electro-optical technique that allows for insitu measurement of energy barrier heights at heterojunctions, including metal-insulator interfaces. To date, little IPE work has been reported on ALD metals. In this work, we use IPE to directly measure the φ_{Bn} between ALD dielectrics and ALD Ru deposited using Ru(DMBD)$(CO)_3$ and O_2.

4.2 Experimental

Metal-oxide-semiconductor (MOS) devices were fabricated on n^{++} Si MIM devices on blanket films of either TaN or TiN. TaN bottom electrode substrates (obtained from ON semiconductor, Gresham, OR) consisted of a Si/SiO_2/Ta/TaN stack that was planarized via chemical mechanical polishing. TiN bottom electrode substrates were also provided by ON semiconductor. Insulators were deposited on the bottom electrodes using atomic layer deposition (ALD), targeting a thickness of 10 nm, such that the insulator was thick enough to prevent direct tunneling from dominating charge transport. Al_2O_3 and HfO_2 were deposited using thermal ALD in a Picosun SUNALE R-

150 reactor at 300 °C and 350 °C, respectively. The precursors used for Al_2O_3 and HfO_2 were trimethylaluminum (TMA) and tetrakis(ethylmethylamino)hafnium (TEMA-Hf), respectively, with H_2O as the oxidizing agent. Insulator thickness were measured on Si witness coupons via variable angle spectroscopic ellipsometry (VASE) in a J.A. Woollam M-2000 VASE using a Cauchy model. Approximately 12 nm thick Ru top electrodes were deposited via thermal ALD in a Picosun SUNALE R-200 reactor at 260 °C using $Ru(DMBD)(CO)_3$ and O_2.[1] Following Ru deposition, select samples were annealed in a 5% H_2 / 95% N_2 forming gas atmosphere at 500 °C for 60 minutes.

IPE measurements were conducted using light from a 150 W Xe arc lamp source that was passed through a monochromator, followed by a long-pass filter to remove second-order diffraction. The light was then shined onto the device of interest using a parabolic mirror focused to a spot size of 1 mm^2. Electrical bias was applied to the bottom electrode and the top electrode was held at ground. At each applied bias, the electrical current was measured as the photon energy (hv) was swept from 2 to 5 eV (620-248 nm). The current was normalized by subtracting the dark current for each applied bias, such that only photo-induced current was analyzed. The quantum yield, Y, was calculated from normalized current, and spectral thresholds, φ_{thresh} were determined from plots of $Y^{1/2}$ or $Y^{1/3}$ versus hv using the regions of highest linearity.[2,3] The zero-field barrier height, φ_{Bn}, for each interface was then found as the y-intercept of a Schottky plot of φ_{thresh} vs. the square root of the electric field across the insulator, $\xi^{1/2}$. The $\xi^{1/2}$ values are corrected for the built-in field, ξ_{bi}, of each device, found by determining the field at which the emission current switches polarity. Reported φ_{Bn} values have estimated accuracy of +/- 0.1 eV.

4.3 Results and Discussion

Yield curves for metal-oxide-semiconductor (MOS) devices with Al_2O_3 in the as-deposited state (unannealed) are shown in Fig. 1 A y-axis of $Y^{1/2}$ is used for metal-insulator interface while $Y^{1/3}$ is used for the insulator-semiconductor interface to account for differing energy distributions at the injecting interface: a step function for metals and a ramp function for semiconductors, respectively.[4] The Ru-Al_2O_3 yield curve 9n Fig. 1(a) shows a single linear region, indicating a single barrier with no optical transitions within the photon range in use. As shown in the Schottky plot in Fig. 2, this results in a zero-field barrier height, $\varphi_{bn\text{-}Ru/Al2O3}$, of 3.6 eV. Assuming an χ_{Al2O3} of 1.4 eV,[5] this yields $\Phi_{Ru,eff}$ ~ 5.0 eV. To date, $\Phi_{M,eff}$ values for the Ru/Al_2O_3 barrier have been reported only for samples that have undergone a post-metallization anneal, not for as-deposited samples. $\Phi_{M,eff}$ values for annealed Ru have been reported to be ~ 5.0 eV for Al_2O_3,[6] with recent work done on annealed ALD Ru / Al_2O_3 yielding an $\Phi_{M,eff}$ of 4.98 eV.[7] These values are in agreement with the IPE-derived $\Phi_{M,eff}$ obtained here for as-deposited ALD Ru /Al_2O_3.

The Al_2O_3-Si yield curve in Fig. 1(b) shows distinct inflection points at ~3.4 and 4.3 eV, corresponding to the onset of direct optical transitions in the Si and denoted as E_1 and E_2.[8] The barrier height is extracted from the region prior to these optical transitions, yielding a zero-field barrier height, $\varphi_{bn\text{-}Si/Al2O3}$, of 3.1 eV as shown in Fig. 2. Again assuming $\chi_{Al2O3} = 1.4$ eV,[5] this yields $\Phi_{Si,eff} = 4.5$ eV, approximately 0.4 eV higher than the expected Φ_{si} of 4.07 eV as determined from the doping concentration. However, previous IPE results on ALD Al_2O_3 report $\varphi_{bn\text{-}Si/Al2O3} = 3.25$ eV,[2] slightly larger than the value found here. One possible explanation for the higher than expected value obtained for $\Phi_{Si,eff}$ is the presence of a dipole at the interface between the ALD Al_2O_3 and Si. A negative dipole at the interfaces of ALD Al_2O_3 and various metals is commonly reported in IPE measured barrier heights.[9] The slope of the Schottky plot is ideally dependent on the dielectric constant of the insulator, as described by Schottky barrier lowering.[10] The slope of the Schottky plot for a given barrier height can thus be used as an indicator for the presence of dipoles at the interface. In this work, the slope of the Al_2O_3/Si barrier Schottky plot is lower than would be expected from k_{Al2O3}, suggesting the presence of a dipole that decreases the impact of Schottky barrier lowering with increasing electric field. While this dipole has been reported at the interface of ALD insulators and metals, it has not been reported at the ALD Al_2O_3/Si interface.[9]

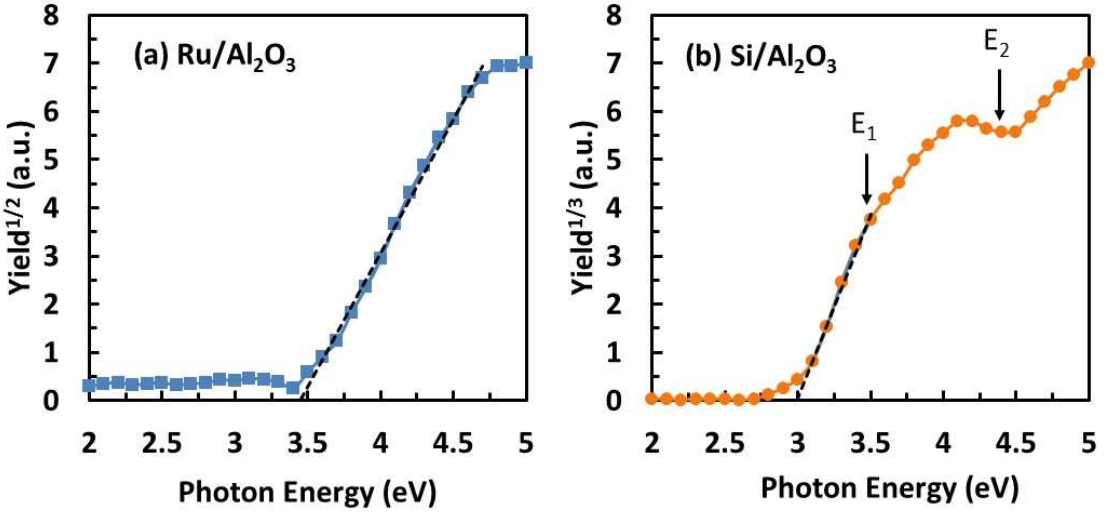

Figure 4.1: Representative yield$^{1/2}$ curves for the as-deposited Ru/Al_2O_3/TaN MOS device for both (a) bottom and (b) top electrode interfaces. Dashed lines guide the eye for regions of φ_{thresh} extraction, with φ_{thresh} extracted at x-intercept.

MIM devices with Ru top electrodes and both TiN and TaN bottom electrodes were also characterized via IPE. Schottky plots for both types of devices are shown in Fig. 3. For the top Ru electrode, the extracted $\varphi_{bn\text{-}Ru/Al2O3}$ was found to be approximately 3.6 and

3.7 eV for TiN and TaN bottom electrodes, respectively, both within experimental error of the 3.6 eV found above for the n^+Si bottom electrode. At the bottom electrode for these MIM devices, $\varphi_{bn\text{-}TaN/Al2O3}$ and $\varphi_{bn\text{-}TiN/Al2O3}$ were within experimental error of one another at 2.9 and 3.0 eV, respectively. $\varphi_{bn\text{-}TaN/Al2O3}$ is also in agreement with reported values.[10]

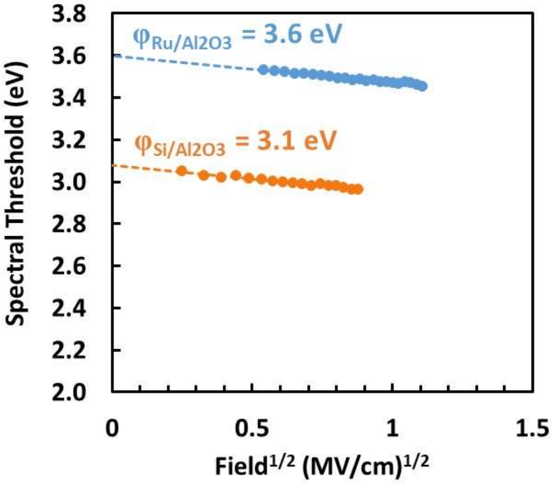

Figure 4.2: Schottky plot for the as-deposited Ru/Al_2O_3/TaN MOS device for top and bottom interfaces. The y-intercept of the dashed lines indicate extrapolated φ_{bn}'s.

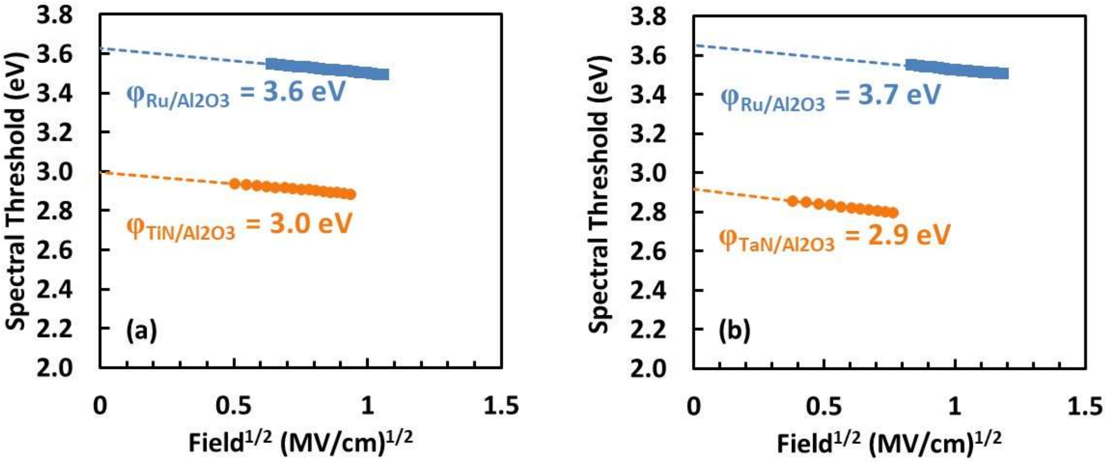

Figure 4.3: Schottky plots for as-deposited (a) Ru/Al_2O_3/TiN and (b) Ru/Al_2O_3/TaN MIM devices. The y-intercept of the dashed line indicates the zero-field barrier heights for top and bottom electrodes.

Shown in Fig. 4 are Schottky plots summarizing IPE measurements of the top and bottom interfaces of (a) Ru/Al_2O_3/TiN and (b) Ru/HfO_2/TaN MIM devices. Measurements on as-deposited Ru/HfO_2/TaN devices yielded $\varphi_{bn\text{-}Ru/HfO2} \simeq 3.8$ eV. Assuming $\chi_{HfO2} = 2.25$ eV,[11] this yields an $\Phi_{Ru,eff}$ of roughly 6.05 eV, much larger than expected from the difference of bulk vacuum work function, Φ_{Ru}, and χ_{HfO2}. As was the case for Al_2O_3 above, this could be due to the presence of a negative dipole at the ALD HfO_2 / metal interface, which has been reported in previous work.[9]

In our prior work, ALD HfO_2 and Al_2O_3 have been shown to have similar barrier heights when in contact with the same metal, believed to be due to charging and dipoles at the interface.[10,12] Here, however, $\varphi_{bn\text{-}Ru/HfO2}$ is slightly larger than $\varphi_{bn\text{-}Ru/Al2O3}$. To understand this, it is necessary to consider how each dielectric will interact with Ru and the interface that will result from their interaction. In the case of the Al_2O_3/Ru interface, due to the high oxygen affinity of Al as compared to Ru, the Ru will experience minimal oxidation. For the HfO_2/Ru interface, however, the comparatively lower oxygen affinity of HfO_2 will result in a greater degree of oxidation of Ru. RuO_2 has a larger work function than Ru, at 5.2 vs. 4.7 eV, respectively.[6,13] Enhanced RuO_2 formation at the HfO_2/Ru interface could thus lead to a larger work function than at the Al_2O_3/Ru device. This is in agreement with other work based on MOS capacitors with an array of dielectric thicknesses which also showed that MOCVD Ru had a larger $\Phi_{M,eff}$ with HfO_2 than with Al_2O_3.[7]

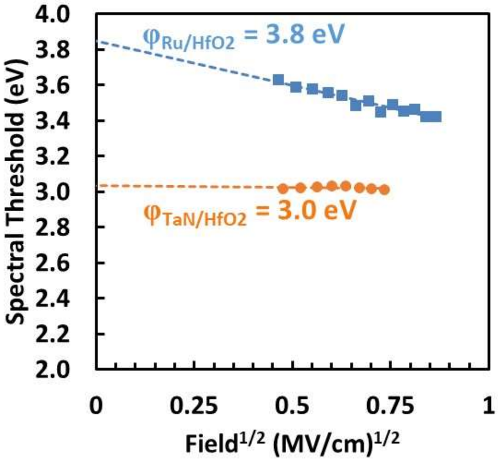

Figure 4.4: Schottky plot for the as-deposited HfO_2 MIM device with a TaN bottom electrode and Ru top electrode.

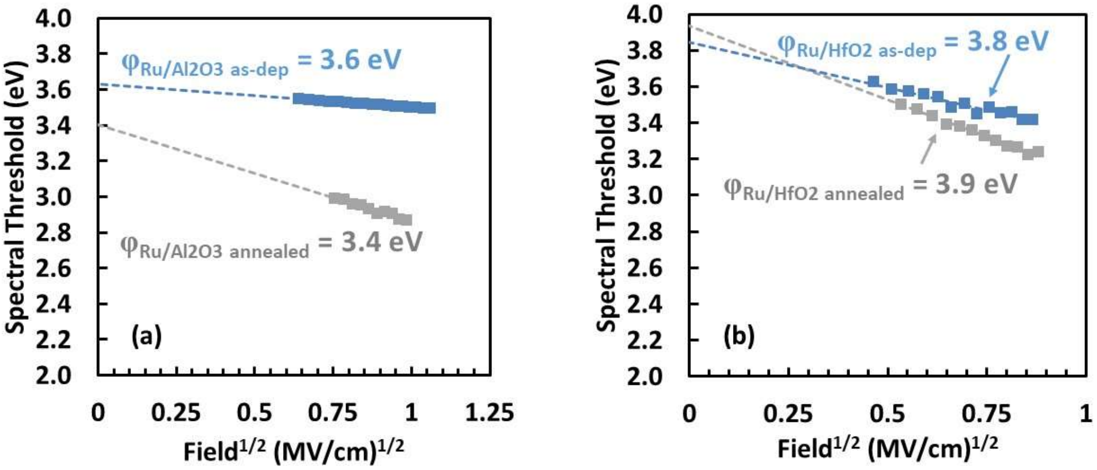

Figure 4.5: Schottky plots for annealed vs. as-deposited MIM devices with a Ru top electrode and TaN bottom electrode for (a) Al_2O_3 device and (b) HfO_2 device.

Post-metallization anneals (PMA) in forming gas were performed on select Al_2O_3 and HfO_2 devices, as shown in Fig. 5, to assess the impact on the Ru barrier height. For Al_2O_3, the IPE measured $\varphi_{bn\text{-}Ru/Al2O3}$ decreased by 0.2 eV after PMA to 3.4 eV. Previous work with sputtered Ru electrodes on MOS devices showed that PMA in a forming gas as compared to an oxygen environment led to a dipole at the Ru-insulator interface that resulted in a decrease of the Ru barrier height with both HfO_2 and SiO_2.[14,15] In that work, it was postulated that the reduction of the barrier height following a forming gas anneal was due to either a reduction of RuO_x to Ru or hydroxyl formation at the interface. However, $\varphi_{bn\text{-}Ru/HfO2}$ did not change for following PMA, remaining within experimental error of +/- 0.1 eV, at 3.9 eV. It is unclear at this time why HfO_2 would not exhibit the same barrier height decrease that is seen for Al_2O_3. One possibility is that the forming gas anneal was not sufficient to reduce the RuO_2 interfacial layer entirely on the HfO_2 sample due to non-ideal annealing conditions.

While the barrier heights showed minimal to no change, there was a distinct change in the slope of the Schottky plots for both oxides, most drastically for the Al_2O_3/Ru interface. Ideally, the slope of the Schottky plot should be proportional to the dielectric constant of the insulator in question, assuming a single metal work function. However, it has been show by Afanas'ev, et al. that the slope of the Schottky plot may also be affected by lateral non-uniformity of the metal work function, particularly in the case of Ru.[15] In this work, a similar slope is seen between the Ru and TaN bottom electrodes in the as-deposited samples. However, the slope of the Schottky plots for both Ru barriers changes upon anneal in a forming gas environment, suggesting that the anneal led to an increased degree of lateral non-uniformity in the top Ru electrode work function.

4.4 Summary and Conclusion

Barrier heights at the interface between ALD Ru and multiple ALD insulators were characterized with internal photoemission spectroscopy. It was found that the as-deposited barrier height at the Ru/Al_2O_3 interface was 3.6 eV, reducing to 3.4 eV following a forming gas anneal. The decrease in barrier height following anneal may be due to reduction of an interfacial RuO_2 that forms in contact with Al_2O_3. The Ru/HfO_2 barrier height was found to be 3.8 eV for both as-deposited and post forming gas anneal. The larger Ru barrier height for HfO_2 as compared to Al_2O_3 is in agreement with $\Phi_{M,eff}$ measurements in the literature and is likely due to a greater degree of oxidation of the Ru electrode in the case of HfO_2, leading to a larger work function RuO_2 interfacial layer at the Ru/HfO_2 interface. Following a 400 C forming gas anneal, the difference between the Ru/HfO_2 and Ru/Al_2O_3 barrier heights was within measurement error. Forming gas anneal leads to a drastic change in the slope of the Schottky plot for both insulators. This suggests that there is enhanced lateral non-uniformity of the $\Phi_{M,eff}$ of the top electrode following a forming gas anneal, in agreement with work on sputtered Ru.

4.5 Acknowledgments

The authors thank C. Tasker for equipment support and the Oregon Nanoscience and Microtechnologies Institute (ONAMI) for partial financial support. J.F.C. and M.A.J. acknowledge support of the NSF Center for Sustainable Materials Chemistry (grant CHE-1606982), M.H. acknowledges partial support from EMD Performance Materials. This work was conducted at the Materials Synthesis and Characterization (MaSC) Center, a National Nanotechnology Coordinated Infrastructure (NNCI) Northwest

Nanotechnology Infrastructure (NNI) user facility at the Oregon State University which is supported in part by the National Science Foundation (grant ECC-1542101) and Oregon State University.

4.6 References

[1] D.Z. Austin, M.A. Jenkins, D. Allman, S. Hose, D. Price, C.L. Dezelah, and J.F. Conley, Jr., “Atomic Layer Deposition of Ruthenium and Ruthenium Oxide Using a Zero-Oxidation State Precursor,” Chem. Mater. **29**, 1107 (2017).

[2] V.V. Afanas’ev and A. Stesmans, “Internal Photoemission at Interfaces of High-κ Insulators with Semiconductors and Metals,” J. Appl. Phys. **102**, 081301 (2007).

[3] N.V. Nguyen, O. Kirillov, H.D. Xiong, and J.S. Suehle, “Internal Photoemission Spectroscopy of Metal Gate/High-k/Semiconductor Interfaces,” in *AIP Conf. Proc.* (AIP Publishing, 2007), pp. 308–314.

[4] R.J. Powell, “Interface Barrier Energy Determination from Voltage Dependence of Photoinjected Currents,” J. Appl. Phys. **41**, 2424 (1970).

[5] S. Swaminathan, Y. Sun, P. Pianetta, and P.C. McIntyre, “Ultrathin ALD-Al2O3 Layers for Ge(001) Gate Stacks: Local Composition Evolution and Dielectric Properties,” J. Appl. Phys. **110**, 094105 (2011).

[6] K. Fröhlich, K. Husekova, D. Machajdik, J.C. Hooker, N. Perez, M. Fanciulli, S. Ferrari, C. Wiemer, A. Dimoulas, G. Vellianitis, and F. Roozeboom, “Ru and RuO2 Gate Electrodes for Advanced CMOS Technology,” Mater. Sci. Eng. B **109**, 117 (2004).

[7] M. Hayes, J. Woodruff, C. Dezelah, and J.F. Conley, Jr., “Properties of Annealed Ruthenium Deposited via Atomic Layer Deposition Using Ru(DMBD)CO3,” Manuscr. Prog. (n.d.).

[8] V.V. Afanas’ev, M. Houssa, A. Stesmans, and M.M. Heyns, “Electron Energy Barriers between (100)Si and Ultrathin Stacks of SiO2,Al2O3, and ZrO2 Insulators,” Appl. Phys. Lett. **78**, 3073 (2001).

[9] V.V. Afanas’ev, M. Houssa, A. Stesmans, and M.M. Heyns, “Band Alignments in Metal–Oxide–Silicon Structures with Atomic-Layer Deposited Al2O3 and ZrO2,” J. Appl. Phys. **91**, 3079 (2002).

[10] V.K. Adamchuk and V.V. Afanas’ev, “Internal Photoemission Spectroscopy of Semiconductor-Insulator Interfaces,” Prog. Surf. Sci. **41**, 111 (1992).

[11] M.A. Jenkins, J.M. McGlone, J.F. Wager, and J.F. Conley, “Internal Photoemission Spectroscopy Determination of Barrier Heights between Ta-Based Amorphous Metals and Atomic Layer Deposited Insulators,” J. Appl. Phys. **125**, 055301 (2019).

[12] S. Monaghan, P.K. Hurley, K. Cherkaoui, M.A. Negara, and A. Schenk, “Determination of Electron Effective Mass and Electron Affinity in HfO2 Using MOS and MOSFET Structures,” Solid-State Electron. **53**, 438 (2009).

[13] M.A. Jenkins, T. Klarr, D.Z. Austin, W. Li, N.V. Nguyen, and J.F. Conley, Jr., “Assessment of Energy Barriers Between ZrCuAlNi Amorphous Metal and Atomic Layer Deposition Insulators Using Internal Photoemission Spectroscopy,” Phys. Status Solidi RRL – Rapid Res. Lett. **12**, 1700437 (2018).

[14] K. Frohlich, K. Husekova, D. Machajdik, R. Luptak, M. Tapajna, and J.C. Hooker, "Growth and Properties of Ruthenium Based Metal Gates for PMOS Devices," in *Fifth Int. Conf. Adv. Semicond. Devices Microsyst. 2004 ASDAM 2004* (2004), pp. 163–166.

[15] L. Pantisano, T. Schram, Z. Li, J.G. Lisoni, G. Pourtois, S. De Gendt, D.P. Brunco, A. Akheyar, V.V. Afanas'ev, S. Shamuilia, and A. Stesmans, "Ruthenium Gate Electrodes on SiO2 and HfO2: Sensitivity to Hydrogen and Oxygen Ambients," Appl. Phys. Lett. **88**, 243514 (2006).

[16] V. Afanas'ev, N. Kolomiiets, M. Houssa, and A. Stesmans, "Internal Photoemission Metrology of Inhomogeneous Interface Barriers," Phys. Status Solidi A 1700865 (2017).

5 CHARACTERIZATION OF FERROELECTRIC HAFNIUM ZIRCONIUM OXIDE ENERGY BARRIER HEIGHTS WITH INTERNAL PHOTOEMISSION SPECTROSCOPY

M.A. Jenkins, S. W. Smith, and J.F. Conley, Jr.

Manuscript in preparation

5.1 Introduction

Ferroelectric materials based on HfO_2 have been highly researched in recent years for multiple applications. One application with a large degree of recent interest is use of ferroelectric materials in negative capacitance FETs to achieve sub-threshold swings steeper than the theoretical limit of 60 mV/decade for conventional FETs.[1] Ferroelectric materials, including HfO_2, have been demonstrated to exhibit negative differential capacitance, and have exhibited subthreshold slopes less than 60 mV/decade in a FinFET structure.[2,3] HfO_2-based ferroelectric materials are of particular interest due to the ease of integration with existing silicon CMOS processing. It is believed that the orthorhombic phase of HfO_2 is responsible for ferroelectric behavior. This phase has been stabilized with a number of dopants, one of which is zirconium,[4–6] where the relative ratio of Zr to Hf may be used to control the ratio of phases present, and thus the ferroelectric behavior.[7]

Successful integration of ferroelectric materials into ferroelectric memory or ferroelectric FETs necessitates an understanding of the band structure of these materials and how they interact with electrodes. This is particularly important because the high dielectric constant of $Hf_{1-x}Zr_xO_2$ materials[7] may lead to enhanced Fermi-level pinning.[8] This would cause an insensitivity of the metal-ferroelectric barrier height to the metal work function, meaning that there would less control over the threshold voltage of these transistors. Thus, it is beneficial for integration efforts to characterize the barrier height between the metal and ferroelectric material. Internal photoemission spectroscopy (IPE) is a technique capable of characterizing insitu barrier heights.[9–11] This is necessary because, as previously mentioned, the insitu barrier height may deviate from ideal due to non-idealities such as Fermi-level pinning. In this work, IPE is used to measure the insitu energy barrier heights at the interface of $Hf_{1-x}Zr_xO_2$ and an array of metal electrodes.

5.2 Experimental

Sample preparation began with low doped Si substrates with a native oxide. On these substrates, 100 nm of TaN was deposited as the bottom electrode via pulsed DC sputtering from a TaN target. Atomic layer deposition was then used to deposit 20 nm $Hf_{0.58}Zr_{0.42}O_2$ at 150 °C using tetrakis(dimethylamino)hafnium (TDMAH) held at 75 °C and tetrakis(dimethylamino)zirconium (TDMAZ) held at 75 °C, with H_2O as the oxidizing agent for both precursors. $Hf_{0.58}Zr_{0.42}O_2$ was deposited using 102 supercycles, with each supercycle consisting of 1 ZrO_2 cycle and 1 HfO_2 cycle.[7] Following insulator deposition, a rapid thermal anneal was performed at 600 °C for 30 seconds in an N_2 environment. Top electrodes of Au, Al, Ta, Pt, and Pt/Ti (with Ti in contact with the insulator) were patterned via liftoff with devices consisting of circles 75-200 μm in diameter. Top electrodes were deposited via physical vapor deposition with a targeted thickness of 10 nm for all metals except for Pt/Ti, which had a targeted Pt thickness of 10 nm a Ti thickness of 1.5 nm.

IPE measurements were conducted in a homebuilt system with estimated accuracy of +/- 0.1 eV. Light originated from a 150 W Xe arc lamp, which passed through a monochromator that selected a single wavelength to reach the sample, which was placed in a standard probe station. Voltage was applied to the bottom electrode of the sample and the top electrode was grounded. An array of voltages were applied such that, assuming no built-in field, application of a positive voltage to the bottom electrode would result in emission from the top electrode and application of negative voltage to the bottom electrode would result in emission from the bottom electrode. At each applied voltage, the monochromator swept the photon energy from 2 to 5 eV and the current was measured. The spectral threshold was determined following conversion of current to quantum yield, taking the yield to the ½ to account for the energy distribution of carriers at the metal electrode, and then extracting the onset of photoemission from the most linear region of the yield$^{1/2}$ vs. photon energy curve. The zero-field barrier height was then determined from a Schottky plot of the spectral threshold vs. applied field$^{1/2}$ to account for Schottky barrier lowering. [12]

5.3 Results and Discussion

Fig. 5.1 shows the Schottky plot derived from IPE measurements, with the resulting zero-field barrier heights shown in Table 5.1. All metals except for TaN are top electrodes, while the TaN data is taken from the bottom electrode of the Ta device. The TaN results from the Ta device were repeated with the Al device. Because TaN is a bottom electrode, there may be unique considerations in interpreting the results as it will have undergone additional processing in the insulator deposition and anneal that the top electrodes did not experience. The $Hf_{0.58}Zr_{0.42}O_2$/TaN barrier height of 2.7 eV is 0.2 eV lower than prior IPE measurements of HfO_2/TaN, with a barrier height of 2.9 eV.[13] Au and Al also show slightly lower barrier heights with $Hf_{0.58}Zr_{0.42}O_2$ as compared to HfO_2, with a difference of 0.2 eV between $Hf_{0.58}Zr_{0.42}O_2$ and HfO_2 barrier heights for both metals.[11,13] This 0.2 eV difference between $Hf_{0.58}Zr_{0.42}O_2$ and HfO_2 barrier heights is consistent for all three metals for which there are direct comparison with our previous work. This points towards a slightly lower band gap for $Hf_{0.58}Zr_{0.42}O_2$ as compared to HfO_2.

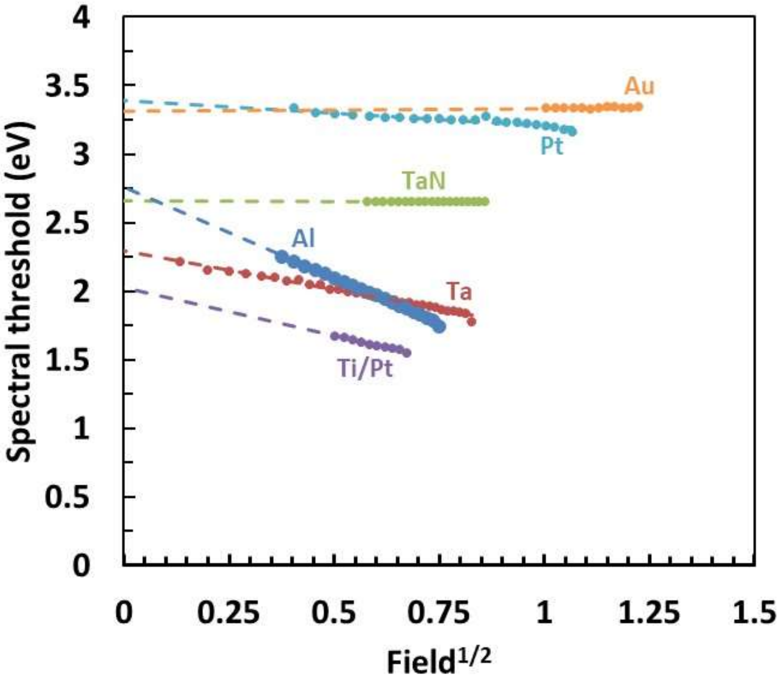

Figure 5.1: Schottky plot of the results in this work for all metals. TaN Schottky plot is from the device with a Ta top electrode. Dashed lines are a linear regression of the data for each metal, with the y-intercept giving the zero-field barrier height.

Similar to work with HfO_2, the Al/$Hf_{0.58}Zr_{0.42}O_2$ Schottky plot shows a steeper slope than any of the other metals.[11] The slope of the Schottky plot should ideally be dependent on the dielectric constant of the insulator, however this is often not the case due to non-idealities at the interface. In this case, this could be due to negative charge trapped at the interface, or lateral non-uniformity of the effective work function at the interface.[14] Other metals, particularly the inert metals Au and Pt, show minimal change in the spectral threshold with field, as would be expected from a high dielectric constant material such as $Hf_{0.58}Zr_{0.42}O_2$.

Table 5.1: Barrier heights measured in this work, allow with metal work functions from literature and the resulting calculated electron affinity

op electrode	Barrier height (eV)	Work function (eV)	Calculated electron affinity (eV)
Pt	3.4	5.6	2.2
Au	3.3	5.4	2.1
TiPt	2.0	4.33	2.33
TaN	2.7	4.3	1.6
Ta	2.3	4.25	1.95
Al	2.8	4.2	1.4

Table 5.1 also shows reported work functions for the metals used in this work, along with the electron affinity that would be calculated from the barrier height measured in this work and the literature work function. There is a large range in these calculated values where this value should ideally be consistent across all metals. However, as previously mentioned, this ideal relationship is rarely the case. Fermi-level pinning accounts for some of this non-ideality. Pinning results in the same linear relationship between barrier height and work function, but with a slope less than one, where the slope is then defined as the slope parameter. The slope parameter may be found as the slope from a plot of work function vs. barrier height. This is shown in Fig. 5.2, yielding a slope parameter for $Hf_{0.58}Zr_{0.42}O_2$ of 0.71. There is still a large degree of variation in the lower work function metals, so clearly Fermi-level pinning is not the only cause of non-ideality in the relationship between barrier height and work function in this material. In the non-inert metals, there may be interfacial layers present. For any of these metals, there may be

additional sources of dipoles causing these non-idealities. It is also important to note that this degree of variation is also seen in literature for HfO_2 and ZrO_2.[9]

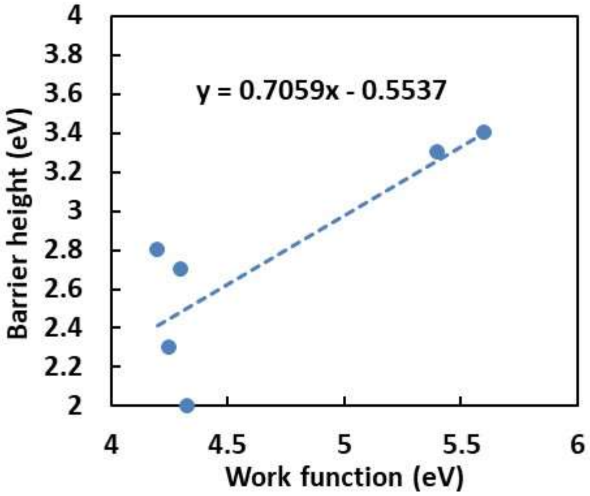

Figure 5.2: Plot of work function vs. barrier height as determined via IPE and used for determining the slope parameter.

By taking the photon energy sweep out to a 6 eV, rather than 5 eV, photoconduction in the HfO_2 can be detected as a secondary slope in the yield$^{1/2}$ curve. This is shown in a curve of emission from the Pt top electrode in Fig. 5.3. This can be used to determine the band gap of the insulator.[15] In Fig. 5.3, the band gap is determined by the intersection of a linear regression of the baseline and the region of photoconduction. This leads to a band gap of 4.9 eV for the $Hf_{0.58}Zr_{0.42}O_2$ used in this work. This is a smaller than both HfO_2 and ZrO_2, which is consistent with the observation of the smaller barrier heights for $Hf_{0.58}Zr_{0.42}O_2$ as compared to HfO_2.

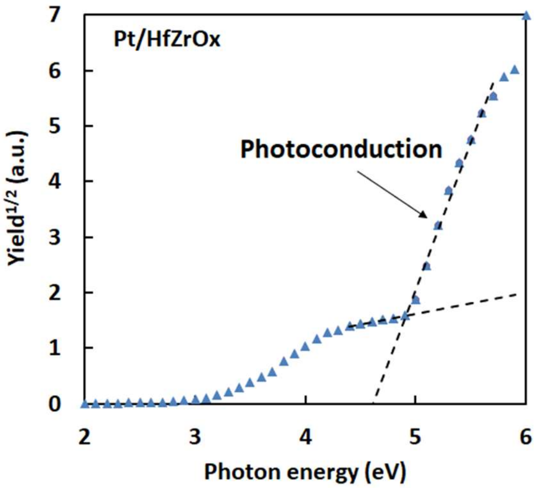

Figure 5.3: Representative curve of yield$^{1/2}$ vs. photon energy, taken out to 6 eV to obtain photoconductivity data for the insulator. Region of photoconduction is as indicated, and onset of photoconduction is taken to be the intersection of the two dashed lines.

5.4 Summary and Conclusion

Barrier heights between various metal electrodes and $Hf_{0.58}Zr_{0.42}O_2$ were measured via internal photoemission spectroscopy. It was found that for electrodes for which there are comparisons to HfO_2, the difference between the barrier heights of $Hf_{0.58}Zr_{0.42}O_2$ and HfO_2 was consistently 0.2 eV, with $Hf_{0.58}Zr_{0.42}O_2$ being 0.2 eV lower than HfO_2. This indicates that the band gap for $Hf_{0.58}Zr_{0.42}O_2$ is slightly smaller than that of HfO_2. A steep slope in the Schottky plot of the Al/$Hf_{0.58}Zr_{0.42}O_2$ device was also seen in prior work for Al/HfO_2 and is believed to be due to negative charge at the interface or lateral non-uniformity of the work function. The other metals showed much shallower slopes, with the inert metals showing little dependence of the spectral threshold on the applied bias. This is consistent with expectations for a high dielectric constant material. A band gap of 4.9 eV was found by extending the measurement spectrum out to 6 eV.

5.5 Acknowledgments

The authors thank C. Tasker for equipment support and the Oregon Nanoscience and Microtechnologies Institute (ONAMI) for partial financial support. J.F.C. and M.A.J. acknowledge support of the NSF Center for Sustainable Materials Chemistry (grant CHE-1606982). This work was conducted at the Materials Synthesis and Characterization (MaSC) Center, a National Nanotechnology Coordinated Infrastructure (NNCI) Northwest Nanotechnology Infrastructure (NNI) user facility at the Oregon State University which is supported in part by the National Science Foundation (grant ECC-1542101) and Oregon State University.

5.6 References

[1] S. Salahuddin and S. Datta, “Use of Negative Capacitance to Provide Voltage Amplification for Low Power Nanoscale Devices,” Nano Lett. **8**, 405 (2008).

[2] M. Hoffmann, M. Pešić, K. Chatterjee, A.I. Khan, S. Salahuddin, S. Slesazeck, U. Schroeder, and T. Mikolajick, “Direct Observation of Negative Capacitance in Polycrystalline Ferroelectric HfO2,” Adv. Funct. Mater. **26**, 8643 (2016).

[3] K. Li, P. Chen, T. Lai, C. Lin, C. Cheng, C. Chen, Y. Wei, Y. Hou, M. Liao, M. Lee, M. Chen, J. Sheih, W. Yeh, F. Yang, S. Salahuddin, and C. Hu, “Sub-60mV-Swing Negative-Capacitance FinFET without Hysteresis,” in *2015 IEEE Int. Electron Devices Meet. IEDM* (2015), pp. 22.6.1-22.6.4.

[4] S. Starschich, T. Schenk, U. Schroeder, and U. Boettger, “Ferroelectric and Piezoelectric Properties of Hf1-XZrxO2 and Pure ZrO2 Films,” Appl. Phys. Lett. **110**, 182905 (2017).

[5] J. Müller, T.S. Böscke, U. Schröder, S. Mueller, D. Bräuhaus, U. Böttger, L. Frey, and T. Mikolajick, “Ferroelectricity in Simple Binary ZrO2 and HfO2,” Nano Lett. **12**, 4318 (2012).

[6] S. Riedel, P. Polakowski, and J. Müller, “A Thermally Robust and Thickness Independent Ferroelectric Phase in Laminated Hafnium Zirconium Oxide,” AIP Adv. **6**, 095123 (2016).

[7] S.W. Smith, A.R. Kitahara, M.A. Rodriguez, M.D. Henry, M.T. Brumbach, and J.F. Ihlefeld, “Pyroelectric Response in Crystalline Hafnium Zirconium Oxide (Hf1-XZrxO2) Thin Films,” Appl. Phys. Lett. **110**, 072901 (2017).

[8] J. Robertson, “Band Offsets of Wide-Band-Gap Oxides and Implications for Future Electronic Devices,” J. Vac. Sci. Technol. B **18**, 1785 (2000).

[9] V.V. Afanas’ev and A. Stesmans, “Internal Photoemission at Interfaces of High-κ Insulators with Semiconductors and Metals,” J. Appl. Phys. **102**, 081301 (2007).

[10] N.V. Nguyen, O.A. Kirillov, and J.S. Suehle, “Band Alignment of Metal-Oxide-Semiconductor Structure by Internal Photoemission Spectroscopy and Spectroscopic Ellipsometry,” Thin Solid Films **519**, 2811 (2011).

[11] M.A. Jenkins, T. Klarr, D.Z. Austin, W. Li, N.V. Nguyen, and J.F. Conley, Jr., “Assessment of Energy Barriers Between ZrCuAlNi Amorphous Metal and Atomic Layer Deposition Insulators Using Internal Photoemission Spectroscopy,” Phys. Status Solidi RRL – Rapid Res. Lett. **12**, 1700437 (2018).

[12] N.V. Nguyen, O.A. Kirillov, W. Jiang, J.E. Maslar, W. Kimes, and J.S. Suehle, "Interface Barrier Determination by Internal Photoemission: Applications to Metal/Oxide/Semiconductor Structure," ECS Trans. **13**, 161 (2008).

[13] M.A. Jenkins, J.M. McGlone, J.F. Wager, and J.F. Conley, Jr., "Internal Photoemission Spectroscopy Determination of Barrier Heights between Ta-Based Amorphous Metals and Atomic Layer Deposited Insulators," J. Appl. Phys. **125**, 055301 (2019).

[14] V.V. Afanas'ev, N. Kolomiiets, M. Houssa, and A. Stesmans, "Internal Photoemission Metrology of Inhomogeneous Interface Barriers," Phys. Status Solidi A **215**, n/a (2017).

[15] V.V. Afanas'ev, A. Stesmans, F. Chen, X. Shi, and S.A. Campbell, "Internal Photoemission of Electrons and Holes from (100)Si into HfO2," Applied Physics Letters **81**, 1053 (2002).

6 LAMINATE AL_2O_3/TA_2O_5 METAL/INSULATOR/INSULATOR/METAL (MIIM) DEVICES FOR HIGH VOLTAGE APPLICATIONS

M. A. Jenkins, D. Z. Austin, K. E. K. Holden, D. Allman, and J. F. Conley, Jr.

IEEE Transactions on Electron Devices **66**, 5260 (2019)

6.1 Introduction

Back end of line (BEOL) metal-insulator-metal (MIM) devices such as capacitors and resistive random-access memory (RRAM) help to increase integrated circuit packing density by multilevel stacking of devices. Recently, thin film MIM tunnel diodes have gained widespread interest for a number of applications such as rectification for solar rectenna based energy harvesting [1–4], infrared (IR) detection, selector diodes for RRAM [5], hot electron transistors [6,7], single electron transistors [8], and field emission cathodes [9–11]. Typically, the current vs. voltage performance of single insulator MIM devices is controlled by the built-in electric field induced by the work function difference ($\Delta\Phi_M$) between the two dissimilar metal electrodes, which is limited to a maximum of roughly 1.3 eV for practical materials [12,13]. Recent work, however, has demonstrated that engineering the asymmetry of the tunnel barrier by using asymmetric bi-layer and multi-layer nanolaminate heterostructure insulators with different electron affinities is a more effective way to optimize these devices. Further, by properly aligning the asymmetric tunnel barrier with $\Delta\Phi_M$, one can greatly improve the asymmetry ($|I^-/I^+|$,), non-linearity ($f_{NL} = (dI/dV)/(I/V)$), responsivity ($1/2(d^2I/dV^2)/(dI/dV)$), and zero-bias-resistance of these devices ($I/V|_{V=0\,V}$) [7,14–24]. Work on dual insulator MIIM devices to date has focused on thin films insulator stacks for low voltage applications. For example, it was recently shown that the use of 5 nm thick Ta_2O_5/Al_2O_3 bilayers with TaN bottom and Al top electrodes, resulted in $\eta_{asym} > 10$ and f_{NL} of ~5 at less than 0.5 V, a significant improvement over Ta_2O_5 or Al_2O_3 alone [14]. There is also interest in using MIIM based devices for high voltage applications such as diodes for circuit routing optimization, energy management for flexible wearable electronics, high voltage logic, antenna diodes for plasma induced damage (PID) and electrostatic discharge protection, and antifuse one-time programmable (OTP) non-volatile memory [25–27]. Based on oxide breakdown, antifuse OTP memory is a class of programmable read only memory (PROM) that can be programmed only once. Because of its low leakage in the non-programmed state, small readout voltage, and imperviousness to altering the state of the device with heat or voltage, they are in demand not only for analog/sensor trimming and calibration, but also for high security applications such as secure key storage and device IDs [28].

In this work, we evaluate a series of thick (60-300 nm) Al_2O_3/Ta_2O_5 bi-layer MIIM devices for high-voltage applications and investigate the impact of Ta_2O_5 to Al_2O_3 stack order and layer thickness ratio on device performance, including asymmetry, reverse leakage, breakdown, and programmable resistance ratio. Regions of operation are distinguished, underlying dominant conduction mechanisms are identified, and performance evaluated for OTP applications.

6.2 Experimental

Dual insulator Al_2O_3/Ta_2O_5 MIIM diodes were fabricated using three different substrates as bottom electrodes. The majority of the work was performed using $Si/SiO_2/Ta/TaN$ substrates with the TaN layer planarized via chemical mechanical polishing (provided by ON Semiconductor). For comparison, Si/SiO_2 substrates with either sputtered ZrCuAlNi or sputtered TiN were also investigated. Atomic layer deposition (ALD) of Al_2O_3 and Ta_2O_5 were performed at 200 °C in a Picosun SUNALE R-150 reactor using alternating N_2-purge-separated pulses of H_2O and either trimethylaluminum (TMA) or tris(ethylmethylamido)(tert-butylimido)tantalum(V)

(TBTEMTa), respectively. The TMA and TBTEMTa sources were held at 17 °C and 90 °C, respectively. The deposition rates of Al_2O_3 and Ta_2O_5 were approximately 0.092 nm/cycle and 0.051 nm/cycle, respectively. Al_2O_3/Ta_2O_5 bilayer stacks were deposited without breaking vacuum. To complete fabrication of MIIM diodes, 250 µm diameter Al top contacts (area approximately 0.05 mm^2) were thermally evaporated through a shadow mask. A schematic cross section of a $TaN/Al_2O_3/Ta_2O_5/Al$ MIIM diode is shown in Fig. 6.1(a).

Insulator film thickness was measured using a J.A. Woollam M2000 variable angle spectroscopic ellipsometer (VASE) in the range of 400-1000 nm. Current vs. voltage measurements were taken using an Agilent B1500A in the dark with the bottom electrode held at ground. Measurements shown were performed on pristine devices with the bias swept from 0 V to the maximum absolute voltage, with new devices used for each polarity. The area of each Al contact was measured (with an average error of +/- 1.8%) for area normalizations.

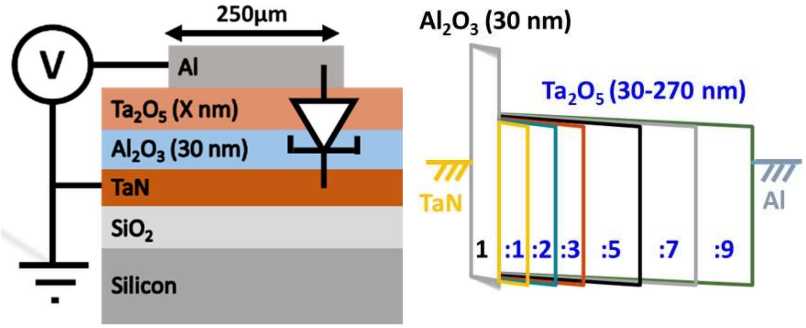

Figure 6.1: (a) Schematic cross section and (b) superimposed equilibrium band diagrams for $Al/Ta_2O_5/Al_2O_3/TaN$ MIIM devices.

6.3 Results and Discussion

6.3.1 Deposition Temperature, Layer Order, and Lower Electrode

To obtain the maximum asymmetry of MIIM diodes with 30 nm / 30 nm (1:1 ratio) Al_2O_3/Ta_2O_5 insulator stacks, three parameters are varied: (i) the ALD temperature (200 vs. 250 °C), (ii) the bottom electrode (TaN, TiN, and ZrCuAlNi), and (iii) the order of insulator deposition (Al_2O_3/Ta_2O_5 vs. Ta_2O_5/Al_2O_3). For all devices, an ALD temperature of 200 °C produces a greater maximum asymmetry than a temperature of 250 °C. Shown in Fig. 6.2 are η_{asym} vs. V plots for all of the 200 °C deposited devices. Of the three bottom electrode metals, TaN has the greatest asymmetry for all ALD temperatures and insulator orientations, indicating that TaN has a larger effective work function with both Al_2O_3 and Ta_2O_5 than does either TiN or ZrCuAlNi. Finally, an insulator orientation of $Al/Al_2O_3/Ta_2O_5$ shows the greatest asymmetry in all cases except for devices with a TaN bottom electrode. This same orientation with respect to the electrode work functions also led to the largest asymmetry in our previous report on ultrathin Al_2O_3/Ta_2O_5 stacks [18]. Subsequent experiments were thus performed on TaN substrates with an insulator orientation of Al_2O_3/Ta_2O_5 and an ALD temperature of 200 °C.

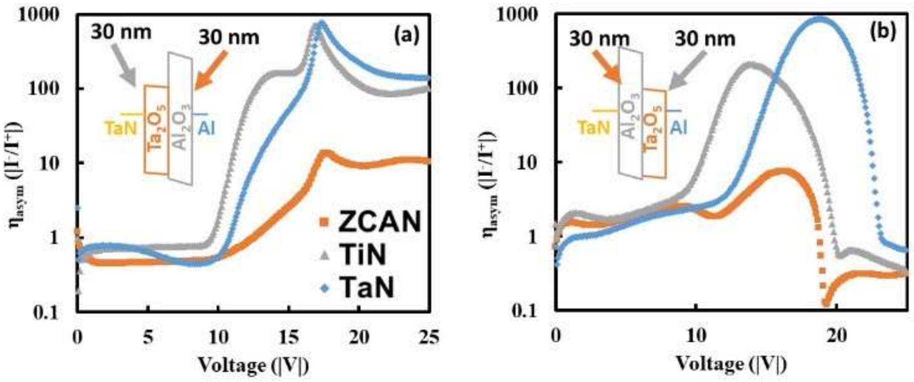

Figure 6.2: Plots of log (η_{asym}) vs. V for (a) Ta_2O_5/Al_2O_3 and (b) Al_2O_3/Ta_2O_5 MIIM diodes, each with Al top electrodes and either TaN, TiN, or ZrCuAlNi bottom electrodes.

6.3.2 Conduction mechanism analysis

Superimposed equilibrium band diagrams for a series of Al_2O_3/Ta_2O_5 MIIM devices with the Al_2O_3 layer fixed at 30 nm and the Ta_2O_5 layer thickness varied from 30 to 270 nm, such that the $Al_2O_3:Ta_2O_5$ thickness ratio is varied from 1:1 to 1:9, is shown in Fig. 6.1(b). Plots of logarithmic current density vs. applied voltage (J-V) for these devices (Fig. 6.3) reveal that the $Al_2O_3:Ta_2O_5$ thickness ratio affects the J-V characteristics in a number of distinct ways for positive and negative bias.

(i) Positive bias

Under positive bias, four distinct regions of J-V behavior are apparent (marked 1-4 in Fig. 6.3). In each of these regions, the dominant conduction mechanisms are determined using a combination of J-V simulation, linearization of test data and elevated temperature testing (where appropriate).

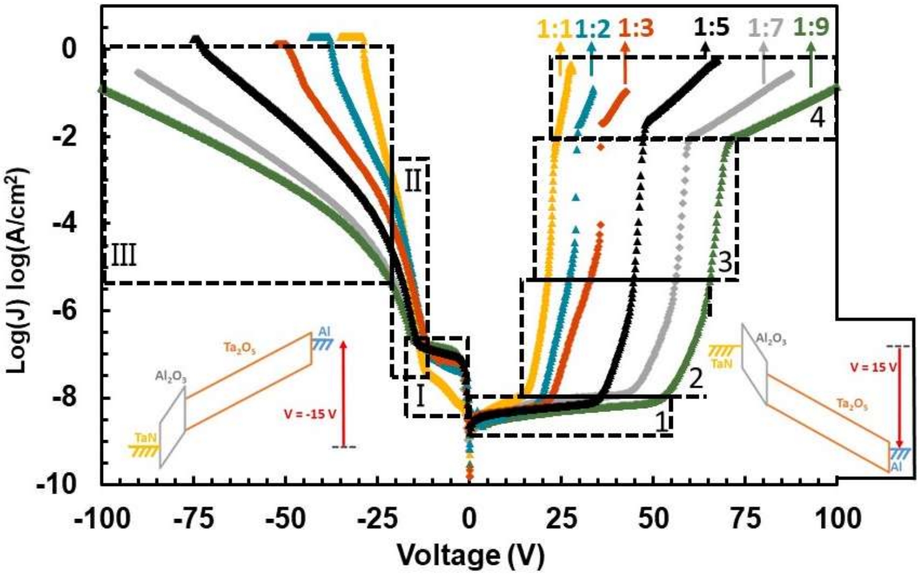

Figure 6.3: Representative log J vs. V curves for a series of TaN/Al_2O_3/Ta_2O_5/Al MIIM devices with constant Al_2O_3 thickness (30 nm) and varying Ta_2O_5 thickness, with Al_2O_3:Ta_2O_5 thickness ratios labeled. Three distinct conduction regions are indicated for negative bias (labeled I, II, III and demarcated with dashed lines) and four conduction regions are indicated for positive bias (labeled 1 through 4 and demarcated with dashed lines). Insets show a representative negative and positive bias band diagrams for the 1:5 device.

Region 1 is defined as the region prior to the "knee" in each J-V curve that marks the onset of steeply increasing conduction. As an example, for the 1:5 device, Region 1 begins at 0 V and ends at approximately 37 V. Within this region, J is linearly dependent upon V, suggesting ohmic conduction where

$$J_{ohmic} = nq\mu\mathcal{E}\,, \tag{1}$$

and where n is the density of electrons in the conduction band (CB) of the insulator, q is the elementary charge, μ is the electron mobility within the insulator, and $\mathcal{E}$ is the electric field. Fitting Eqn. (1) to the linearized J-V data yields a mobility μ of roughly 20 $cm^2/(V\ s)$ and an n of roughly 3×10^3 cm^{-3}, both reasonable values for Al_2O_3, indicating that ohmic conduction through the Al_2O_3 is the dominant charge transport mechanism in Region 1.

Region 2 is defined between the "knee" (again, occurring at roughly 37 V for the 1:5 device) and the more subtle increase in slope (occurring at approximately 44 V for the 1:5 device). This region is well described by Fowler-Nordheim tunneling (FNT), an electrode / interface controlled conduction mechanism in which electrons quantum mechanically tunnel through the triangular barrier formed when a high electric field is applied across the insulator tunnel barrier. FNT is distinct from direct tunneling, in which electrons must tunnel through the entirety of the insulator thickness, and may be described as

$$J_{FNT} = \frac{q^3\mathcal{E}^2}{16\pi^2\hbar\varphi_{Bn}}\exp\left[-\frac{4\sqrt{2m_e^*}\varphi_{Bn}^{3/2}}{3\hbar\mathcal{E}}\right], \tag{2}$$

where $\hbar$ is the reduced Plank's constant, φ_{Bn} is the barrier height between the two materials of interest (in this case the TaN/Al_2O_3 interface), and m_e^* is the electron effective mass in the insulator [29]. Linearizing this equation and replotting Region 2 of Fig. 6.3 as $\ln(J/\mathcal{E}^2)$ vs. $1/\mathcal{E}$ allows an assessment of the likelihood of FNT (through determination of the R^2 value of a linear fit). As seen in the inset in Fig. 6.4(a), the 1:5 stack device shows high linearity with an R^2 value of 0.996 in Region 2. Similarly good fits are observed for the rest of the devices, strongly suggesting that FNT through the Al_2O_3 layer is limiting charge transport in Region 2.

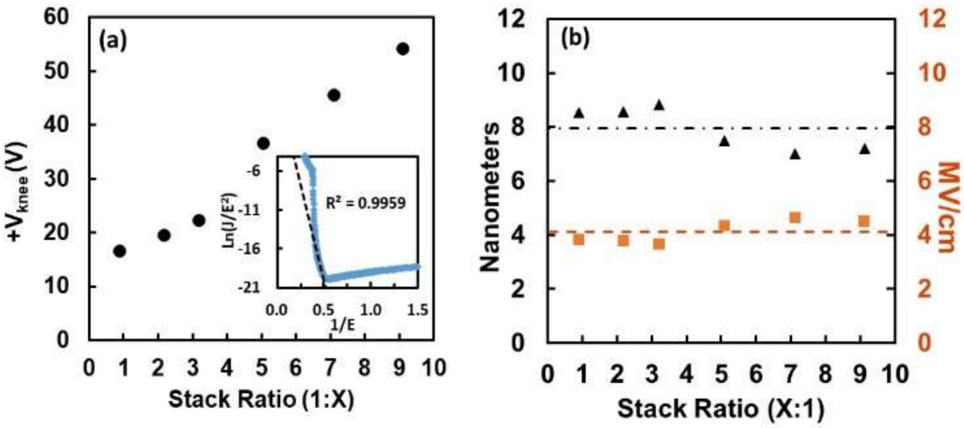

Figure 6.4: (a) Plot of positive V_{knee} vs. Al_2O_3:Ta_2O_5 thickness ratio (inset shows FNT linearization plot of ln($J/\mathscr{E}^2$) vs. $1/\mathscr{E}$ for the 1:5 Al_2O_3:Ta_2O_5 device under positive bias along with the linear regression coefficient of determination (R^2) for Region 2). (b) Plot of $\mathscr{E}_{Al2O3,knee}$ (right-hand axis, orange squares) and effective tunnel distance d_{tunnel} (left-hand axis, black triangles) in Al_2O_3 vs. Al_2O_3:Ta_2O_5 thickness ratio assuming an ideal capacitive voltage divider. The average value for each quantity is indicated with a horizontal dashed line.

The voltage at which the knee occurs (V_{knee}) increases roughly linearly with increasing stack ratio from roughly 16 V for the 1:1 to roughly 54 V for the 1:9 devices, as shown in Fig. 6.4(a), where the knee values are determined from the intersection of the slopes of the pre and post knee regions. Assuming that the devices behave as ideal capacitive voltage dividers under positive applied bias, the electric field present across the Al_2O_3 layer ($\mathscr{E}_{Al2O3,knee}$) and effective tunneling distance (d_{tunnel}) through the Al_2O_3 layer are calculated at V_{knee} and plotted for each device in Fig. 6.4(b). The average of the $\mathscr{E}_{Al2O3,knee}$ and d_{tunnel} across all thickness ratio devices is 4.0 MV/cm and 8.1 nm. Though there does appear to be a slight difference between the average values for the three low ratio stacks versus the three high ratio stacks, this may be an extraction artifact due to the increased contribution of FPE conduction in stacks with thinner Ta_2O_5 layers. Extrapolation of the three lowest ratio and three highest ratio stacks in Fig. 6.4(a) to the y-axis (zero Ta_2O_5 layer thickness) both yield $V_{knee} = 12$ V ($\mathscr{E}_{Al2O3,knee} = 4$ MV/cm), consistent with the average of the calculated values and with previous reports of values for FNT in Al_2O_3. Taken together, the FNT linearization, $\mathscr{E}_{Al2O3,knee}$ values, and d_{tunnel} values indicate that Region 2 is dominated by FNT through the Al_2O_3 layer.

Region 3 is bounded at lower voltages by the subtle increase in slope and at higher voltage by the abrupt decrease in slope. Following FNT conduction through the Al_2O_3 in Region 2, as voltage is increased, the field across the Al_2O_3 layer eventually reaches the breakdown strength and irreversible hard breakdown occurs. The voltage at the onset of breakdown (V_{BD}) for each device is plotted in Fig. 6.5. Assuming again an ideal Ta_2O_5/Al_2O_3 capacitive voltage divider, the electric field in the Al_2O_3 layer at which hard breakdown occurs ($\mathscr{E}_{BD,Al2O3}$) is calculated for each devices and plotted in Fig. 6.5 for all stack ratios. The calculated $\mathscr{E}_{BD,Al2O3}$ is roughly independent of stack ratio and the average $\mathscr{E}_{BD,Al2O3}$ for all device types is roughly 5.8 MV/cm. Extrapolating the $V_{BD,Al2O3}$ data to the y-axis (zero Ta_2O_5 thickness) yields ~18 V or ~6 MV/cm, consistent with average of the calculated values.

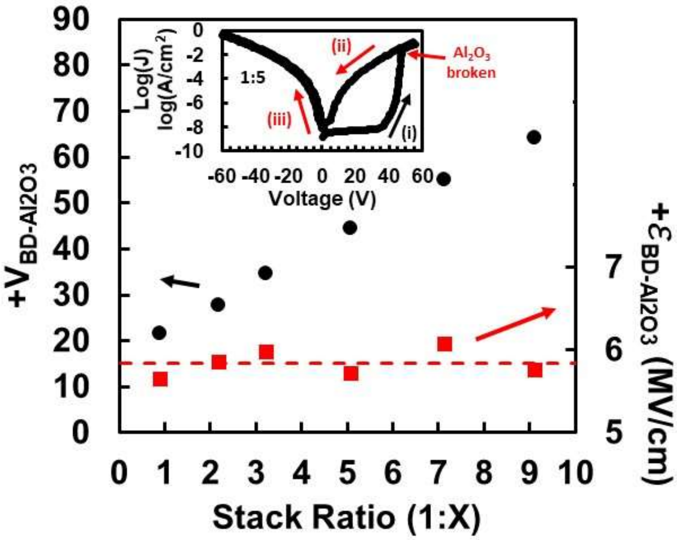

Figure 6.5: Plots of V$_{BD,Al2O3}$ and E$_{BD,Al2O3}$ for all devices under positive bias. The average of the E$_{BD,Al2O3}$ of all device types indicated by the horizontal dashed line. Inset shows J-V sweep following breakdown.

Finally, Region 4 of the positive bias response is marked by the abrupt decrease in slope following breakdown of the Al_2O_3 layer. Once breakdown occurs and the device enters Region 4, the J-V behavior is irreversibly changed, as shown in the inset of Fig. 6.5. Subsequent current-voltage behavior is limited by Frenkel-Poole emission (FPE) through only the Ta_2O_5 layer, described by

$$J_{FPE} = q\mu N_C \mathcal{E} \exp\left[\frac{-q\left(\varphi_T - \sqrt{q\mathcal{E}/(\pi\varepsilon_r)}\right)}{kT}\right], \tag{3}$$

where N_c is the density of states in the conduction band, φ_T is the energy level of the traps through which FPE conduction occurs, ε_r is the optical dielectric constant of the insulator, and k is Boltzmann’s constant [29]. FPE conduction in similarly deposited Ta_2O_5 was previously seen in [30]; fitting of FPE conduction will be discussed below for Region III.

(ii) Negative bias

For negative bias operation, three distinct conduction regions are apparent (marked I, II, and II in Fig. 6.3). The initial negative sweep in Region I shows a rapid increase in current followed by a rough "shelf" of slowly increasing current vs. voltage. In subsequent negative sweeps, current density remains low to about -3 V before rapidly increasing to the same "shelf" value. The negative shift in the voltage at which the rapid increase in current occurs is likely due to charging of defects at the Al_2O_3/Ta_2O_5 interface or in the Ta_2O_5.

For the 1:1 device, the I-V response in region I shows a high degree of linearity for Schottky emission (SE), where

$$J_{SE} = A^*T^2 \exp\left[\frac{-q\left(\varphi_{Bn} - \sqrt{q\mathcal{E}/(4\pi\varepsilon_r)}\right)}{kT}\right], \tag{4}$$

where A^* is the effective Richardson constant for the insulator into which the electron is being injected [29]. Fitting is achieved by replotting data from Region I as ln(J) vs. $E^{1/2}$ and calculating the coefficient of determination (R^2) for the region of interest. For the 1:1 device, the Region I shelf is highly linear ($R^2 = 0.998$) indicating that SE is likely the dominant conduction mechanism. Under negative bias there are two energy barriers to be surmounted, the Ta_2O_5/Al barrier with a theoretical ideal value of 1.0 eV, and the Al_2O_3/Ta_2O_5 barrier with an ideal value of 1.8 eV (assuming a steady supply of electrons in the Ta_2O_5 conduction band. As one would expect that the larger barrier would be the limiting factor in charge transport, we tentatively assign SE over the Al_2O_3/Ta_2O_5 barrier as the dominant conduction mechanism for the 1:1 device. As expected, current shows temperature dependence.

As the Al_2O_3:Ta_2O_5 ratio increases, current density increases and the R^2 value for Schottky emission in Region I decreases, suggesting that another conduction mechanism is also playing a dominate role. For all devices, it is presumed that charge from the Al top electrode is injected into the Ta_2O_5 via either SE over the Ta_2O_5/Al barrier or direct tunneling into the abundant defect levels at about 0.5 eV below the CB of Ta_2O_5 [13]. In the Ta_2O_5, charge transports rapidly through these defect levels via FPE. Upon reaching Al_2O_3/Ta_2O_5 interface, there will be SE of charge over the Al_2O_3/Ta_2O_5 barrier. For the higher ratio devices however, increased current flow indicates that there must be an additional conduction path.

One possible contribution of additional current is from hot carriers. As the thickness ratio is increased to 1:2 and above, for the same applied voltage range, the CB of Ta_2O_5 begins to rise higher than the CB of Al_2O_3. This situation creates the potential for hot electrons within a mean free path of the interface to either surmount the Al_2O_3/Ta_2O_5 barrier and be directly injected into the CB of Al_2O_3 or to energetically assist with SE. As there is a large increase in current between the 1:1 and 1:2 stacks, but only small increases for thicker stacks, it may be that only electrons within a narrow band of distance (at the edge of the mean free path) away from the interface are hot electron assisted, whereas closer electrons are blocked by the barrier and those further away are thermalized.

Another, perhaps more likely, potential cause of the increase in current density with increasing insulator thickness is negative charge at the Ta_2O_5/Al_2O_3 interface. This buildup of charge would increase the field across the Al_2O_3 and decrease the field across the Ta_2O_5, leading to increased Schottky lowering of the Al_2O_3/Ta_2O_5 barrier for thicker stacks and a concomitant increase in SE current.

Since the two interfaces are in electrical series, both hot carrier assistance and negative charge buildup would shift current limiting from the Al_2O_3/Ta_2O_5 to the Ta_2O_5/Al interface. Thus, for the thinner stacks current is limited primarily by the Al_2O_3/Ta_2O_5 interface while for the thicker stacks the current becomes more limited by the Ta_2O_5/Al interface. Given that injection of current at the Ta_2O_5/Al interface should remain relatively constant for all stacks, this would create the interesting situation in which the low field current is greater for the thicker than for the thinner stacks. However, due to the difficulty of modeling competing conduction mechanisms, our assessment of conduction in this region is inconclusive.

The start of Region II (Fig. 6.3) is characterized by a knee marking a steep slope change to exponentially increasing current, which we assign to the onset of FNT through the Al_2O_3 barrier. Due to high defect density, thermal conduction mechanisms such as FPE typically overwhelm tunneling in Ta_2O_5, as demonstrated in Region 4 for positive bias [30].

Shown in Fig. 6.6 is a plot of the negative onset voltage for FNT through the Al_2O_3 ($-V_{onset,FNT}$) for each ratio device, as determined from the intersection of pre- and post-knee slopes. A band diagram illustrating device operation in this regime is shown as an inset. While $+V_{onset,FNT}$ is a strong function of the stack thickness, as expected for a capacitive voltage divider (Fig. 6.5), under negative bias, $-V_{onset,FNT}$ occurs at lower absolute voltages and is only a weak function of stack thickness. Assuming the devices act as ideal capacitive voltage dividers under negative bias, the onset field across the

Al_2O_3 layer, $\mathscr{E}_{onset,FNT,Al2O3}$, *decreases* from roughly -2.7 MV/cm for the 1:1 to roughly -1.25 MV/cm for the 1:9 device. Not only is this field in all cases too low to account for FNT in Al_2O_3, $\mathscr{E}_{onset,FNT,Al2O3}$ should be roughly the same for all stack ratios because the Ta_2O_5/Al_2O_3 injection barrier height remains the same, as do the properties of the Al_2O_3. This indicates that the ideal voltage divider model does not hold for negative bias. Due to high levels of FPE conduction, the Ta_2O_5 layer is highly conductive compared to the Al_2O_3. Therefore, under negative bias, the insulator stack may act more as a resistive voltage divider such that most of the voltage drop is across the Al_2O_3 layer.

If we simply assume that all of the voltage drop occurs across the Al_2O_3, we find that $-\mathscr{E}_{onset,FNT,Al2O3}$ is roughly constant at -4 MV/cm for all device stacks (see Fig. 6.6). This is comparable to the roughly +4 MV/cm onset field for FNT through the 30 nm Al_2O_3 layer under positive bias (Fig. 6.4). However, there is a slight trend to higher $-\mathscr{E}_{onset,FNT,Al2O3}$ for larger insulator ratio devices. This may be accounted for by the fact that thicker Ta_2O_5 layers will proportionally drop more of the field than thinner Ta_2O_5 layers.

The onset of Region III is marked by a distinct rollover in the slope of the J-V response. The rollover occurs due to dielectric breakdown of the Al_2O_3 layer, resulting in the current no longer being limited by FNT through the Al_2O_3. Instead, conduction in this region is well modeled by FPE through only the Ta_2O_5 layer with thicker layers showing higher resistance. FPE simulation with an optical dielectric constant of 4.6, a trap depth of 0.71 eV, and electron mobility of 170 cm^2/V-s yields a close match to the 1:5 device J-V response. The negative bias breakdown voltages (Fig. 6.7(a)), are much lower than observed for positive bias (Fig. 6.4) and have a weaker dependence on stack thickness, increasing from roughly -17 V for the 1:1 device to ~30V for the 1:9 device. Considering again the device to act as a resistive divider rather than a capacitive divider, we find that the average breakdown field for each stack is roughly 8 MV/cm, consistent with Al_2O_3 and slightly higher than for positive bias due to the larger barrier for electron injection.

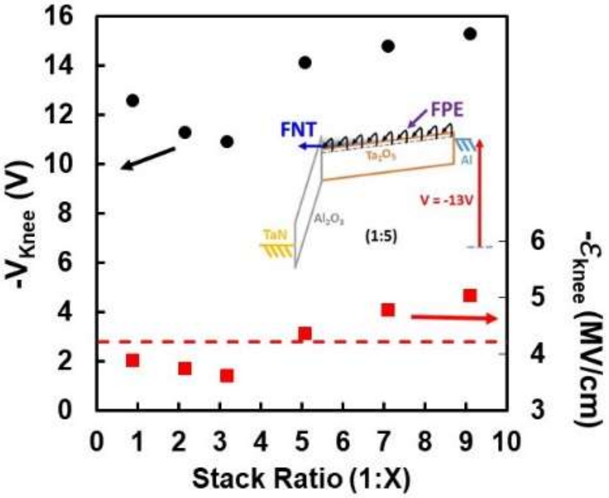

Figure 6.6: Plot of voltage and field within the Al_2O_3 (assuming ideal voltage divider) at which the negative knee between Regions 1 and 2 occurs for all stack ratio devices.

Finally, for the 1:1, 1:2, 1:3, and 1:5 stacks, an increase in slope is observed at larger negative biases. This is due to dielectric breakdown of the Ta_2O_5 layer and current quickly reaches compliance. Assuming that all of the field is dropped across the Ta_2O_5, this leads to a breakdown field of a little over 4 MV/cm, consistent with Ta_2O_5. The 1:1 device shows a larger calculated breakdown field than the thicker stacks (Fig. 6.7(b)), because the small voltage drop occurring across the broken 30 nm Al_2O_3 layer that is ignored in this treatment comprises a greater percentage of the total voltage drop for the lower ratio devices.

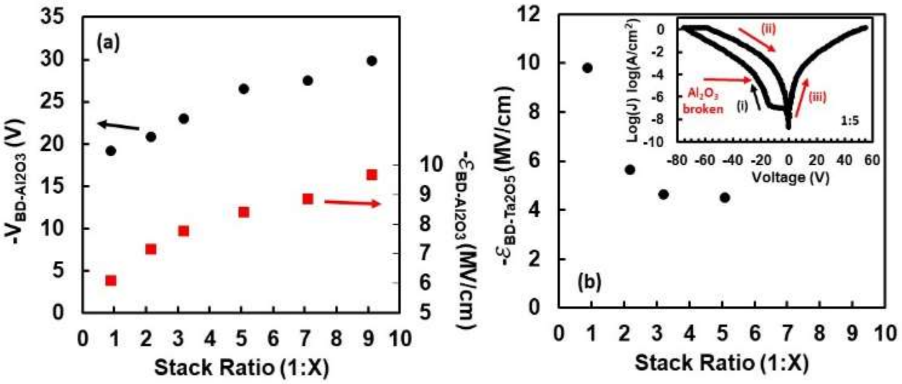

Figure 6.7: (a) Plot of applied voltage and calculated field within the Al_2O_3 (assuming all field is dropped across the Al_2O_3) at which breakdown occurs for all stack ratios. Inset shows reverse sweep for the 1:5 device taken after negative breakdown showing that the Al_2O_3 no longer contributes to the current-voltage behavior. (b) The field within the Ta_2O_5 at which negative breakdown of Ta_2O_5 occurs for those ratios which exhibit this behavior.

6.3.3 Device operation

Shown in Fig. 6.8 is a plot of current-voltage asymmetry (η_{asym}) vs. |V| for all devices. For device operation at voltages less than about +/-12 V (below the onset of negative bias FNT through the Al_2O_3 layer), we find that η_{asym} increases roughly with increasing stack ratio from roughly 5 for the 1:1 to roughly 50 for the 9:1. In this region the devices may be operated as a back end of line (BEOL) weakly rectifying MIM diode in which the asymmetry can be tuned with the thickness of the Ta_2O_5 layer.

With the onset of negative bias FNT conduction through the Al_2O_3 layer, η_{asym} increases rapidly. In this region, with the exception of the 1:1 device, η_{asym} becomes higher for thinner devices. Diode operation in this region is limited by the negative bias breakdown of the Al_2O_3 layer (Region III), which increases only weakly with increasing Ta_2O_5 thickness (Fig. 6.7). $\eta_{asym,max}$ occurs at the forward (negative) breakdown voltage and, with the exception of the 1:1 devices, is roughly independent of stack thickness. The maximum asymmetry voltage is tuned by the Ta_2O_5 thickness, increasing from ~19 V for the 1:1 ratio device to ~52 V for the 1:9 ratio (Fig. 6.4).

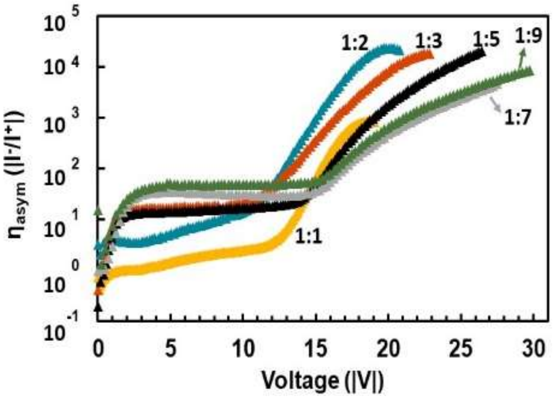

Figure 6.8: Asymmetry (η_{asym}) for all ratios of Al_2O_3:Ta_2O_5, as labeled below each curve, for (a) the entire sweep and (b) the asymmetry which can be obtained prior to irreversible Al_2O_3 breakdown.

Next, we consider the more interesting case of operation as an OTP anti-fuse in which the devices are operated only in reverse (positive) bias. The programming voltage, which normally is at or slightly above the circuit operational voltage, is set by the Al_2O_3 film thickness and stack ratio. In the un-programmed state, the anti-fuse is the open high resistance state (HRS) and current density is very low ($< 10^{-8}$ A/cm^2) up to the onset of FNT. The device is programmed by ramping to the positive Al_2O_3 breakdown voltage so that the anti-fuse is shorted and the device is in the low resistance state (LRS), yielding a maximum programmable resistance ratio (R^+_{LRS}/R^+_{HRS}) at $+V_{onset,FNT,Al2O3}$ which is controlled by the resistive properties of the Ta_2O_5 layer. For the 1:5 stack, R^+_{LRS}/R^+_{HRS} = ~7 x 10^5 at $+V_{onset,FNT,Al2O3}$ (see inset Fig. 6.5).

The maximum operating voltage in the high resistance state ($+V_{onset,FNT,Al2O3}$) and the reverse program voltage ($+V_{BD,Al2O3}$) may be tuned not only with the thickness of the

Al_2O_3 layer but also the thickness of the Ta_2O_5 layer. The resistance of the LRS is controlled by the thickness and properties of the Ta_2O_5 layer while the resistance of the HRS is determined by the thickness and properties of the Al_2O_3 layer.

6.4 Summary and Conclusion

Using TaN bottom gates and Al top gates, a series of thick Al_2O_3/Ta_2O_5 bilayers were deposited via ALD with the Al_2O_3 layer thickness fixed at 30 nm and Ta_2O_5 varied from 30 to 270 nm to assess the impact of insulator thickness ratio on MIIM devices under high voltage operation. Due to low temperature fabrication, MIM based devices are of interest for large area electronics and for implementation in the CMOS BEOL as a way to implement 3D integration and reduced interconnect routing conflicts, building upward away from Si.

Device operation is found to be a strong function of the Al_2O_3/Ta_2O_5 thickness ratio. Trends in conduction and η_{asym} are explained by the asymmetric barrier (Fig. 6.1) created by the pairing of Al_2O_3 and Ta_2O_5 and involve the interplay of several distinct positive and negative bias conduction regions, dominated by either Schottky emission (SE), ohmic conduction and Fowler-Nordheim tunneling (FNT) through the Al_2O_3 barrier, and defect-based Frenkel-Poole emission (FPE) conduction through the Ta_2O_5. Because the FNT onset voltage is dependent (independent) on the Ta_2O_5 thickness under positive (negative) bias, controlling the Ta_2O_5 thickness can effectively tune device operation.

As an OTP anti-fuse, this device shows very low leakage in non-programmed state, has a high programmable resistance ratio, can be read with a relatively small voltage, is compatible with CMOS processes, scalable, reliable (once it has experienced hard breakdown, the Al_2O_3 layer will not self-heal as with e-fuse technology), and is potentially secure. As such, it is of interest for applications such as secure key storage, device IDs, analog/sensor trimming and calibration.

This work demonstrates that ALD bilayers may be used to effectively engineer the reverse breakdown programming voltage, maximum programmable resistance ratio, I-V asymmetry, and operating range of high voltage MIM devices.

6.5 References

[1] J. Shank, E.A. Kadlec, R.L. Jarecki, A. Starbuck, S. Howell, D.W. Peters, and P.S. Davids, "Power Generation from a Radiative Thermal Source Using a Large-Area Infrared Rectenna," Phys. Rev. Appl. **9**, 054040 (2018).

[2] E.C. Anderson and B.A. Cola, "Photon-Assisted Tunneling in Carbon Nanotube Optical Rectennas: Characterization and Modeling," ACS Appl. Electron. Mater. **1**, 692 (2019).

[3] E. Donchev, J.S. Pang, P.M. Gammon, A. Centeno, F. Xie, P.K. Petrov, J.D. Breeze, M.P. Ryan, D.J. Riley, and N.McN. Alford, "The Rectenna Device: From Theory to Practice (a Review)," MRS Energy & Sustainability - A Review Journal **1**, 1 (2014).

[4] N. Alimardani, E.W. Cowell, J.F. Wager, J.F. Conley, Jr., D.R. Evans, M. Chin, S.J. Kilpatrick, and M. Dubey, "Impact of Electrode Roughness on Metal-Insulator-Metal Tunnel Diodes with Atomic Layer Deposited Al2O3 Tunnel Barriers," J. Vac. Sci. Technol. A **30**, 01A113 (2012).

[5] B. Govoreanu, C. Adelmann, A. Redolfi, L. Zhang, S. Clima, and M. Jurczak, “High-Performance Metal-Insulator-Metal Tunnel Diode Selectors,” IEEE Electron Device Lett. **35**, 63 (2014).

[6] S. Vaziri, M. Belete, E. Dentoni Litta, A.D. Smith, G. Lupina, M.C. Lemme, and M. Östling, “Bilayer Insulator Tunnel Barriers for Graphene-Based Vertical Hot-Electron Transistors,” Nanoscale **7**, 13096 (2015).

[7] S. Vaziri, A.D. Smith, M. Östling, G. Lupina, J. Dabrowski, G. Lippert, W. Mehr, F. Driussi, S. Venica, V. Di Lecce, A. Gnudi, M. König, G. Ruhl, M. Belete, and M.C. Lemme, “Going Ballistic: Graphene Hot Electron Transistors,” Solic State Commun. **224**, 64 (2015).

[8] G. Karbasian, M.S. McConnell, H. George, L.C. Schneider, M.J. Filmer, A.O. Orlov, A.N. Nazarov, and G.L. Snider, “Metal-Insulator-Metal Single Electron Transistors with Tunnel Barriers Prepared by Atomic Layer Deposition,” Appl. Sci. **7**, 246 (2017).

[9] T.W. Hickmott, “Defect Conduction Bands, Localization, and Temperature-Dependent Electron Emission from Al–Al2O3–Au Diodes,” Journal of Applied Physics **108**, 093703 (2010).

[10] M. Suzuki, M. Sagawa, T. Kusunoki, E. Nishimura, M. Ikeda, and K. Tsuji, “Enhancing Electron-Emission Efficiency of MIM Tunneling Cathodes by Reducing Insulator Trap Density,” IEEE Transactions on Electron Devices **59**, 2256 (2012).

[11] H. Liu, B. Chen, X. Li, W. Liu, Y. Ding, and B. Lu, “A Metal/Insulator/Metal Field-Emission Cannon,” Nanotechnology **22**, 455302 (2011).

[12] J.G. Simmons, “Electric Tunnel Effect between Dissimilar Electrodes Separated by a Thin Insulating Film,” Journal of Applied Physics **34**, 2581 (1963).

[13] N. Alimardani, S.W. King, B.L. French, C. Tan, B.P. Lampert, and J.F. Conley, Jr., “Investigation of the Impact of Insulator Material on the Performance of Dissimilar Electrode Metal-Insulator-Metal Diodes,” Journal of Applied Physics **116**, 024508 (2014).

[14] S. Grover and G. Moddel, “Engineering the Current–Voltage Characteristics of Metal–Insulator–Metal Diodes Using Double-Insulator Tunnel Barriers,” Solid-State Electronics **67**, 94 (2012).

[15] P. Maraghechi, A. Foroughi-Abari, K. Cadien, and A.Y. Elezzabi, “Enhanced Rectifying Response from Metal-Insulator-Insulator-Metal Junctions,” Applied Physics Letters **99**, 253503 (2011).

[16] P. Maraghechi, A. Foroughi-Abari, K. Cadien, and A.Y. Elezzabi, “Observation of Resonant Tunneling Phenomenon in Metal-Insulator-Insulator-Insulator-Metal Electron Tunnel Devices,” Applied Physics Letters **100**, 113503 (2012).

[17] E.C. Anderson, T.L. Bougher, and B.A. Cola, “High Performance Multiwall Carbon Nanotube–Insulator–Metal Tunnel Diode Arrays for Optical Rectification,” Advanced Electronic Materials **4**, 1700446 (2018).

[18] N. Alimardani and J.F. Conley, Jr., “Enhancing Metal-Insulator-Insulator-Metal Tunnel Diodes via Defect Enhanced Direct Tunneling,” Applied Physics Letters **105**, 082902 (2014).

[19] N. Alimardani and J.F. Conley, Jr., “Step Tunneling Enhanced Asymmetry in Asymmetric Electrode Metal-Insulator-Insulator-Metal Tunnel Diodes,” Applied Physics Letters **102**, 143501 (2013).

[20] I.Z. Mitrovic, A.D. Weerakkody, N. Sedghi, J.F. Ralph, S. Hall, V.R. Dhanak, Z. Luo, and S. Beeby, "Controlled Modification of Resonant Tunneling in Metal-Insulator-Insulator-Metal Structures," Appl. Phys. Lett. **112**, 012902 (2018).

[21] I.Z. Mitrovic, A.D. Weerakkody, N. Sedghi, S. Hall, J.F. Ralph, J.S. Wrench, P.R. Chalker, Z. Luo, and S. Beeby, "(Invited) Tunnel-Barrier Rectifiers for Optical Nantennas," ECS Trans. **72**, 287 (2016).

[22] A.D. Weerakkody, N. Sedghi, I.Z. Mitrovic, H. van Zalinge, I. Nemr Noureddine, S. Hall, J.S. Wrench, P.R. Chalker, L.J. Phillips, R. Treharne, and K. Durose, "Enhanced Low Voltage Nonlinearity in Resonant Tunneling Metal–Insulator–Insulator–Metal Nanostructures," Microelectronic Engineering **147**, 298 (2015).

[23] S.B. Herner, A.D. Weerakkody, A. Belkadi, and G. Moddel, "High Performance MIIM Diode Based on Cobalt Oxide/Titanium Oxide," Applied Physics Letters **110**, 223901 (2017).

[24] J.F. Conley and N. Alimardani, "Impact of Electrode Roughness on Metal-Insulator-Metal (MIM) Diodes and Step Tunneling in Nanolaminate Tunnel Barrier Metal-Insulator-Insulator-Metal (MIIM) Diodes," in *Rectenna Solar Cells*, edited by G. Moddel and S. Grover (Springer New York, New York, NY, 2013), pp. 111–134.

[25] K.H. Kim, B.S. Kang, M. Lee, S. Ahn, C.B. Lee, G. Stefanovich, W.X. Xianyu, C.J. Kim, and Y. Park, "Multilevel Programmable Oxide Diode for Cross-Point Memory by Electrical-Pulse-Induced Resistance Change," IEEE Electron Device Letters **30**, 1036 (2009).

[26] E.Y.H. Teo, C. Zhang, S.L. Lim, E. Kang, D.S.H. Chan, and C. Zhu, “An Organic-Based Diode–Memory Device With Rectifying Property for Crossbar Memory Array Applications,” IEEE Electron Device Letters **30**, 487 (2009).

[27] Y. Zhang, Z. Mei, T. Wang, W. Huo, S. Cui, H. Liang, and X. Du, “Flexible Transparent High-Voltage Diodes for Energy Management in Wearable Electronics,” Nano Energy **40**, 289 (2017).

[28] R. Bernardini and R. Rinaldo, “A Very Stable Diode-Based Physically Unclonable Constant,” Integration **59**, 179 (2017).

[29] F.-C. Chiu, “A Review on Conduction Mechanisms in Dielectric Films,” Advances in Materials Science and Engineering **2014**, e578168 (2014).

[30] N. Alimardani, J.M. McGlone, J.F. Wager, and J.F. Conley, Jr., “Conduction Processes in Metal–Insulator–Metal Diodes with Ta2O5 and Nb2O5 Insulators Deposited by Atomic Layer Deposition,” Journal of Vacuum Science & Technology A **32**, 01A122 (2014).

7 PRELIMINARY RESULTS AND FUTURE WORK

7.1 Internal Photoemission Spectroscopy of MIIM devices

The devices characterized in Chapter 6[1] present a very interesting structure for barrier height analysis. In the configuration used in that work, the barrier to electron flow from the TaN electrode is formed from a single insulator, while both insulators present barriers to electron flow from the Al electrode as shown in the ideal band diagram in Fig. 7.1. In literature there have been reports of IPE measurement within dual-insulator systems, however this has typically been in systems where at least one of the insulators is very thin.[2,3] This is useful, for example, in Fermi-level de-pinning where a thin insulator is inserted at a metal contact interface to provide better control over the Schottky barrier height.[4,5] However, understanding barrier heights in thicker dual-insulator systems such as those in Chapter 6 may be very useful in understanding the complex conduction mechanisms at play.

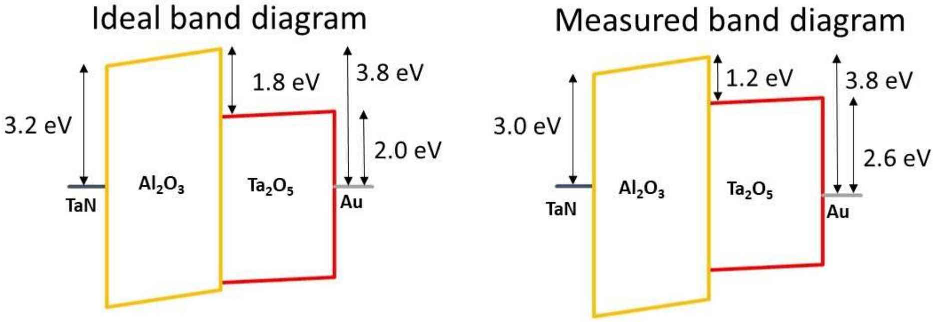

Figure 7.1: Ideal band diagram utilizing vacuum measurements for metal work functions and electron affinities, and measured band diagram determined from IPE barrier height measurements.

Representative yield$^{1/2}$ curves, calculated as outlined in Chapter 1, for the measured barrier heights shown in Fig. 7.1 are shown in Fig. 7.2. Notably, there are two distinct regions of linearity in emission from the top electrode, while there is only one region of linearity in emission from the bottom electrode. Both slopes were extracted and are given in the measured band diagram in Fig. 7.1. These results are beneficial in that they can assist in interpreting the conduction mechanisms in the work from Chapter 6. Future work should focus on depositing new dual-insulator devices with insulators of varying thicknesses and insulator ratios to determine at which point there are no longer two distinct slopes in the yield curves.

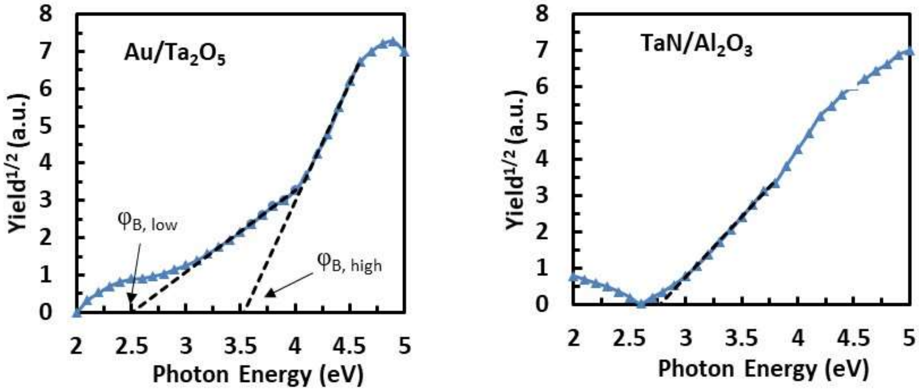

Figure 7.2: Representative yield curves for emission from the top and bottom electrodes. Two regions are extracted from the top electrode curve, with dashed lines guiding the eye for spectral threshold extraction.

7.2 Internal Photoemission Spectroscopy of Solution Deposited Thin Films

Solution deposited films present a number of benefits over traditional vacuum deposited thin films. They are processed at atmosphere, so there is no need for expensive vacuum systems, and they have higher throughput than atomic layer deposited films. Solution deposition has drawbacks as well, such as historically poor electrical performance and high annealing temperatures. We recently demonstrated electrical performance of solution deposited Al_2O_3 comparable to that of ALD Al_2O_3 by using a high-purity starting solution.[6] To follow up on this work, IPE measurements were taken on these high-purity solution deposited films on silicon and TaN substrates and compared to barrier heights of ALD Al_2O_3 in the same devices.

Schottky plots for solution deposited and ALD Al_2O_3 on silicon are shown in Fig. 7.3. Though the solution deposited film could not be measured up to as high of fields as the ALD film, the resulting barrier height with the Au top electrode was found to be the same for both deposition methods at 4.0 eV. This barrier height for ALD Al_2O_3 matches prior reports.[7] Schottky plots for the same films on TaN substrates and with Al top electrodes are shown in Fig. 7.4. These results show a different relationship in that the barrier height for ALD Al_2O_3 is 0.6 eV greater than that of solution deposited Al_2O_3. Generally, a greater degree of disorder in an oxide will tend to decrease the band gap, so it is reasonable that solution deposition would lead to oxides with smaller band gaps than ALD. However, this does not align with the results on silicon. A very likely reason for this is that solution deposited Al_2O_3 leads to significant SiO_x interfacial layer formation,[6,8] so the barrier height found via IPE may be the barrier height with SiO_x rather than Al_2O_3 in the case of the solution deposited film.

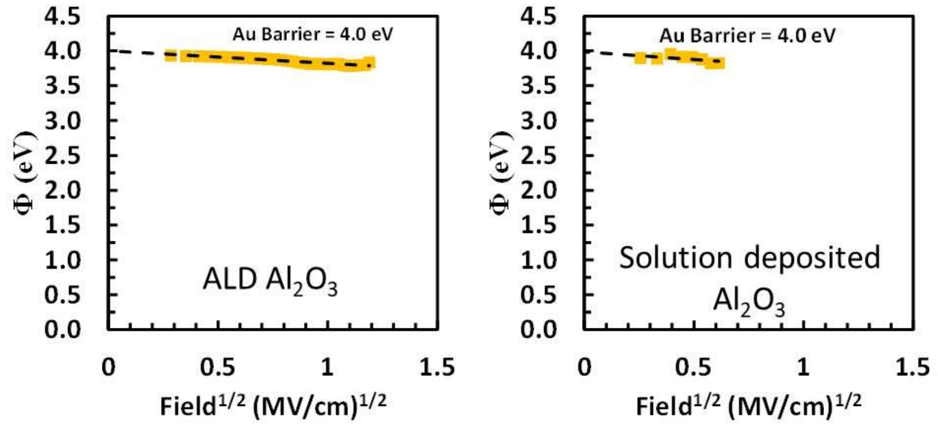

Figure 7.3: Schottky plots for the Au top electrode barrier height for ALD and solution deposited Al_2O_3 on silicon substrates.

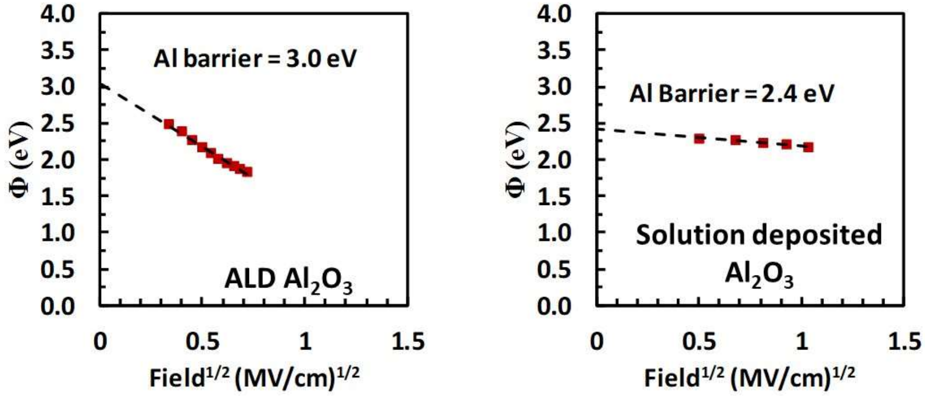

Figure 7.4: Schottky plots for the Al top electrode barrier height for ALD and solution deposited Al_2O_3 on TaN substrates.

The next steps for this work would be to measure additional samples both of Al_2O_3 and other solution deposited films available to ensure that the results seen in this preliminary data are repeatable.

7.3 References

[1] M.A. Jenkins, D.Z. Austin, K.E.K. Holden, D. Allman, and J.F. Conley, Jr., "Laminate Al_2O_3/Ta_2O_5 Metal/Insulator/ Insulator/Metal (MIIM) Devices for High-Voltage Applications," IEEE Trans. Electron Devices 1 (2019).

[2] V.V. Afanas'ev, A. Stesmans, L. Pantisano, and T. Schram, "Electron Photoemission from Conducting Nitrides (TiNx,TaNx) into SiO2 and HfO2," Appl. Phys. Lett. **86**, 232902 (2005).

[3] V.V. Afanas'ev, M. Houssa, A. Stesmans, and M.M. Heyns, "Electron Energy Barriers between (100)Si and Ultrathin Stacks of SiO2,Al2O3, and ZrO2 Insulators," Appl. Phys. Lett. **78**, 3073 (2001).

[4] L. Lin, J. Robertson, and S.J. Clark, "Shifting Schottky Barrier Heights with Ultra-Thin Dielectric Layers," Microelectron. Eng. **88**, 1461 (2011).

[5] D. Connelly, C. Faulkner, P.A. Clifton, and D.E. Grupp, "Fermi-Level Depinning for Low-Barrier Schottky Source/Drain Transistors," Appl. Phys. Lett. **88**, 012105 (2006).

[6] C.K. Perkins, M.A. Jenkins, T.-H. Chiang, R.H. Mansergh, V. Gouliouk, N. Kenane, J.F. Wager, J.F. Conley, and D.A. Keszler, "Demonstration of Fowler–Nordheim Tunneling in Simple Solution-Processed Thin Films," ACS Appl. Mater. Interfaces **10**, 36082 (2018).

[7] M.A. Jenkins, J.M. McGlone, J.F. Wager, and J.F. Conley, Jr., "Internal Photoemission Spectroscopy Determination of Barrier Heights between Ta-Based Amorphous Metals and Atomic Layer Deposited Insulators," J. Appl. Phys. **125**, 055301 (2019).

[8] S.W. Smith, W. Wang, D.A. Keszler, and J.F. Conley, Jr., “Solution Based Prompt Inorganic Condensation and Atomic Layer Deposition of Al_2O_3 Films: A Side-by-Side Comparison,” J. Vac. Sci. Technol. Vac. Surf. Films **32**, 041501 (2014).

8 CONCLUSION

A combination of internal photoemission spectroscopy (IPE) and current-voltage measurements were utilized to characterize barrier heights and conduction mechanisms in metal-insulator-metal (MIM) and metal-insulator-semiconductor (MOS) devices. There were a number of metal-insulator systems characterized with unique components relevant to an array of technological applications.

First, barrier heights at the interface of amorphous metal bottom electrodes and atomic layer deposited (ALD) insulators were characterized. ZrCuAlNi was the first amorphous metal characterized in MIM devices with Al top electrodes. It was found in this work that the ZrCuAlNi barrier heights were lower than expected from vacuum measurements and were indeed lower than Al barrier heights. From these results, it is expected that the effective work function of ZrCuAlNi is closer to that of Al than vacuum measurements of work function would predict and that there is a dipole present at the interface. IPE results were found to be consistent in polarity with current-voltage measurements. Ta-based amorphous metals TaWSi and TaNiSi were also characterized with IPE and current-voltage measurements, along with polycrystalline TaN. It was found that TaWSi has a larger effective work function with the ALD insulators in this work than does ZrCuAlNi, making TaWSi an excellent choice as an electrode where a high work function is needed. It was also found with the Ta-based amorphous metal devices that the polarity of IPE measured barrier heights were in alignment with current-voltage measurements.

The barriers at the interface of ALD ruthenium metal and ALD insulators were characterized as-deposited and following a post-deposition anneal. It was found that the

Ru/Al_2O_3 barrier height was 3.6 eV and the Ru/HfO_2 barrier height was 3.8 eV. Following a post-deposition forming gas anneal, the Al_2O_3 barrier height decreased slightly while the HfO_2 barrier height stayed within the error of measurement. The difference in the as-deposited barrier height between HfO_2 and Al_2O_3 is likely due to a difference in the degree of oxidation of the Ru top electrode. Following post-deposition anneal, there was a steeper slope in the Schottky plot for both oxides, which indicates a greater degree of lateral non-uniformity in the effective work function. This agrees with previous work on sputtered Ru.

Ferroelectric $Hf_{0.58}Zr_{0.42}O_2$ barrier heights with various metal electrodes were determined. Barrier heights with Au, Al, and TaN were all 0.2 eV lower than barrier heights with HfO_2 in previous work, which points to a smaller bandgap for $Hf_{0.58}Zr_{0.42}O_2$ as compared to HfO_2. Use of all extracted barrier heights led to a slope parameter of 0.71 eV. Most of the electrodes showed minimal impact of the applied field on the barrier height, aside from Al. Given that $Hf_{0.58}Zr_{0.42}O_2$ has a relatively high dielectric constant, this is the expected behavior. The deviation with the Al electrode has also been seen in prior work with HfO_2 and is expected to be due to interfacial charge or effective work function lateral non-uniformity.

Thick bi-layer stacks of Al_2O_3 and Ta_2O_5 were characterized with current-voltage analysis and preliminary IPE results of these devices were shown. This work showed tunability of the reverse breakdown programming voltage, maximum programmable resistance ratio, I-V asymmetry, and operating range of high voltage MIIM devices. IPE measurements showed potential for determining the offset between the two insulators in an MIIM device.

Finally, preliminary IPE results on solution deposited Al_2O_3 were compared to ALD Al_2O_3. It was shown that with an Al top electrode and TaN bottom electrode, the Al barrier height with the solution deposited device was 0.6 eV lower than with the ALD device. However, on a device with a Au top electrode and silicon bottom electrode, the Au/Al_2O_3 barrier height was 4.0 eV for both solution deposited and ALD Al_2O_3. This solution deposited film is known to oxidize substrates, so the difference in these results may, in fact, be coming from the SiO_x interfacial layer on the silicon device. Additional samples are needed to confirm these results. Taken together, this work shows an array of materials and devices for which IPE is useful and shows the benefits of directly characterizing barrier heights of new materials using IPE.